From Point Defects to Ripples: Ultrafast Laser Induced High Spatial Frequency Laser Induced Periodic Surface Structures

by

Michael J. Abere

A dissertation submitted in partial fulfillment
of the requirements for the degree of
Doctor of Philosophy
(Materials Science and Engineering)
in The University of Michigan
2015

Doctoral Committee:

Professor Steven M. Yalisove, Chair
Professor John W. Halloran
Professor Joanna M. Millunchick
Professor Jamie D. Phillips
Research Scientist Ben Torralva

© Michael J. Abere

2015

To my late grandfather, Joe Abere for fostering my interest in materials science since the first grade

Acknowledgements

I would like to thank my family and friends for their help and support in my professional studies. I would like to specifically thank Ryan Murphy for guiding me through my initiation into research. Thanks especially to my research mentor Ben Torralva and adviser Steve Yalisove for guiding me through this PhD process.

Table of Contents

Dedication……………………………………………………………………………ii

Acknowledgements……………………………………………………………………..iii

List of Figures…………………………………………………………………………vii

List of Appendices……………………………………………………………………….x

List of Abbreviations……………………………………………………………………xi

Abstract…………………………………………………………………………………xii

Chapter

1. Introduction……………………………………………………………………1

2. Background……………………………………………………………………..…7

2.1 Material response to femtosecond laser irradiation……………………….….……7

2.1.1 Ultrafast melting and band-gap collapse……………………………9

2.1.2 Models for material removal in semiconductors…………………..…13

2.2 Nanoparticle formation from laser irradiation………………………………15

2.3 Surface plasmon polariton coupling…………………………………………16

2.4 Laser induced periodic surface structures……………………………………20

2.4.1 Mechanisms for near lambda periodic surface structures…………21

2.4.2 Mechanisms for low spatial frequency periodic surface structures..22

2.4.3 Model for high spatial frequency periodic structures in dielectrics..23

2.4.4 Preexisting models for high spatial frequency periodic surface structures in semiconductors……………………………………..24

3. Experimental Details…………………………………………………………..29

3.1 Sample Preparation……………………………………………………………30

3.2 Aligning the laser for laser induced periodic surface structure formation….30

3.3 Thin Film Deposition…………………………………………………………33

3.4 Nanoparticle Collection……………………………………………………..33
3.5 Finite element frequency domain simulation………………………………..34

4. Laser Induced Periodic Surface Structures in Semiconductors…………………..38
4.1 Fluence Dependence of laser induced periodic surface structures in semiconductors…………………………………………………………..39
4.2 Point defects and high spatial frequency laser induced periodic surface structures……………………………………………………………………47
4.3 Structural characterization of high spatial frequency periodic surface structures in semiconductors……………………………………………..52

5. Island Precursors to High Spatial Frequency Laser Induced Periodic Surface Structures in Semiconductors……………………………………………………….61
5.1 Nanodot Formation in ZnSe…………………………………………………63
5.2 Nanodot Formation in GaAs…………………………………………………75
5.3 Comparison of point defect based islands and ablation based nanoparticles..80

6. Coupled Surface plasmon polariton and Diffusive Mechanisms of High Spatial Frequency Laser Induced Periodic Surface Structure Formation in Semiconductors…………………………………………………96
6.1 Initial coupling to surface plasmon polaritons………………………………97
6.2 Interplay between strain relaxation, via diffusion, and surface plasmon polaritons…………………………………………………………………..101

7. Effect of Wavelength on Ultrafast Laser Induced Morphology…………………114
7.1 The effect of wavelength above the melt threshold………………………..115
7.2 Control of high spatial frequency laser induced periodic surface structure formation with laser wavelength………………………………………125

8. Summary and Future Work……………………………………………………….134
8.1 Dynamics of defect formation and digital diffusion………………………..137
8.2 Interaction with a laser excited material during band-gap collapse………..139
8.3 Characterization of ultrafast laser generated point defects…………………142
8.4 Temperature and atmosphere control during high spatial frequency laser induced periodic surface structure formation…………………………..143
8.5 Production of a broad-band detector………………………………………144
8.6 Doping with exotic elements……………………………………………….145

Appendices…………………………………………………………………….148

List of Figures

Figure 2.1.1 Relevant timescales for femtosecond laser irradiation……………………………8

Figure 2.1.2 Bond softening and band-gap collapse……………………………………………11

Figure 2.1.3 Bulk ablation in metals and semiconductors……………………………………..14

Figure 2.2.1 Nanoparticle printing setup………………………………………………………16

Figure 2.3.1 Schematic of propagating SPP……………………………………………………17

Figure 2.3.2 Schematic of grating coupled SPP………………………………………………..19

Figure 2.4.1 Ultrafast laser LIPSS in semiconductors………………………………………….20

Figure 3.0.1 Basic laser parameters…………………………………………………………….29

Figure 3.3.1 Experimental setup for LIPSS formation…………………………………………..31

Figure 3.3.2 Experimental setup for frequency doubling………………………………………..32

Figure 3.7.1 COMSOL simulation setup………………………………………………………...36

Figure 4.1.1 Ablation and melt thresholds in GaAs……………………………………………..39

Figure 4.1.2 Low spatial frequency LIPSS………………………………………………………41

Figure 4.1.3 HSFL processing window………………………………………………………….43

Figure 4.1.4 HSFL fluence dependence…………………………………………………………44

Figure 4.1.5 HSFL form via mass redistribution………………………………………………..45

Figure 4.1.6 HSFL transient and final periods…………………………………………………..46

Figure 4.2.1 Schematic of ultrafast point defect formation……………………………………..48

Figure 4.2.2 Time delay study on HSFL formation……………………………………………..51

Figure 4.3.1 Conventional bright field TEM of HSFL………………………………………….53

Figure 4.3.2 STEM of HSFL epitaxial region…………………………………………………...54

Figure 4.3.3 STEM of twin boundary within HSFL…………………………………………….55

Figure 4.3.4 STEM of wurtzite stacked grain in HSFL……………………………………………56

Figure 4.3.5 Raman spectroscopy of HSFL in GaAs…………………………………………….57

Figure 5.0.1 Island precursors to HSFL in GaAs and ZnSe……………………………………..62

Figure 5.1.1 HSFL and nanodot formation in ZnSe……………………………………………..64

Figure 5.1.2 Fluence dependence of nanodot formation in ZnSe………………………………..66

Figure 5.1.3 Coarsening via surface diffusion of ZnSe nanodots………………………………..67

Figure 5.1.4 Volume expansion of ZnSe nanodots from bulk diffusion…………………………69

Figure 5.1.5 STEM of ZnSe nanodots…………………………………………………………..72

Figure 5.2.1 SEM of GaAs nanodots formed from 390 nm irradiation…………………………76

Figure 5.2.2 Volume stability of GaAs nanodots………………………………………………..77

Figure 5.3.1 NiO nanoparticles formed over the plasma threshold……………………………..82

Figure 5.3.2 Chemical and structural characterization of NiO nanoparticles……………………83

Figure 5.3.3 Ni thin film material removal thresholds…………………………………………..84

Figure 5.3.4 NiO nanoparticles printed from 10 nm films………………………………………85

Figure 5.3.5 NiO nanoparticles printed from 20 nm films………………………………………87

Figure 5.3.6 NiO nanoparticle size vs removed film thickness via liquid spallation……………89

Figure 6.0.1 HSFL evolution in GaAs…………………………………………………………..97

Figure 6.1.1 Initial uncorrelated islands on GaAs surface………………………………………98

Figure 6.1.2 SPP coupling to a single island……………………………………………………100

Figure 6.2.1 Island alignment and coarsening in GaAs………………………………………...102

Figure 6.2.2 Pair correlation function of aligned islands………………………………………104

Figure 6.2.3 SPP coupling to aligned islands with regular spacings…………………………..106

Figure 6.2.4 Negative feedback between SPP coupling and coarsening when pits nucleate…..107

Figure 6.2.5 HSFL evolution along the grating coupled SPP dispersion curve……………….109

Figure 6.2.6 HSFL strain driven bifurcation…………………………………………………..111

Figure 7.1.1 Wavelength dependence of ablation and melt thresholds in GaAs………………115

Figure 7.1.2 Wavelength dependence of crater depth in GaAs………………………………..116

Figure 7.1.3 AFM of ZnSe/GaAs film/substrate morphologies for 780 nm irradiation………..118

Figure 7.1.4 SEM of ZnSe/GaAs film/substrate morphologies for 780 nm irradiation above the ZnSe melt threshold………………………………………………………………………….119

Figure 7.1.5 SEM of ZnSe/GaAs film/substrate morphologies for 780 nm irradiation below the ZnSe melt threshold………………………………………………………………………….120

Figure 7.1.6 ZnSe/GaAs film/substrate morphologies for 390 nm irradiation…………………121

Figure 7.2.1 Wavelength dependence of HSFL period in GaAs………………………………..126

Figure 7.2.2 Inhibition of HSFL formation in GaAs for 390 nm irradiation…………………..127

Figure 7.2.3 Parallel LIPSS formation in GaAs for 390 nm irradiation……………………….128

Figure 7.2.4 Wavelength dependence of excited dielectric function in GaAs…………………129

Figure 8.1 Optical image of HSFL nucleation…………………………………………………137

Figure 8.2 GaAs nanodots from temporal pulse shaping………………………………………139

Figure 8.3 Parallel Si LIPSS from temporal pulse shaping…………………………………….141

Figure A3.1 Experimental setup for Si threshold………………………………………………158

Figure A3.2 Two parameter fit for Si threshold………………………………………………..159

Figure A3.3 Schematic of Clark MXR laser……………………………………………………160

Figure A3.4 Diagnostic Si morphology………………………………………………………..162

List of Appendices

Appendix 1: Dielectric Function Code……………………………………………148

Appendix 2: Pair Correlation Code…………………………………………….152

Appendix 3: Calibrating an Ultrafast Laser with the Si Threshold…………….157

Appendix 4: Microscopy long after irradiation………………………………..165

List of Abbreviations

AFM - Atomic force microscope

BBO - Beta-barium borate

CCD - Charge coupled device

HSFL - High spatial frequency laser induced periodic surface structure

LIPSS - Laser induced periodic surface structure

LSFL - Low spatial frequency laser induced periodic surface structure

OM - Optical microscope

SEM - Scanning electron microscope

SP - Surface plasmon

SPP - Surface plasmon polariton

STEM - Scanning transmission electron microscope

TEM - Transmission electron microscope

YAG - Yttrium Aluminum Garnett

λ - Wavelength

Abstract

From Point Defects to Ripples: Ultrafast Laser Induced High Spatial Frequency Laser Induced Periodic Surface Structures

by

Michael J. Abere

Chair: Steven M. Yalisove

This dissertation explores the interaction between ultrashort laser pulses and solids and focusses specifically on regular corrugations produced in semiconductors. Individual structures have length scales ranging from less than a nm to hundreds of nm, uniformly cover the entire irradiated region, and form in air at ambient temperature and pressure. The resulting morphologies are characterized in a combination of optical microscopy, scanning electron microscopy, atomic force microscopy, transmission electron microscopy, and Raman spectroscopy. These experimental results are combined with finite element frequency domain calculations in order to develop a physical model for the formation of ultrafast laser induced nanostructures.

This thesis identifies a coupled mechanism that operates in a specific range of fluences in semiconductors between two well understood ultrafast laser thresholds, that for band-gap collapse and ultrafast-melt, that produces a unique corrugation known as high spatial frequency laser induced periodic surface structures (HSFL). The HSFL have period < 0.3 times the laser

wavelength and are predominately epitaxial single crystal. While these structures are observed to form universally in semiconductors, previous existing models have focussed on a single component of the coupled process and either do not predict the period, allow for an evolution through multiple intermediate nanostructures, or explain the polarization dependence on orientation.

This thesis meets three stated goals. First, this thesis determines that the mechanism responsible for ultrafast point defect generation generation in semiconductors is a softening of the inter-atomic binding potential due to electron excitation, which allows for some atoms to drift to an interstitial site with their room temperature thermal velocity. Diffusion of the resulting vacancy/interstitial pairs redistributes mass in order to form nanostructures such as islands, pits, and the aforementioned HSFL.

Second, this thesis establishes that role of surface plasmon polaritons (SPP) on nanostructures formed by the diffusion of laser induced point defects is to localize point defect generation where the absorbed intensity is maximized. The interplay between SPPs and transient surface morphologies driven by strain relaxation, via diffusing defects, results in the evolution through three distinct periods during HSFL formation. The first intermediate LIPSS population is a previously unreported stage of evolution that has the highest of the three observed spatial frequencies and is responsible for the initial coherence between the structures and laser polarization. The second, longer period forms at the grating coupled SPP wavelength, and the third is the result of a bifurcation of those structures.

Third, this thesis will investigate the wavelength dependence of ultrafast laser materials interactions as a means to gain control over the formation of islands and HSFL. Small excursions from the laser's fundamental frequency produce HSFL with periods that scale with the grating coupled SPP wavelength. Further, this thesis demonstrates that the defect generation and SPP-based mechanisms can be decoupled, which allows for the formation of nanodots that do not align into HSFL. By establishing a fundamental understanding of the mechanisms responsible for HSFL formation, this thesis opens the potential for ultrafast laser directed self-assembly.

Chapter 1

Introduction

The interaction between ultrashort laser pulses and solids allows for the study of materials under extreme conditions. By compressing light pulses down to the femtosecond timescale, solids can be irradiated at intensities on the order of 10^{11}-10^{13} W/cm^2 while only depositing microjoules of energy into the material. For the irradiation conditions covered in this thesis, these high intensity lasers excite solids into an unusual non-equilibrium state where the electrons have temperatures exceeding 11,000°K [Wang, 1994] while the lattice remains at room temperature [Chen, 2006]. Moreover, the excited non-equilibrium carrier density is often on the order of 10% of all valence electrons in the solid [Graves, 1998], which substantially changes the interatomic binding potential [Lindenberg, 2005]. The dynamical pathway a material takes back to equilibrium from this unusual state may permit atomic mixing [Serpenguzel, 2008], rapid liquid-vapor separation [Reis, 2006], or surface morphologies [Tull, 2006] generally inaccessible by other means.

This thesis will focus on a surface corrugation in semiconductors unique to ultrafast laser irradiation known as high spatial frequency laser induced periodic surface structures (HSFL) so named because they have periods < 0.3 times the laser wavelength. The structures self-assemble via an additive mass redistribution process as opposed to the far more commonly studied laser ablation [Liu, 1997; Bonse, 2002; Ancona, 2008; Sher, 2011; Kumar, 2014]. The way in which

the long timescale material response to ultrafast laser irradiation could drive an additive process have remained largely unexplored and thus the mechanism for HSFL formation has remained unexplained. This thesis will present, for the first time, a complete model detailing the cascading and coupled mechanisms driven by surface plasmon polariton coupling and a semiconductor's material response to ultrafast laser irradiation responsible for HSFL formation as well as each of the intermediate nanostructures observed during formation. These additional morphologies include a combination of LIPSS, islands, and pits.

This thesis will describe the way in which this laser induced self-assembly arises from the generation of vacancy/interstitial pairs formed on a sub-picosecond timescale after an optical excitation softens the inter-atomic binding potential within a fluence range between the well understood ultrafast laser damage thresholds of band-gap collapse [Glezer, 1995] and ultrafast-melt [Lindenberg, 2005]. By understanding the origin the point defects and the fluences at which they can form and accumulate, this thesis will refine the fundamental physical understanding of ultrafast laser materials interactions. Understanding the formation of vacancy/interstitial pairs expands upon our previous understanding of band-gap collapse by showing that the lattice does not completely restore after bond softening.

Furthering the fundamental understanding of ultrafast laser materials interactions allows us to confirm models within other fields where the processes have overlap. The strain driven defect diffusion leading to these structural and compositional properties can serve as an alternate system for confirming models for surface patterning in the fields of molecular beam epitaxy and ion beam irradiation. In addition, the study of a material's pathway back to equilibrium from a

state in which the electron and ion temperatures are orders of magnitude apart from each other has allowed for the use the laser to study phase changes in nuclear power applicable materials [Rittman, 2015].

A major advantage of laser based techniques is techniques that they have the speed and scalability for roll-to-roll processing [Ahn, 2008] and can be performed in air at ambient temperature and pressure. The HSFL presented in this thesis are one such nanostructure that could be patterned on the sheet scale with these next generation lasers. The epitaxial and stoichiometric nature of the HSFL hold potential to improve production of nano-plasmonic [Schuller, 2010] and optoelectronic [Sher, 2011] devices. Surface patterning typically leads to a loss of the original crystal structure, which leads to losses in device efficiency through scattering at grain boundaries. Avoiding this trade-off would be particularly useful for developing broad band sensors for low light applications ranging from military drones to self-driving cars to in-vivo medical imaging devices. Moreover, there mere fact that the laser can enhance mobility in the near surface of holds great potential in the field of semiconductor doping as foreign atoms will more readily diffuse into near-surface vacancies.

The goals of this thesis include:

Determine the mechanism responsible for ultrafast point defect generation and the defects' diffusional properties long after irradiation

1. To determine the origin of laser induced nanodots
2. To determine the diffusional component of high spatial frequency laser induced periodic surface structure formation.

Establish the role of surface plasmon polaritons on nanostructures formed by the diffusion of laser induced point defects

1. To develop a complete model for the formation of high spatial frequency laser induced periodic surface structures.
2. To gain size and shape control over nanostructures formed via laser induced point defect diffusion

To investigate the wavelength dependence of ultrafast laser materials interactions

1. To investigate the effects of exciting specific inter-band transitions during ultrafast point defect generation
2. To gain wavelength control over high spatial frequency laser induced periodic surface structures

The impact of this thesis is a fundamental understanding of the formation of ultrafast laser generated nanostructures formed from the interplay between surface plasmon polaritons and transient surface morphologies driven by strain relaxation, via diffusing point defects. The basic science implications of these findings are that the ultrafast laser can controllably enhance the mobility of atoms within a semiconductor on a sub-picosecond timescale through optical excitation. Furthermore, ultrafast laser irradiation can localize this enhanced mobility within an existing surface structure by coupling to surface plasmon polaritons (SPP). The wavelength dependence of SPP coupling allows us to both control HSFL period as well as completely inhibit their formation.

References

X.Y. Wang, D.M. Riffe, Y.S. Lee, and M.C. Downer, *Phys. Rev. B.* **50**, 8016 (1994).

J.K. Chen, D.Y. Tzou, and J.E. Beraun*, Int. J. Heat Mass Tran.* ***49,*** 307 (2006).

JS. Graves and RE. Allen, *Phys Rev. B.* **58**, 13627 (1998).

AM. Lindenberg, J. Larsson, K. Sokolowski-Tinten, KJ. Gaffney, C. Blome, O. Synnergren, J. Sheppard, C. Caleman, AG. MacPhee, D. Weinstein *et al*. *Science*. **308.** 392 (2005).

A. Serpenguzel, A. Kurt, I. Inanc, J. Carey, and E.Mazur, *J. Nanophoton.* **2**, 021770 (2008).

D.A. Reis, K.J. Gaffney, G.H. Gilmer, and B. Torralva, *MRS Bulletin.* **31**, 601 (2006).

B.R. Tull, J.E. Carey, E. Mazur, J.P. McDonald, and S.M. Yalisove, *MRS Bulletin.* **31**, 626 (2006).

X. Liu, D. Du, and G. Mourou, *IEEE J. Quantum. Elect.* **33**, 1706 (1997).

J. Bonse, S. Baudach, J. Kruger, W. Kautek, and M. Lenzner, *Appl. Phys. A.* **74**, 19 (2002).

A. Ancona, F. Roser, K. Rademaker, J. Limpert, S. Nolte, and A. Tunnermann, *Opt Express.* **16**, 8958 (2008).

M-J. Sher, M.T. Winkler, and E. Mazur, *MRS Bulletin.* **36**, 439 (2011).

K. Kumar, K.K. Lee, J. Li, J. Nogami, N.P. Kherani, and P.R. Herman, *Nature Light: Science & Applications.* **3**, e157 (2014).

J.A. Schuller, E.S. Barnard, W. Cai, Y.C. Jun, J.S. White, and M.L. Brongersma, *Nat. Mater.* **9**, 193 (2010).

EN Glezer, Y. Siegal, L. Huang, and E. Mazur, *Phys. Rev. B.* **51**, 6959 (1995).

AM. Lindenberg, J. Larsson, K. Sokolowski-Tinten, KJ. Gaffney, C. Blome, O. Synnergren, J. Sheppard, C. Caleman, AG. MacPhee, D. Weinstein *et al*. *Science*. **308.** 392 (2005).

D.R. Rittman, C.L. Tracy, A.B. Cusick, M.J. Abere, B. Torralva, R.C. Ewing, and S.M. Yalisove, *Appl. Phys. Lett.* **106**, 171914 (2015).

S.H. Ahn and J.L. Guo, *Adv. Matr.* **20**, 2044 (2008).

Chapter 2

Background

A review of ultrafast laser materials interaction detailing ablation, melting, band-gap collapse, and surface plasmon polariton (SPP) coupling will be presented in this chapter. In addition, this chapter will provide a review of previous work on laser induced periodic surface structures. The chapter will conclude with a brief overview of previous work in printing nanoparticles using laser induced forward transfer.

Section 2.1 Material response to femtosecond laser irradiation

This thesis will focus on the interaction between ultrafast lasers and solids. This class of laser involves compressing the temporal profile of the beam down to femtosecond timescales in order to produce high intensity pulses [Strickland, 1985]. A typical Ti:sapphire ultrafast laser is capable irradiation at fluences as high as 10^2 J/cm^2, which for a 150 fs pulse is equivalent to 6.7 x 10^{14} W/cm^2 at focus [Clark MXR]. Ti:sapphire refers to a lasing medium made of Al_2O_3 doped with Ti ions. The Ti:sapphire crystal is pumped with a second green laser, often neodymium doped yttrium aluminum garnet based, and seeded with a third fiber laser. Pulse amplification inside of ultrafast lasers is performed using chirped pulse amplification [Strickland, 1985]. The low energy short pulse is stretched in time by a pair of gratings. The stretched pulse can be amplified without damaging the laser's internal optics before being recompressed by a second

pair of gratings. The resulting high energy, ultrashort pulse then exits the laser cavity and can be delivered to the desired sample.

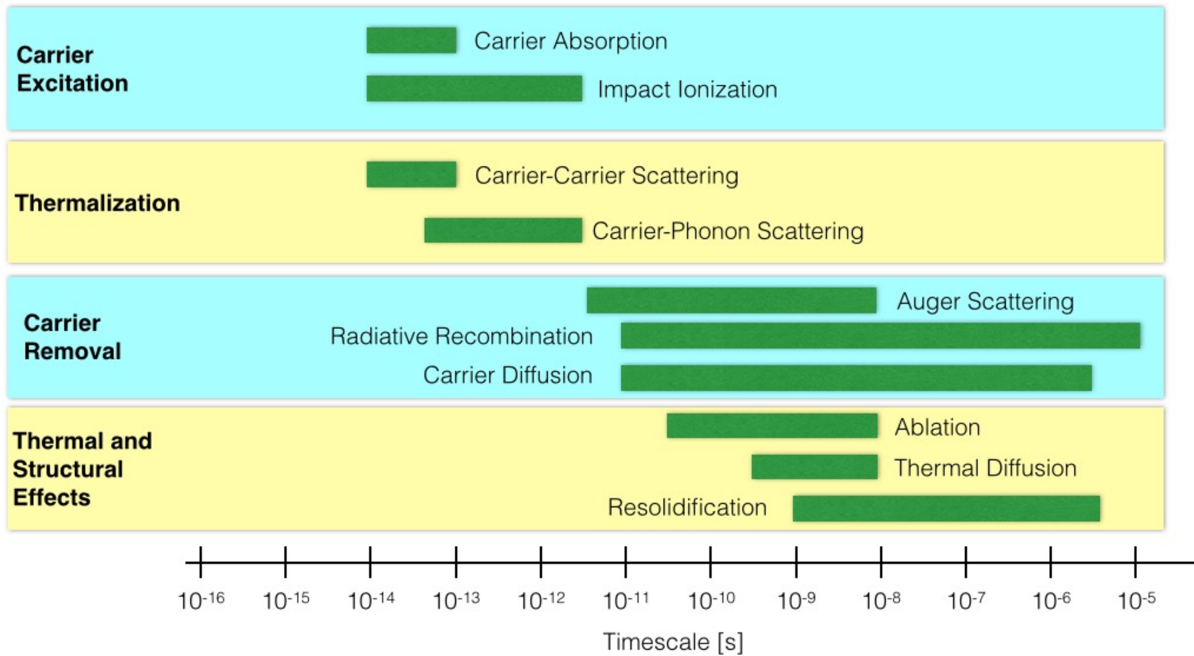

Figure 2.1.1 Timescales of various electron and lattice processes in laser-excited solids for non-equilibrium carrier excitation on the order 10^{17}-10^{22} cm^{-3} (ie: those relevant to the work in this thesis) adapted from [Sundaram, 2002].

During the laser-material interaction, photon absorption excites valence electrons within the solid. Typical ultrafast laser intensities are high enough that even linearly transparent semiconductors can still absorb strongly through a combination of tunneling ionization and multi-photon absorption [Keldysh, 1964]. The excited carriers cannot be described by Boltzmann kinetics [Banyai, 1995] and remain in a non-Fermi distribution for hundreds of femtoseconds [Sun, 1994; Chen, 2006]. By this time, the laser pulse is no longer interacting with the solid. The material, however, is in an extreme non-equilibrium state. This thesis will specifically examine

how the dynamical pathway a semiconductor can take from this unusual material state can lead to unique surface morphologies.

The excited electrons approach a Fermi-Dirac distribution after 200 fs [Chen, 2006] as electrons and holes are redistributed throughout the conduction and valance bands through carrier-carrier and carrier-phonon scattering. Once thermalized, the hot electrons have temperatures exceeding 11,000 K while the ions remain at room temperature [Wang, 1994] in what is known as the two-temperature model [Anisomov, 1974; Chen, 2006]. For metals and semiconductors, continued carrier-phonon scattering transfers energy back to the lattice until the material reaches thermal equilibrium, a process that takes several ps. Once the material has a single defined temperature, the excited free carriers undergo recombination. Recombination occurs through a combination of carrier diffusion out of the excited region, radiative recombination, and Auger scattering. The relevant timescales for each of these processes are shown in Figure 2.1.1. The well understood structural changes that occur before the material reaches thermal equilibrium will be covered in Sections 2.1.1 and 2.1.2.

Section 2.1.1 Ultrafast melting and band-gap collapse

Ultrafast laser irradiation has the ability to induce structural changes to materials on timescales shorter than those necessary for thermal expansion. It has long been known that semiconductor reflectivity can resemble that of a liquid within the first picosecond after irradiation [Shank, 1983; Downer, 1985]. This “ultrafast-melting” was characterized using double-angle reflectivity [Glezer, 1995a; Huang, 1997]. For a given time delay, the reflectivity of

(a)

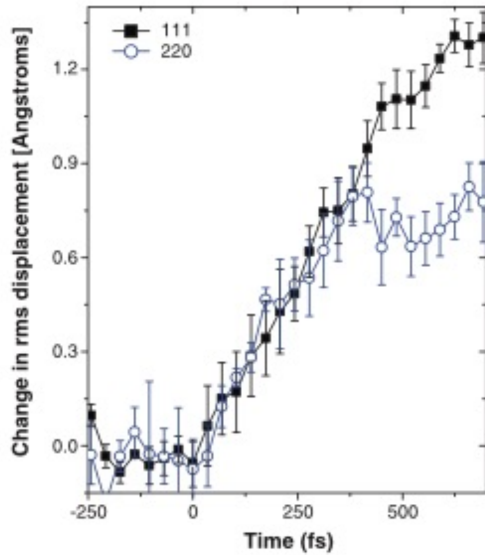

(b)

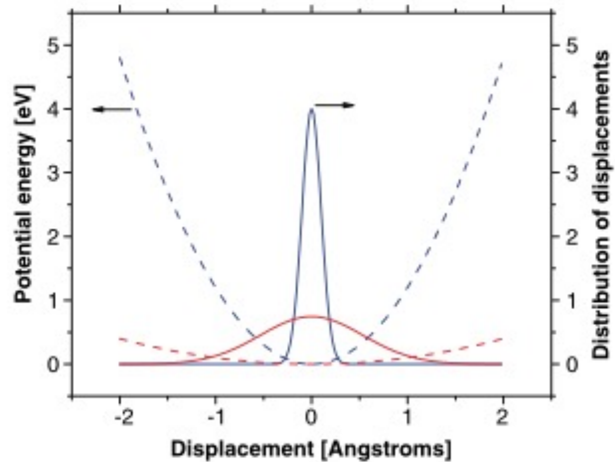

(c)

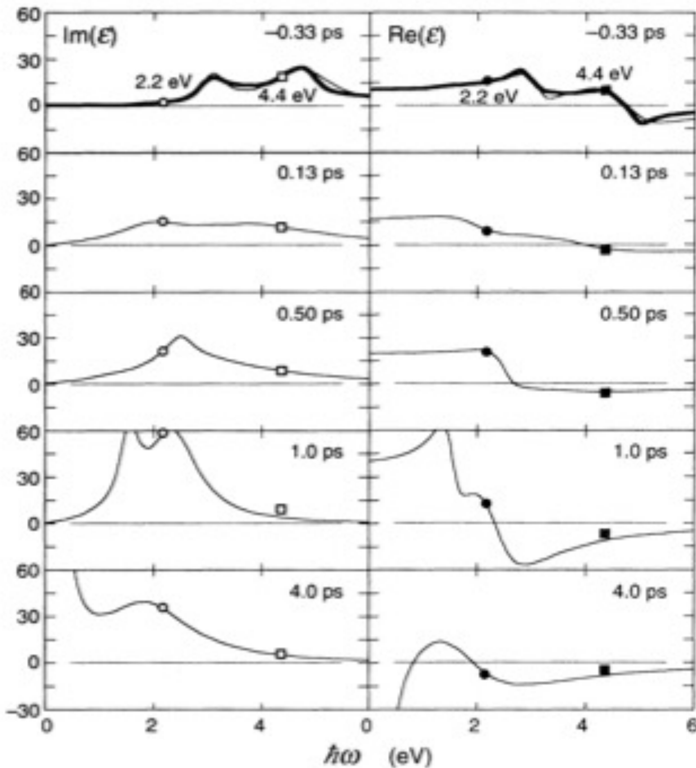

Figure 2.1.2. (a) Adapted from Lindenberg, 2005: The change in root mean squared displacement extracted from the time-dependent x-ray diffraction data of laser excited InSb showing atoms drifting at their room temperature thermal velocity (b) One-dimensional illustration showing the softening of the interatomic potential (dashed lines) leads to an increase in the root mean squared displacement (solid lines) after laser irradiation. (c) Adapted from Glezer, 1995: The effect of the atomic motion in (a) and (b) on the dielectric function of GaAs. The time dependent curves are calculated from reflectivity data using a 2-oscillator fit. C++ code written to repeat this fit is included in Appendix 1. The imaginary part of the dielectric function first becomes non-zero at the band-edge. The redshift in the band-edge due to atomic drift is known as band-gap collapse in semiconductors.

the laser irradiated semiconductor was measured at two angles for a p-polarized pump beam reflecting off the surface. The dielectric function was calculated from the two reflectivity measurements using the Fresnel equation for p-polarized light given in Equation 2.1.1 below:

$$R_p=|[(\mu_0/\varepsilon_{semi})^{0.5}\cos(\theta_t)-(\mu_0/\varepsilon_{air})^{0.5}\cos(\theta_i)]/[(\mu_0/\varepsilon_{semi})^{0.5}\cos(\theta_t)+(\mu_0/\varepsilon_{air})^{0.5}\cos(\theta_i)]|^2$$

Equation 2.1.1

where R_p is the reflectivity of p-polarized light, μ_0 is the permeability of free space, ε_{semi} is the laser excited dielectric function of the semiconductor, ε_{air} is the dielectric function of the air environment, θ_t is the transmitted beam angle, and θ_i is the incident beam angle. The transmitted angle is not measured directly, but is calculated in terms of known parameters via Snell's Law. The imaginary part of the excited semiconductor dielectric function is determined by setting one of the two angles to the Brewster angle, which allows the real part to be calculated from the reflectivity at a second arbitrary angle.

Double-angle reflectivity studies show that ultrafast laser irradiation causes a redshift in the absorption peak of a semiconductor's dielectric function as shown in Figure 2.1.2c. The peak energy corresponds to the average bonding-antibonding splitting in the semiconductor. As the bonding-antibonding splitting decreases, the semiconductor band-gap narrows. This phenomena is known as band-gap collapse and is observed at fluences both above and below the ultrafast-melt threshold. Above the melt threshold, the original dielectric function [Glezer, 1995a; Huang, 1997; Sundaram, 2002] permanently disappears. However, for fluences above the band-gap collapse threshold but below the ultrafast-melt threshold, changes to the dielectric function last at least 8 ps, but then the material appears to completely recover after a single laser exposure

[Glezer, 1995a]. The double-angle reflectivity results were corroborated with second harmonic generation studies, which showed that a zinc-blende semiconductor lost its $\underline{4}3m$ symmetry during band-gap collapse [Glezer, 1995b; Sokolowski-Tinten 1995]. For GaAs at fluences just above the band-gap collapse threshold, the original second harmonic generation did not return until at least 100 ns after irradiation [Sundram, 2002].

The specific nature of the structural changes occurring during band-gap collapse and ultrafast melt were determined with synchrotron x-ray diffraction [Lindenberg, 2005; Fritz, 2007]. After irradiation, the diffraction peak intensity decreases to 10% of its initial value within hundreds of femtoseconds. The loss in peak intensity was correlated to an increase in root mean squared (RMS) displacement using a Debye-Waller model shown below in Equation 2.1.2:

$$I(Q,t) = \exp(-Q^2\langle u^2(t)\rangle/3)$$

(Equation 2.1.2)

where I is the diffracted peak intensity, Q is the reciprocal lattice vector of the probed reflection, t is time, and $\langle u^2(t)\rangle$ is the time dependent RMS displacement of the ion core.

After irradiation, the atoms move with velocities set by their initial conditions such that $\langle u^2(t)\rangle^{1/2}=v_{thermal}\cdot t$ meaning that they are drifting at their room temperature velocity as shown in Figure 2.1.2a.. For an atom with initial velocity away from its lattice site, the room temperature velocity is capable of drifting half a unit cell in a picosecond. The fluences where this occurred were consistent with theoretical work predicting that exciting 10% of the valance electrons would cause the material to melt on a sub-picosecond timescale [Stampfli, 1990; Graves, 1998]. In the suggested model, the excited carriers have anti-bonding character that softens the

interatomic binding potential by removing the attractive term. The magnitude of this softening is fluence dependent. The softened binding potential increases the ions' root mean squared displacement as they oscillate about the lattice site at their room temperature thermal velocity. When the electrons begin to relax and restore the attractive part of the potential, electron-phonon coupling leads to rapid melting. This model was consistent with the original claims that the observed reflectivity changes were the result of what is referred to as "ultrafast melting" [Shank, 1983; Downer, 1985]. The focus of Chapter 4 will be an extension of this model for the fluence regime above band-gap collapse but below the melt threshold where this thesis will show that atoms within a laser softened interatomic binding potential can form the point defects that serve as a feedstock for both the nanodots covered in Chapter 5 as well as the high spatial frequency laser induced periodic surface structures (HSFL) discussed in Chapters 4 and 6.

Section 2.1.2 Models for material removal in semiconductors

Ultrafast melting of semiconductors leads to a rapid amorphous resolidification of the material [Saeta, 1991; Bonse, 2004]. Increasing the irradiation fluence beyond the melt threshold leads to the regime for ultrafast laser ablation. On the timescale after ultrafast melting but before thermal expansion can occur, extreme pressure gradients form at the air-liquid and liquid-bulk interfaces as the high temperature liquid remains at constant volume. A compressive, and subsequent tensile wave are launched into the melt, which causes free volume within the melt to coalesce into voids along a plane [Sokolowski-Tinten 1998; von der Linde, 2000; Rethfield, 2004]. The tensile stress is maximum at the reduced cross sectional area between the voids, which leads to spallation of the liquid layer. The resulting craters form with deterministic

thresholds after a single laser exposure, which allows us to correlate a given damage morphology to the local fluence from the Gaussian pulse. The ablation craters have a smooth surface [Bonse, 2002] resulting directly from the void nucleation mechanism [Murphy, 2013a]. This thesis will discuss how this well understood ablation mechanism can be used to calibrate our optical setups in Chapter 3. Laser ablation thresholds also serve as a means to characterize the wavelength dependent response of irradiated semiconductors in Chapter 7.

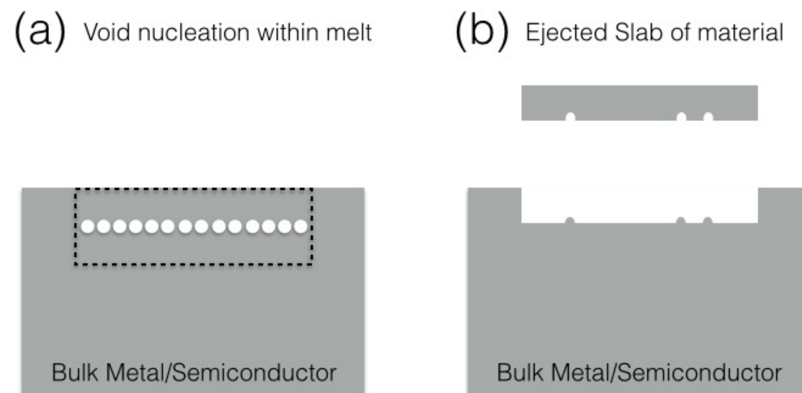

Figure 2.1.3 (a) After irradiation the near surface region of the metal or semiconductor melts as signified by the region contained by the dotted line. Voids nucleate homogeneously at a plane within the melt. (b) Cross-section schematic of material ablation. The material separates along the plane of void nucleation leaving a mostly smooth surface.

Section 2.2 Nanoparticle formation from laser irradiation

Nanoparticles can be produced via a variety of techniques including chemical methods [Kim, 2004] and pulsed laser deposition. Pulsed laser deposition generally involves bulk irradiation in air [Bracikowski, 2007], water [Kabashin, 2003], vacuum [Amoruso, 2005], or an ambient gas [Bracikowski, 2007]. Material removal during ultrafast laser irradiation produces particles with diameters between a few to hundreds of nanometers [Lowndes, 1996]. The nanoparticle size depends on both the dynamics of material removal [Haverkamp, 2003] and cooling [Liu, 2007] conditions.

Nanoparticle printing was first explored for nanosecond laser irradiation [Murray, 2008] and the technique was expanded to femtosecond lasers for printing from both Au [Amoruso, 2011] and Pt [Rouleau, 2014] films. Printing with femtosecond lasers produced more narrow nanoparticle distributions in Au but did not shift the average particle size. Printing from the Pt films produced two distinct modes in the nanoparticle size distribution.

Our own work printing from Ni thin films with a modified version of the laser induced forward transfer technique [Bohandy, 1988] showed that the average particle size can be controlled in two ways. When printing nanoparticles in air, changing the spacing between the film and TEM grid allowed for air currents to filter out the smaller particles resulting in shifts to the average collected nanoparticle diameter [Murphy, 2013b]. Additionally, changing the film thickness between 20 nm and 10 nm produced radically different nanoparticle distributions. Chapter 5.3 of this thesis will explore the physical mechanisms behind our ability to control ultrafast laser printed nanoparticle size.

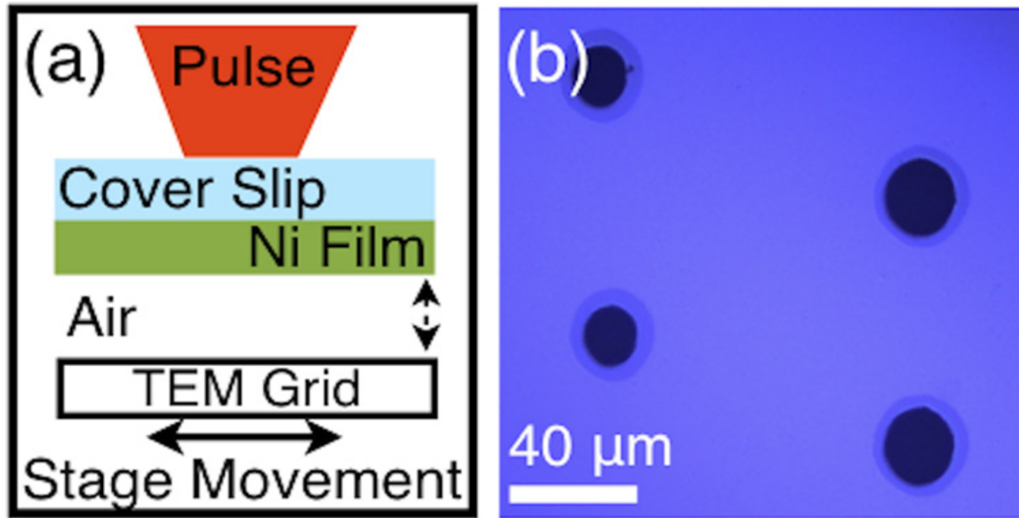

Figure 2.2.1. From Murphy, Abere *et al*, 2013: (a) Illustration of nanoparticle printing setup for a top-down irradiation geometry in the lab-frame. The dashed arrow represents the film to grid separation, while the solid line denotes the scanning direction. (b) Differential interference contrast optical image of irradiated Ni film used for nanoparticle printing.

Section 2.3 Surface plasmon polariton coupling

Plasmons are a collective oscillation of a free electron density with respect to fixed positive ions in a metallic material. Ultrafast lasers can excite enough electrons into the conduction band to form a dense electron-hole plasma at the surface of a semiconductor, making it temporarily metallic [Sokolowski-Tinten, 2000]. The dielectric function for an excited semiconductor can be calculated using Equation 2.3.1 below:

$$\varepsilon_{excited\ _semiconductor} = 1 + [\varepsilon_g(\hbar\omega + \Delta E_{gap}) - 1] * Ng - \omega_p^2/(\omega(\omega + i\Gamma))$$

(Equation 2.3.2)

where ε_g is the ground state dielectric function, ΔE_{gap} is a term for band-gap renormalization, Ng is the fraction of valence electrons in the ground state, ω_p is the plasma frequency, and Γ is the

electron collision frequency. The band renormalization term describes the way in which the sum of exchange-correlation effects and the screened ionic potential reduce contributions from the ground state dielectric function. For fluences that initiate the atomic motion described by band-gap collapse, this term is approximately equal to the GaAs band-gap [Kim, 1994]. Γ is typically on the order of 1 fs for laser excited semiconductors [Sokolowski-Tinten, 2000].

If the plasmon is confined to a surface at a metal/dielectric interface, it is referred to as a surface plasmon. During ultrafast laser irradiation with a 150 fs pulse, electron excitation within the first 11 fs [Becker, 1988] forms the dense electron-hole plasma, while photons that arrive later in the pulse can couple to the oscillating electrons to launch surface plasmon polaritons (SPPs). In short, the SPP refers to the coupling between collective oscillations in the electron-hole plasma, the plasmon, and the resulting radiated electromagnetic field, the polariton [Piazza, 2015].

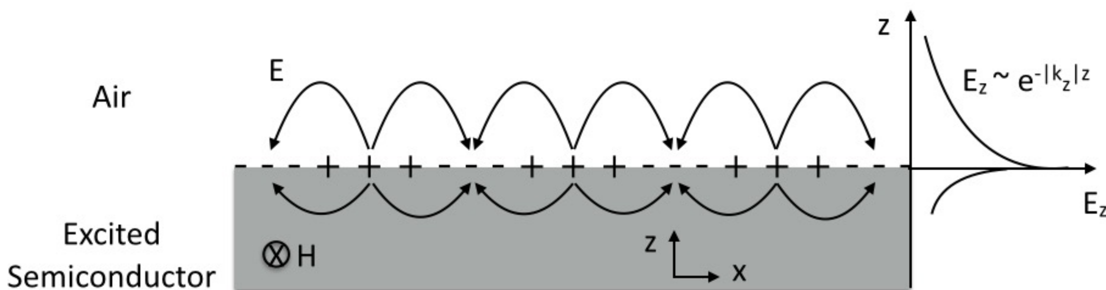

Figure 2.3.1 Schematic of the relative charges due to local differences in electron density and electromagnetic field of SPPs propagating on the surface in the x-direction. SPP propagation requires a metal/dielectric interface, satisfied in this case by a laser excited semiconductor and air. The period of E is equal to the SPP wavelength. H_y shows the magnetic field direction in the y direction for a p-polarized wave. The electric field in the z direction is also plotted to show that the SPP is an evanescent wave that decays exponentially into the material.

In order for a photon to couple to a plasmon, surface roughness must also be present. This occurs because the photon wave-vector in the dielectric is always smaller than that of the SPP, so the photon wave vector must increase by the difference in order to couple to the plasmon. The surface features rotate the laser field in order to provide the necessary momentum to the photon in the coupling direction. The SPP is confined evanescently in the direction perpendicular to the interface but is able to propagate along the surface in the direction of the laser polarization since SPP excitation is prohibited for transverse electric mode but not the transverse magnetic mode with respect to the surface features [Zayats, 2005]. The SPP is shown schematically in Figure 2.3.1. The frequency, ω, of the longitudinal SPP wave is tied to its wave-vector, k_x, by a dispersion relation $\omega(k_x)$ as described by Equation 2.3.2 [Raether, 1988]:

$$k_x = \omega/c \cdot [\varepsilon_{dielectric} \cdot \varepsilon_{excited_semiconductor} / (\varepsilon_{dielectric} + \varepsilon_{excited_semiconductor})]^{1/2}$$

(Equation 2.3.2)

where c is the speed of light and ε is a complex dielectric function. The real parts of the two dielectric functions must have opposite signs, as is the case at a metal/dielectric interface, in order for the wave-vector of the SPP to be real.

Surface plasmon polariton coupling to a regular grating changes the dispersion relation and reduces the oscillation period of the longitudinal wave [Raether, 1988]. For the special condition where k_x is equal to half of the grating's Bragg vector (ie: the grating period is equal to half the SPP wavelength), Bragg scattering results in both forward and backward traveling waves that constructively interfere to form standing waves [Barnes, 1996]. This standing wave can either have nodes at the top and bottom of the grating or within the grating sidewalls [Barnes,

2003]. Coupling to either region has a different energy but the same periodicity for the two standing waves, which leads to a band-gap forming within the polariton as shown schematically in Figure 2.3.2. Frequencies between the energies of the two standing waves are unable to propagate since they completely destructively interfere with another wave along the grating. Chapter 6 of this thesis will focus on the way in which SPPs locally enhance the electric field on grating structures leads to the formation at specific periods of HSFL in semiconductors.

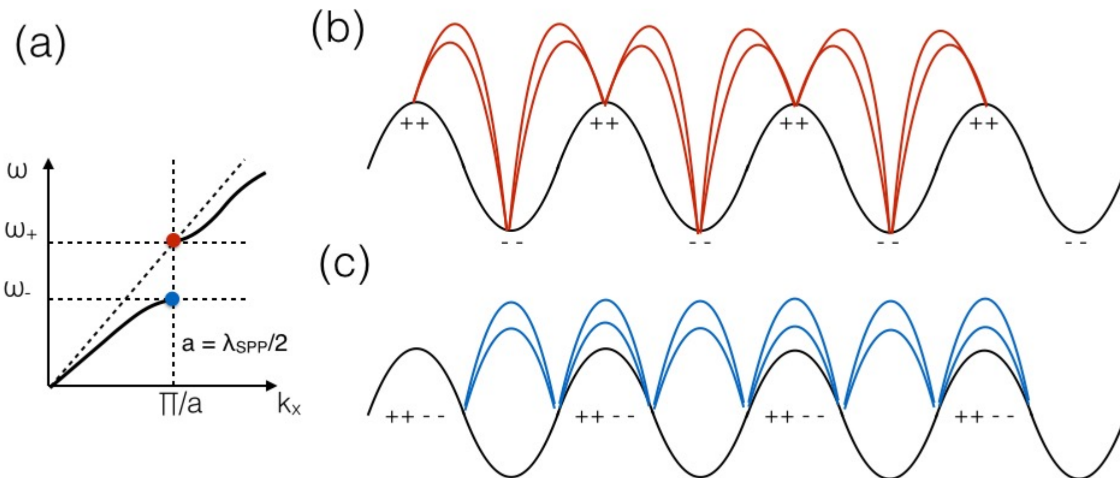

Figure 2.3.2 SPP coupling to a pre-existing grating on a surface can lead to the formation of an SP-photonic band-gap. The band-edge is located at a grating period equal to half of the SPP wavelength, which is shown schematically in (a). At the band-edge the SPP can couple with two different energies depending on the location of charge separation within the grating. (b) Charge separation at the structure tops and trench bottoms corresponds to the high energy upper branch of the SP-photonic band-gap dispersion curve. (c) Charge separation within the structure sidewalls corresponds to the lower branch. At the band edges the density of SP states is high, and there is a significant increase in the associated field enhancement.

Section 2.4 Laser induced periodic surface structures

Surface corrugation is one of the most fundamental phenomena in materials science. This thesis will focus on the long studied [Birbaum, 1965] field of using light to produce a corrugation known as laser induced periodic surface structures (LIPSS). The structures appear universally in metals [Bonse, 2012], semiconductors [Bonse, 2012; Huang, 2009; van Driel, 1982; Sipe, 1983; Costache, 2004; Reif, 2011], and insulators [Bonse, 2012; Bhardwaj, 2006] and orient with their long axis either parallel or perpendicular to the laser polarization. Structure formation occurs in air and at room temperature. These LIPSS are generally attributed to the laser interacting with roughness on the material surface. If no such roughness is initially present, then a single exposure only produces a crater. This section will provide a brief overview of the various types of LIPSS structures formed after pulsed laser irradiation.

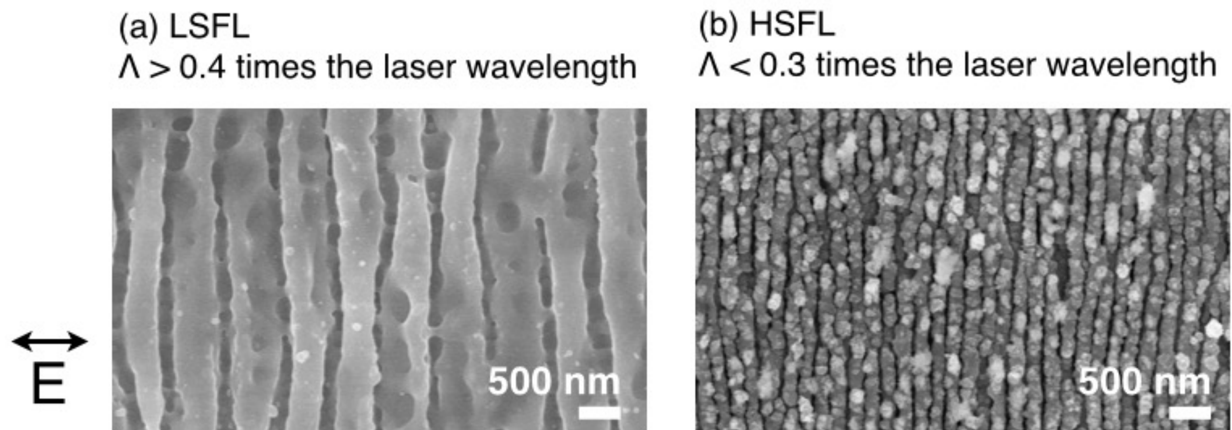

Figure 2.4.1 (a) LSFL and (b) HSFL formed after femtosecond laser irradiation of GaAs. Both populations align perpendicular to the laser polarization.

Section 2.4.1 Mechanisms for near lambda periodic surface structures

Irradiation with multiple nanosecond laser exposures produces a LIPSS with periods on the order of the laser wavelength [Guosheng, 1982; Sipe, 1983]. For semiconductors, the LIPSS form within a crater after multiple exposures with a period near the laser wavelength and orient perpendicular to the laser polarization. SPP based models do not explain nanosecond laser based LIPSS that form below the melt threshold because the ripples should form with periods noticeably less than the laser wavelength and that the nanosecond laser intensity was not large enough to excite enough electrons to directly transform a semiconductor into a metal [Guosheng, 1982]. However, in the case where irradiation is above the melt threshold, the semiconductor becomes a liquid metal [Shvarev, 1974], which can be accurately described by the Drude model [Comins, 1972]. Since the laser pulse duration for nanosecond laser is longer than the time required for the semiconductor to thermally melt, the pulse is able to interact with the liquid metal and couple to SPPs. Based on Equation 2.1.1, for a sufficiently negative real dielectric response, the SPP wavelength approaches the laser wavelength, which is consistent with the observed LIPSS after nanosecond laser irradiation.

The LIPSS with period lambda are attributed, in a model that is referred to today as "classical LIPSS formation," [Sipe, 1983] to laser coupling to the randomly rough "selvedge region" of a material surface. The selvedge region refers to local variations in the surface profile of the material and separates the homogenous bulk sample from vacuum. By treating this selvedge region as the superposition of multiple diffraction gratings of varying periods, Sipe and van Driel found that the light interacts with all of the grating periods but most strongly couples to the transverse magnetic mode for gratings with a period near the laser wavelength. In the case

where the material's dielectric function during the laser interaction is metallic (ie: above the melt threshold), absorption into the transverse magnetic mode would be dominated by SPP coupling [Sipe, 1983].

Near lambda LIPSS can also form after femtosecond laser irradiation, but they orient parallel to the laser polarization [Murphy, 2013c]. LIPSS in this orientation cannot form due to SPP coupling. These LIPSS instead form due to Fresnel diffraction from step edges parallel to the laser polarization. In cases where both parallel and perpendicular step edges are present, such as in a crater, only perpendicular LIPSS are observed because the SPP based mechanism dominates over the Fresnel diffraction. The perpendicular LIPSS formed from femtosecond laser irradiation will be the focus of the next sub-section of this chapter.

Section 2.4.2 Mechanisms for low spatial frequency periodic surface structures

The perpendicular LIPSS have noticeably different characteristics when formed from femtosecond laser irradiation. The LIPSS have periods less than the laser wavelength and can form in two distinct populations in semiconductors. This section will focus on the low spatial frequency laser induced periodic surface structures (LSFL) that form with periods 0.45 and 0.95 times the laser wavelength.

The near sub-wavelength character of LSFL occurs due to local field enhancement from SPP coupling. A 150 femtosecond pulse does not last long enough for the material to melt [Lindenberg, 2005]. Therefore, unlike nanosecond irradiation, the source of the SPP cannot be from a liquid metal. Instead the laser's high intensity is capable of exciting over 10% of the valence electrons [Graves, 1998], which is sufficient to form a dense electron-hole plasma that

causes the dielectric properties of the semiconductor to became metallic during excitation [Sokolowski-Tinten, 2000]. Near the melt threshold, the excited semiconductor is weakly metallic so k_x is large enough to produce measurable differences in LSFL period compared to the laser wavelength [Bonse, 2012]. Regions with enhanced absorption from the SPP preferentially ablate after each exposure, leading to deeper trenches [Huang, 2009; Murphy, 2013d]. Additional exposures interact with the existing structures and allow for contributions form the grating coupled SPPs, which further decreases LIPSS period to as low as 0.4 times the laser wavelength [Huang, 2009; Bonse, 2012].

Section 2.4.3 Model for high spatial frequency periodic structures in dielectrics

Ultrafast laser irradiation can produce periodic sub-surface structures in dielectrics that are less than 10 nm wide with a period on the order of 0.3 times the laser wavelength [Bhardwaj, 2006; Taylor, 2007]. The structures form beneath the surface and must be ground, polished, and etched in order to observe them in characterization techniques such as atomic force microscopy or scanning electron microscopy. The etched structures are ~15 nm deep and form with long axis perpendicular to the laser polarization regardless of scan direction after 10^3 exposures. Although they have similar wavelengths, these structures in dielectrics do not share the same mass redistributive characteristics as the semiconductor high spatial frequency LIPSS (HSFL) that are the focus of this thesis. To further contrast the two populations, the HSFL in semiconductors do not scale linearly with wavelength [Boroweic, 2003] and can form when absorption is primarily linear.

The high spatial frequency periodic sub-surface structure formation is explained by a nanoplasmonics model [Bhardwaj, 2006; Taylor, 2007]. For transparent dielectrics, ultrashort pulses can create ionization hot-spots due to localized inhomogeneous nonlinear multi-photon ionization at defects or color centers. Each exposure increases the local density of the glass at the hot spots, which increases the plasma generation rate at these sites on subsequent exposures. This positive feedback mechanism leads to spherical nanoplasmas forming within the glass. The spherical nanoplasmas grow asymmetrically in a linearly polarized field [Jackson, 1975] to form planks. The planes do not begin with a regular distribution but undergo a competitive process where the lowest order optical mode from within the initial distribution that can be supported within the glass preferentially forms.

Section 2.4.4 Preexisting models for high spatial frequency periodic surface structures in semiconductors

Ultrafast laser irradiation in semiconductors universally produces HSFL in addition to the previously discussed LSFL. The HSFL have periods ≤ 0.3 times the laser wavelength [Bonse, 2012], which is too small to be explained by the LSFL formation mechanism. Semiconductor HSFL form after hundreds to thousands of exposures at fluences below the threshold for the material ablation that leads to LSFL [Costache, 2004]. Existing models have suggested that this shorter period may be due to second harmonic generation during the laser-material interaction [Dufft, 2009] or the dominance of a non-resonant mode within the SPP [Huang, 2013]. A third model relates HSFL formation to the selective sputtering that leads to ripples after ion beam irradiation [Reif, 2011].

Each of these models does not provide a complete story for HSFL formation. The second harmonic generation model does not explain why formation occurs completely independently of crystal orientation [Boyd, 1948], the fact that HSFL formation has an intermediate period during evolution [Reif, 2011], and fails to accurately predict the final LIPSS period in many materials [Bonse, 2012; Boroweic, 2003]. Purely SPP based models do not explain how a non-resonant mode would dominate over the resonant mode at the previously discussed standing wave solution [Barnes, 2003]. Meanwhile, a purely diffusional model does not explain how the HSFL orient perpendicular to the laser polarization and are not affected by crystal orientation. Finally, none of the previously existing models explain the transient LIPSS that serve as a precursor during HSFL formation that have a shorter period than the final structures because the work contained within this thesis is the first observation of this population.

In summary, LIPSS are a long studied phenomena. LIPSS form via a variety of different mechanisms that depend on both the laser irradiation parameters as well as the target material. While the formation mechanisms of some populations are well understood, the HSFL in semiconductors have until now remained unexplained. This thesis will focus on providing a self-consistent model for their formation.

References

D. Strickland and G. Mourou, *Opt. Commun.* **55**, 447 (1985).

http://www.cmxr.com/Products/LaserProducts/CPA-Series.html

L.V. Keldysh, *Zh. Eksp. Teor. Fiz.* **47** 1945 (1964).

L. Banyai, D.B. Thoai, E. Reitsamer, H. Haug, D. Steinbach, M.U. Wehner, M. Wegener, T. Marschner, and W. Stolz, *Phys. Rev. B.* **75**, 2188 (1995).

C. K. Sun, F. Vallee, L. H. Acioli, E. P. Ippen, J. G. Fujimoto, Phys. Rev. B. **50**, 15337 (1994).

J.K. Chen, D.Y. Tzou, and J.E. Beraun*, Int. J. Heat Mass Tran.* ***49**, 307 (2006).*

X.Y. Wang, D.M. Riffe, Y.S. Lee, and M.C. Downer, *Phys. Rev. B.* **50**, 8016 (1994).

S.I. Anisimov, B.L. Kapeliovich, T.L. PerelÕman, *Sov. Phys. JETP* **39,** 375 (1974).

C.V. Shank, R. Yen, and C. Hirlimann, *Phys. Rev. Lett.* **51**, 900 (1983).

M. C. Downer, R. L. Fork, and C. V. Shank, *J. Opt. Soc. Am. B.* **2**, 595 (1985).

EN Glezer, Y. Siegal, L. Huang, and E. Mazur, *Phys. Rev. B.* **51**, 6959 (1995).

L. Huang, *Thesis*, (1997).

SK. Sundaram and E. Mazur, *Nat. Mater.* **1**, 217 (2002).

EN Glezer, Y. Siegal, L. Huang, and E. Mazur, *Phys. Rev. B.* **51**, 9589 (1995).

K. Sokolowski-Tinten, J. Bialkowski, and D. von der Linde, *Phys. Rev. B.* **51**, 14186 (1995).

A. Rousse, C. Rischel, S. Fourmaux, I. Uschmann, S. Sebban, G. Grillon, Ph. Balcou, E. Forster, JP. Gelndre, P. Audebert, JC. Gauthiers, and D. Hulin. *Nature Lett.* **410.** 65 (2001).

AM. Lindenberg, J. Larsson, K. Sokolowski-Tinten, KJ. Gaffney, C. Blome, O. Synnergren, J. Sheppard, C. Caleman, AG. MacPhee, D. Weinstein *et al*. *Science*. **308.** 392 (2005).

DM. Fritz, DA. Reis, B. Adams, RA. Arke, J. Arthur, C. Blome, PH. Bucksbaum, AL. Cavalieri, S. Engemann, S. Fahy, *et al*. *Science*. **315**, 633 (2007).

P. Stampfli, *Phys. Rev. B.* **42,** 7163 (1990).

JS. Graves and RE. Allen, *Phys Rev. B.* **58**, 13627 (1998).

P. Saeta, JK. Wang, Y. Siegal, N. Bloembergen, and E. Mazur, *Phys. Rev. Lett.* **67**, 1023 (1991).

J. Bonse, K. W. Brzezinka, and A. J. Meixner, *Appl. Surf. Sci.* **221**, 215 (2004).

K. Sokolowski-Tinten, J. Bialkowski, A. Cavalleri, D. von der Linde, A. Oparin, J. Meyer-ter-Vehn, and S.I. Anisimov, *Phys. Rev. Lett.* **81**, 224 (1998).

D. Von der Linde, and K. Sokolowski-Tinten, Appl. Surf. Sci. **154**, 1 (2000).

B. Rethfeld, K. Sokolowski-Tinten, D. von der Linde, and S.I. Anisimov, *Appl. Phys. A.* **79**, 767 (2004).

J. Bonse, S. Baudach, J. Kruger, W. Kautek, and M. Lenzner, *Appl. Phys. A.* **74**, 19 (2002).

R.D. Murphy, B. Torralva, and S.M. Yalisove, *Appl. Phys. Lett.* **102.** 181602 (2013).

Y. Kim, S. Oh, and R. M. Crooks, *Chem. Mater.* **16**, 167 (2004).

S. Barcikowski, A. Hahn, A. V. Kabashin, and B. N. Chichkov, *Appl. Phys. A*. **87**, 47 (2007).

A. V. Kabashin and M. Meunier, *J. Appl. Phys*. **94**, 7941 (2003).

S. Amoruso, G. Ausanio, R. Bruzzese, M. Vitiello, and X. Wan, *Phys. Rev. B*. **71**, 033406 (2005).

D. H. Lowndes, D. B. Geohegan, A. A. Puretzky, D. P. Norton, and C. M. Rouleau, *Science* **273,** 898 (1996).

J. Haverkamp, R. M. Mayo, M. A. Bourham, J. Narayan, C. Jin, and G. Duscher, *J. Appl. Phys*. **93**, 3627 (2003).

B. Liu, Z. Hu, Y. Che, Y. Chen, and X. Pan, *Appl. Phys. Lett*. **90**, 044103 (2007).

P. T. Murray and E. Shin, *Mater. Lett*. **62**, 4336 (2008).

S. Amoruso, N. N. Nedyalkov, X. Wang, G. Ausanio, R. Bruzzese, and P. A. Atanasov, *J. Appl. Phys*. **110**, 124303 (2011).

C.M. Rouleau, C.Y. Shih, C. Wu, L.V. Zhigilei, A.A. Puretzky, and D.B. Geohegan, *Appl. Phys. Lett.* **104**, 193106 (2014).

J. Bohandy, B. F. Kim, F. J. Adrian, and A. N. Jette, *J. Appl. Phys*. **63**, 1158 (1988).

R.D. Murphy, M.J. Abere, K.J. Schrider, B. Torralva, and S.M. Yalisove, Appl. Phys. Lett. 103, 093113 (2013).

K. Sokolowski-Tinten and D. Von der Linde, *Phys. Rev. B*. **61**, 2643 (2000).

L Piazza, T.T.A. Lummen, E Quiñonez, Y Murooka, B.W. Reed, B Barwick, and F Carbone, *Nat. Comm*. **6**, 1 (2015).

H. Raether, "*Surface Plasmons on Smooth and Rough Surfaces and on Gratings"* Springer (1988).

A. V. Zayats, I. I. Smolyaninovb, A. A. Maradudinc, *Nano-optics of surface plasmon polaritons*, Physics Reports **408**, 131 (2005).

D.H. Kim, H. Ehrenreich, and E. Runge, *Solid State Communications*, **89**, 119 (1994).

B.C. Becker, H.L. Fragnito, C.H.B. Cruz, R.L. Fork, J.E. Cunningham, J.E. Henry, and C.V. Shank, *Phys. Rev. Lett.* **61**, 1647 (1988).

WL. Barnes, T.W. Priest, S.C. Kitson, and J.R. Sambles, *Phys. Rev. B.* **54**. 6227 (1996)

WL. Barnes, A. Dereux, and T.W. Ebbesen, *Nature*. **424**. 824 (2003).

M. Birnbaum, *J. Appl. Phys.* **36**, 3688 (1965).

J. Bonse, J. Kruger, S. Hohm, and A. Rosenfeld, *J. Laser App.* **24**, 042006 (2012).

M. Huang, F. Zhao, Y. Cheng, N. Xu, and Z. Xu, *ACS Nano.* **3**, 4062 (2009).

HM. van Driel, JE. Sipe, JF. Young, *Phys. Rev. Lett.* **49**, 1955 (1982).

JE. Sipe, J.F. Young, and HM. van Driel, *Phys. Rev. B.* **27**, 1141 (1983).

F. Costache, S. Kouteva-Arguir, and J. Reif, *Appl. Phys. A.* **79**, 1429 (2004).

J. Reif, O. Varlamova, S. Varlamov, and M. Bestehorn, Appl. Phys. A. **104**, 969-973 (2011).

VR. Bhardwaj, E. Simova, PP. Rajeev, C. Hnatovsky, R.S. Taylor, DM. Rayner, and P.B. Corkum, *Phys. Rev. Lett.* **96**, 057404 (2006).

Z. Guosheng, P. M. Fauchet, and A. E. Siegman, *Phys. Rev. B.* **26**, 5366 (1982).

K. M. Shvarev, B. A. Baum, and P. V. Gel'd, Fiz. Tverd. Tela. (Leningrad) **16**, 3246 (1974) [Sov. Phys. — Solid State **16**, 2111 (1975)]

N. R, Comins, *Philos. Mag.* **25**, 817 (1972)

R.D. Murphy, B. Torralva, D.P. Adams, and S.M. Yalisove, *Appl. Phys. Lett.* **102**, 211101 (2013).

R.D. Murphy, B. Torralva, D.P. Adams, and S.M. Yalisove, *Appl. Phys. Lett.* **103**, 141104 (2013).

R. Taylor, C. Hnatovsky, and E. Simova, *Laser Photonics Rev.* **2**, 26 (2008).

J.D. Jackson, "*Classical Electrodynamics*" Wiley (1998).

D. Dufft, A. Rosenfeld, S.K. Das, R. Grunwald, and J. Bonse, *J. Appl. Phys.* **105**, 034908 (2009).

M. Huang, Y. Cheng, F. Zhao, and Z. Xu, *Annalen der Physik.* **525**, 74 (2013).

R.W. Boyd, "*Nonlinear Optics*" Boston Academic Press (1948).

A. Boroweic and H.K. Haugen, *Appl. Phys. Lett.* **82**, 4462 (2003).

Chapter 3

Experimental Details

Experiments were performed with a Clark MXR CPA-2001 Ti:Sapphire pulsed laser. The central wavelength was 780 ± 5 nm with a repetition rate of 1 kHz and a 150 fs pulse duration. The beam has a maximum pulse energy of 1 μJ and a Gaussian spatial profile. A second 50 W, 1064 nm, 600 fs laser with a variable repetition rate between 100 kHz and 50 mHz could also be sent down all existing optical lines. Morphological changes from laser irradiation were characterized using various microscopy techniques. The following section details the irradiation procedures, beam calibration, and microscopy techniques used in this thesis.

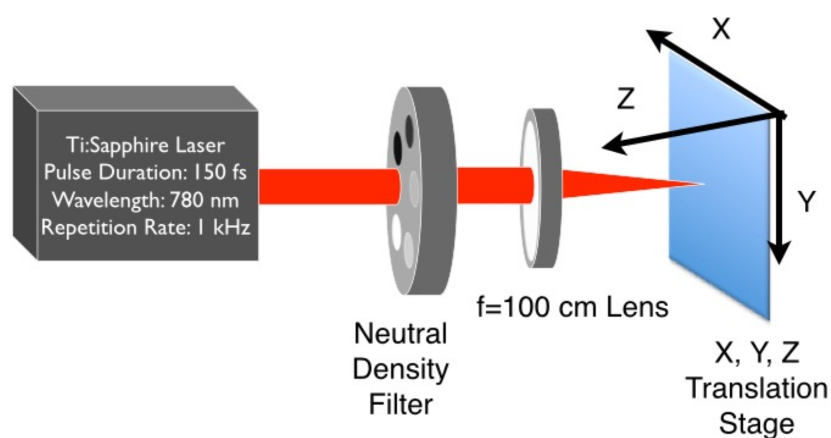

Figure 3.0.1 Clark MXR CPA 2001 laser parameters and general irradiation setup

3.1 Sample Preparation

Prior to either irradiation or material growth, samples were diced with a diamond scribe and cleaned with a series of solvents (acetone, methanol, methanol). Polypropylene tweezer should be used when handling semiconductors so as to avoid contamination from Ni diffusion. During cleaning, samples should be placed on the vacuum stage inside the fume hood. Rinsing in methanol followed by ethanol dissolves any residue left by the acetone. Samples are dried with a nitrogen gun before the ethanol can evaporate. Allowing any of the solvents to evaporate on the the surface will cause any dissolved debris to redeposit on the surface.

3.3 Aligning the laser for laser induced periodic surface structure formation

The standard experimental setup for HSFL formation is shown in Figure 3.3.1. The 20 cm lens is replaced with the longer 100 cm lens for multiple reasons. The error in peak fluence from the power meter reduces by an order of magnitude as well as the error in local fluence at the damage spot edge due to beam precession. Beam precession was measured on the WinCamD profiler to be ±1.5 μm. For multi-shot experiments, this leads to large fluctuations in the local fluence of 20% at the 1/e2 radius with the 20 cm lens but is washed out to 5% with the 100 cm lens. Moreover, the 100 cm lens increases the surface area covered in a uniform morphology for each experiment. Dwell times for multi-shot experiments are controlled with the shutter feature within the LabView program titled “Linear Motion.”

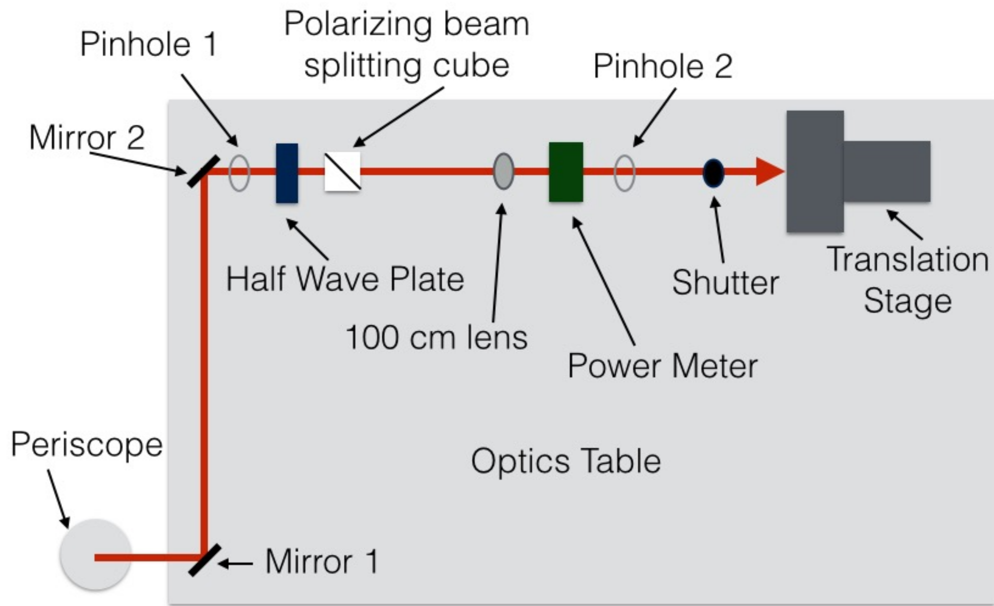

Figure 3.3.1 Experimental setup and relevant optics for HSFL formation with the fundamental wavelength.

For experiments at the frequency doubled wavelength, a beta-barium borate (BBO) crystal was placed inside the beam path. Light exiting the crystal is a mixture of both the fundamental and the frequency doubled wavelength so a blue filter was used to isolate the doubled light. The crystal orientation in x,y,z, and tilt were optimized by maximizing the power of the blue light. The 390 nm beam's polarization is rotated 90 degrees. The polarization was calibrated with a wire grid polarizer. When the crystal is tilted off axis, the polarization rotates at a small angle and makes interpreting results more difficult. A new crystal starts at ~33% efficiency but this value decreases over time as the BBO is exposed to air. For this reason, the crystal should be covered in a plastic bag when not in use to extend the lifetime of the component.

The full beam does not fit though the BBO crystal without clipping on the edges and must therefore be reduced with a 3:1 telescope. To align the telescope, first find the standard beam on the beam profiler. Then, insert the telescope and place the reduced beam onto the same location spatially on the beam profiler. Next, adjust the dispersion on the telescope until the beam has the same spatial profile as the original beam at the focal plane. The reduced beam leads to a larger focal spot with a shorter lens. In order to ensure that at least 1 J/cm^2 can be obtained with the doubled light after accounting for the poor conversion efficiency, experiments were conducted with a 20 cm focal length lens in this setup. A schematic of the standard 2nd harmonic generation setup is provided in Figure 3.3.2.

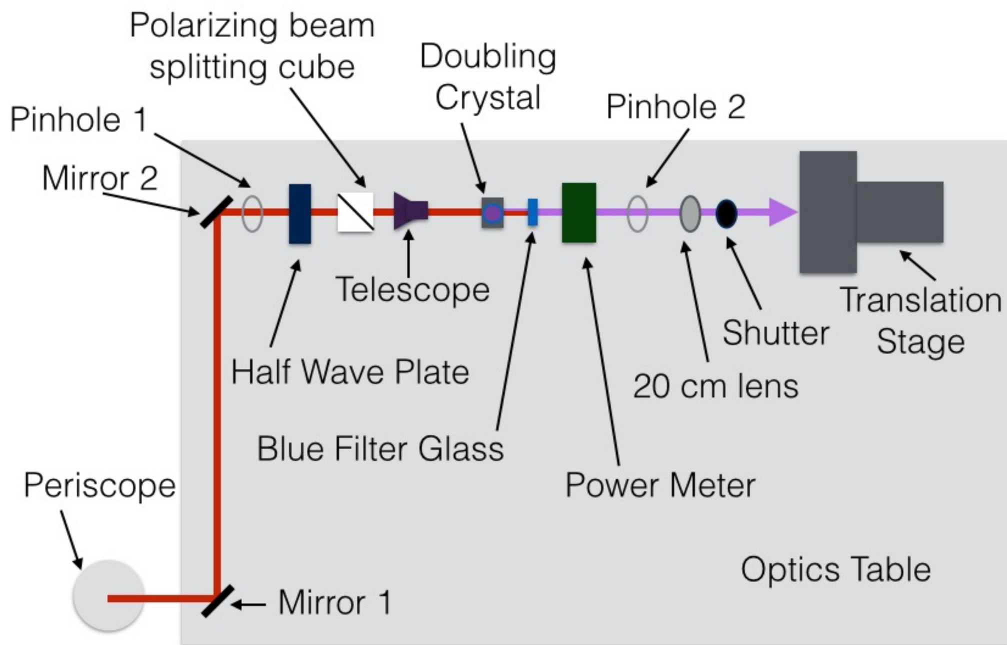

Figure 3.3.2 Experimental setup and relevant optics for frequency doubled irradiation

3.4 Thin Film Deposition

Ni thin films were grown on 140 µm thick glass cover slips using a DC Magneton sputtering system operated in continuous rotation mode. A sputter power of 200 W, Ar pressure of ~2 motor, and base pressure of ~ $4x10^{-3}$ mTorr were used for each run. Film thickness was varied between 5 and 20 nm. A sputter rate of 8 nm/min had been previously calibrated using Rutherford backscattering spectroscopy. The stability of this calibration was confirmed by measuring the depth of laser ablation craters in atomic force microscopy (AFM) that separated at the Ni/glass interface.

3.5 Nanoparticle Collection

Nanoparticles were printed onto substrates in air, using a variation of the Laser Induced Forward Transfer (LIFT) technique [Bera 2007, Banks 2006]. Irradiation was performed in a top-down configuration by placing a periscope mirror into the beam path. Alignment of this mirror was performed by placing a reflective surface beneath the mirror on the optics table and then aligning the back-reflection. The Ni thin films from section 3.4 were placed into the apparatus shown in Figure 3.5.1 such that the beam passed through the glass side first. A TEM grid was placed beneath the film to catch the nanoparticles after they were ejected from the substrate. It should be noted that carbon film grids are ideal for particle distribution as they collect all of the formed nanoparticles, which reduces the amount of time spent looking for enough particles to

generate a distribution. Holey carbon grids are needed for electron energy loss spectroscopy because particles on carbon do not produce sufficient signal to noise. The holey carbon grids also have a higher threshold to damage from the impacting particles during printing.

3.7 Finite Element Frequency Domain Simulations

Frequency domain finite element simulations were performed by propagating a Gaussian beam through air toward a semi-infinite GaAs bulk. Reflections from the box boundaries were prevented using a perfectly matched layer and a perfect electrical conductor at the air boundaries and absorbing boundary conditions for the GaAs. The GaAs layer was modeled using a dielectric function calculated from an expression for an optically excited semiconductor given by Equation 3.7.1 [Sokolowski-Tinten, 2000]:

$$\varepsilon = 1 + [\varepsilon_g(\hbar\omega + \Delta E_{gap}) - 1] * Ng - \omega_p^2/(\omega(\omega + i\Gamma)$$

(Equation 3.7.1)

where ε_g is the ground state dielectric function [Palik, 1985], ΔE_{gap} is a term for band-gap renormalization, Ng is the fraction of valence electrons in the ground state, ω_p is the plasma frequency, and Γ is the electron collision frequency. The frequency domain calculations [COMSOL] require that you input the refractive index of the excited material into the material parameters. The complex refractive index can be calculated from the dielectric function using Equations 3.7.2 and 3.7.3:

$$n = [(|\varepsilon_{complex}| + \varepsilon_{real})/2]^{1/2}$$

(Equation 3.7.2)

$$k = [(|\varepsilon_{complex}| - \varepsilon_{real})/2]^{1/2}$$

(Equation 3.7.3)

where n is the real part of the refractive index, k is the extinction coefficient, $\varepsilon_{complex}$ is the complex dielectric function, and ε_{real} is the real part of the dielectric function. The Gaussian beam polarized in the x direction is input into the simulation using Equation 3.7.4:

$$E_{bx} = E0*(w0/Beam_Waist(y))*exp(-z^2/Beam_Waist(y)^2)*exp(j*(k*y +k*z^2/Piecewise_Curvature(y))+atan(y/z0)))$$

(Equation 3.7.4)

where E_{bx} is the background field in x, E0 is the initial field, w0 is the focussed beam radius, k and j are wave vectors, and z0 is the Rayleigh range. Beam_waist(y) is calculated using equation 3.7.5:

$$Beam_waist(y) = w0*sqrt(1 + (y/z0)^2)$$

(Equation 3.7.5)

and Piecewise_Curvature(y) describes the wavefront curvature using equation 3.7.6:

$$Piecewise_Curvature(y) = \begin{cases} y*(1+(z0/y)^2) & \{-1e10*z0 < y \leq 1e8*z0\} \\ 1e8*z0 & \{-1e8*z0 < y \leq 1e8*z0\} \\ y*(1+(z0/y)^2) & \{1e8*z0 < y \leq 1e10*z0\} \end{cases}$$

(Equation 3.7.6)

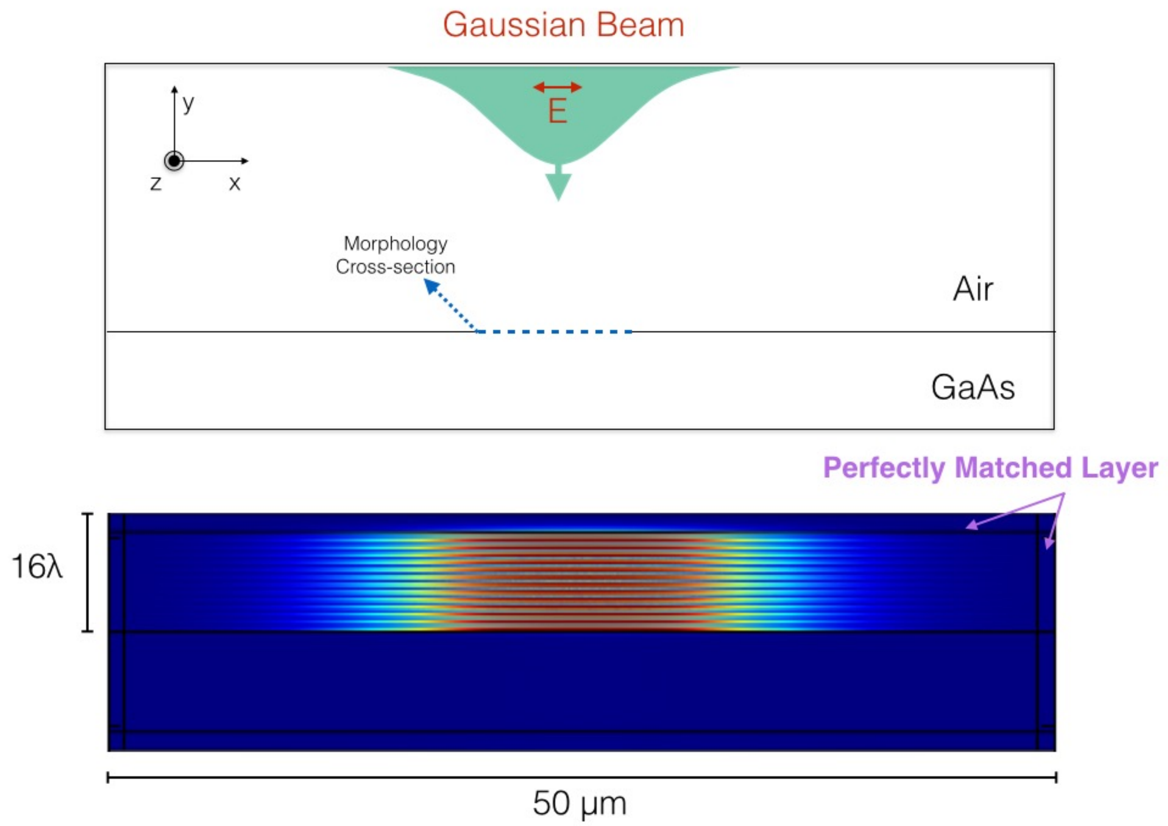

Figure 3.7.1 Simulation box for frequency domain finite element analysis simulations

References

J. Bonse, S. Baudach, J. Kruger, W. Kautek, and M. Lenzner, Appl. Phys. A. **74**, 19 (2002).

S. Bera, A. J. Sabbah, J. M. Yarbrough, C. G. Allen, and B. Winters, Applied Optics **46**, 4650 (2007).

D. P. Banks, C. Grivas, J. D. Mills, I. Zergioti, and R. W. Eason, Appl. Phys. Lett. **89**, 193107 (2006).

https://www.youtube.com/watch?v=vNOpzDViAhE

*K. Sokolowski-Tinten and D. Von der Linde, Phys. Rev. B. **61**, 2643 (2000).*

E. D. Palik, in Handbook of Optical Constants of Solids, edited by E.D. Palik (Academic, New York, (1985).

Chapter 4

Laser Induced Periodic Surface Structures in Semiconductors

Ultrafast laser irradiation is well known to produce two different populations of laser induced periodic surface structures (LIPSS) in semiconductors. The two populations are typically differentiated by their period as being either low spatial frequency LIPSS (LSFL) with periods between 0.4 and 1.0 times the laser wavelength or high spatial frequency LIPSS (HSFL) with periods less than 0.3 times the laser wavelength. The HSFL always form at lower fluences than the LSFL [Bonse, 2012]. In this chapter, we will determine the physical significance of the threshold fluence for the transition between LSFL and HSFL. Furthermore, the minimum threshold for HSFL formation will be tied to the band-gap collapse threshold discussed previously in Chapter 2.1.2.

From our understanding of the material response within this range of fluences, we then develop a model for ultrafast point defect generation. The final section of this chapter shows that the predominately single crystal structure of the HSFL is consistent with a point defect diffusion based model of formation.

Section 4.1 Fluence Dependence of laser induced periodic surface structures in semiconductors

Building an understanding of HSFL formation requires us to first investigate the effects of a single exposure. The ultrafast laser/materials response in GaAs has been well characterized, and was thus chosen as the focus of our experiments [Saeta, 1991; Glezer, 1995a; Glezer, 1995b; Sokolowski-Tinten 1995; Sundaram, 2002]. Damage morphologies from ultrafast laser irradiation are also well known to be fluence dependent and have deterministic thresholds [Pronko, 1998]. We experimentally determined single exposure laser damage thresholds by

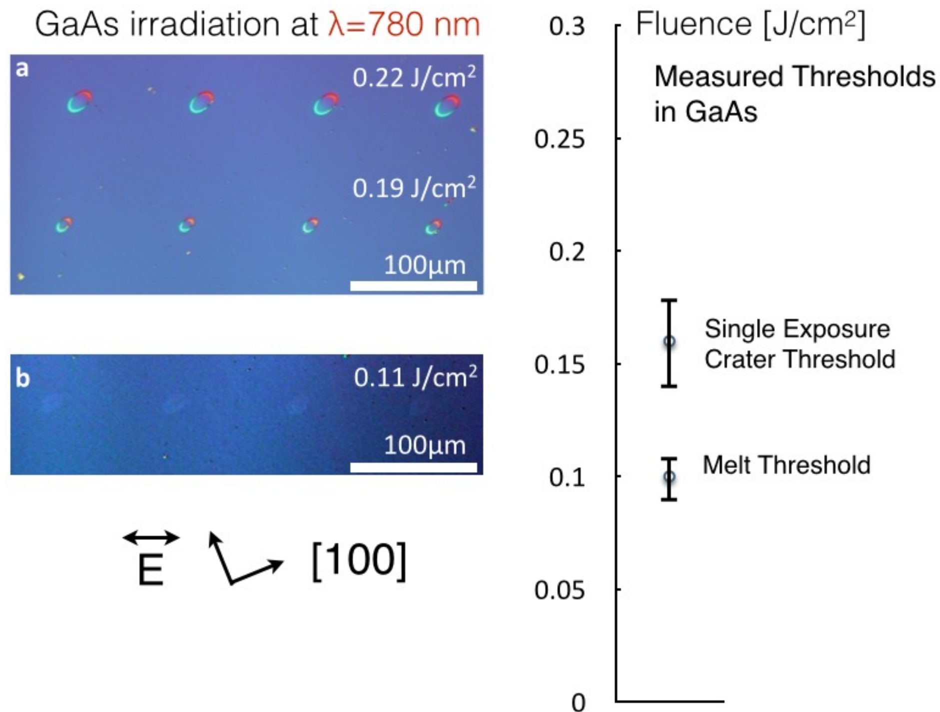

Figure 4.1.1 Differential interference contrast optical images of single exposure a) material removal and b) melt and amorphous resolidification. The single exposure threshold for material removal is 0.17 ± 0.02 J/cm2 and 0.09 ± 0.01 J/cm2 for melt. The melt threshold represents the maximum fluence at which HSFL form.

plotting the relationship between a specific optical contrast and fluence. The bulk GaAs damage thresholds were determined using the same method outlined in Chapter 3.3.

There are two optically visible single exposure damage thresholds shown in Figure 4.1.1 for GaAs. Our measured single exposure material removal threshold for GaAs is 0.17 ± 0.02 J/cm^2. Craters above this threshold were imaged using differential interference contrast in Figure 4.1.1. The top row of craters in Figure 5.1.1 formed at a peak fluence of 0.22 ± 0.02 J/cm^2 have a larger area than those in the row below at 0.19 ± 0.02 J/cm^2. This occurs because the beam does not have a uniform fluence across its spatial profile. Instead, the local fluence across a single laser spot has a Gaussian spatial distribution. The crater size is therefore determined by the distance at which the local fluence equals the threshold fluence. The crater size uniformity within a row in Figure 4.1.1(a) demonstrates the repeatability of this process within a given day. The reported error in each of our studies is equivalent to the measured day to day variation in the fluence necessary to create a specific morphology that arises based on the performance of our laser's internal optics.

The second damage morphology occurs below the material removal threshold in GaAs that corresponds to melting and amorphous resolidification after a single exposure [Crawford, 2008; Saeta, 1991]. This melt threshold refers to the ultrafast melting covered in Chapter 2.1.2. The amorphous phase is visible optically in Figure 4.1.1(b). Our measured threshold for this contrast is 0.09 ± 0.01 J/cm^2. This value is also consistent with the ultrafast melt threshold reported within the literature [Sundaram, 2002].

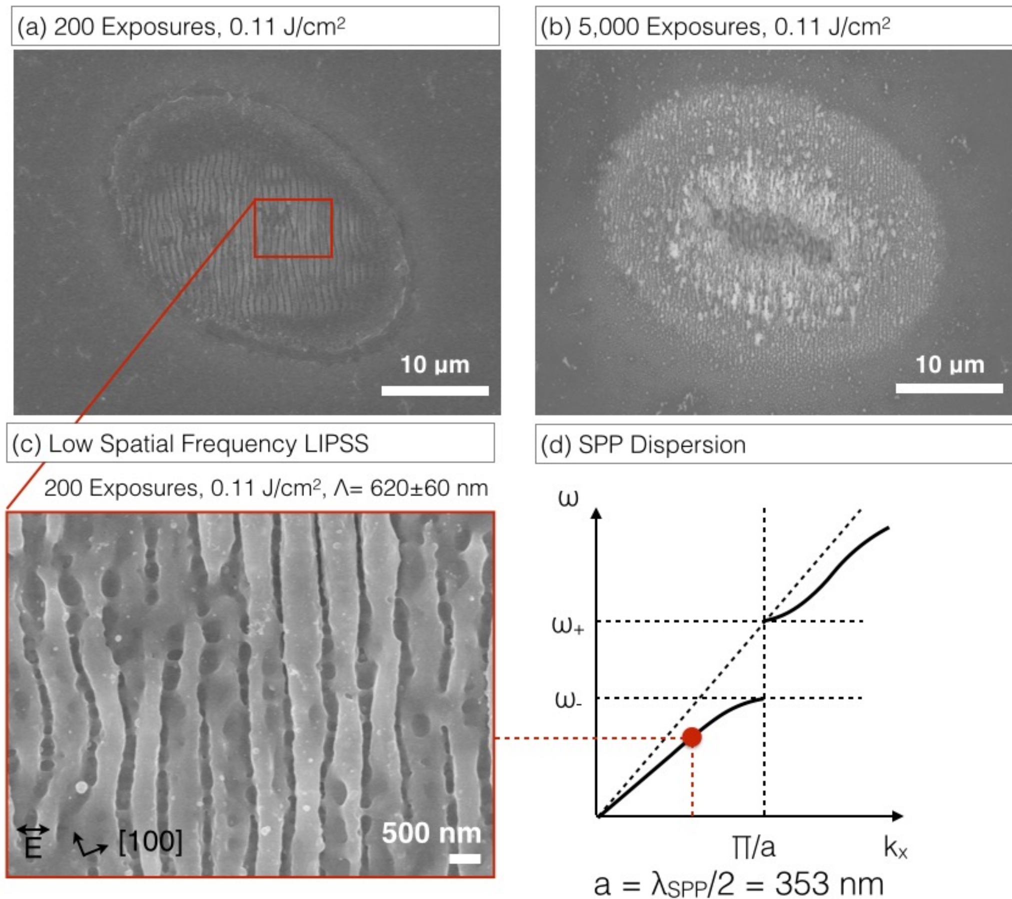

Figure 4.1.2 SEM of LSFL in GaAs formed at 0.11 J/cm^2 after (a) 200 exposures. Above the melt threshold, material is removed during LSFL formation, which can be seen in the crater formation after 5,000 exposures in (b). HSFL around the crater are observed at lower local fluence within the Gaussian laser damage spot. The LSFL after 200 exposures have a spacing of 620 ± 60 nm, which places them on the lower branch of the SPP dispersion curve shown in (d).

Multiple exposures above the melt threshold produced LSFL in GaAs. The LIPSS align perpendicular to the laser polarization regardless of the crystal orientation. The LIPSS form via selective ablation where the local field of a surface plasmon polariton is most intense [Huang, 2009; Murphy, 2013]. The perpendicular LIPSS first become visible after 200 exposures as shown in Figure 4.1.2(a), which represents the number of exposures necessary for the crater edge to be able to tall enough to couple to the SPP [Huang, 2009; Murphy 2013]. Continued exposures

ablate material until a crater is clearly visible in Figure 4.1.2(b). A LIPSS period of 620 ± 90 nm after 200 exposures at 0.11 ± 0.01 J/cm^2 shown in Figure 4.1.2(a) and (c) was calculated by taking histogram of the spacings of contained within the SEM images.

To understand the origin of the LSFL period, we must determine the SPP response based on the excited dielectric function of the GaAs. The GaAs layer was modeled using a dielectric function calculated from an expression for an optically excited semiconductor given by [Sokolowski-Tinten, 2000]:

$$\varepsilon = 1 + [\varepsilon_g(\hbar\omega + \Delta E_{gap}) -1] * Ng - \omega_p^2/(\omega(\omega+i\Gamma)$$

(Equation 4.1.1)

where ε_g is the ground state dielectric function [Palik, 1985], ΔE_{gap} is a term for band-gap renormalization, Ng is the fraction of valence electrons in the ground state, ω_p is the plasma frequency, and Γ is the electron collision frequency.

Ultrafast melt occurs when ~10% of the valence electrons are excited [Stampfli, 1990]. Above the melt threshold, it is valid to assume that $\omega_p^2/(\omega(\omega+i\Gamma) >> [\varepsilon_g(\hbar\omega + \Delta E_{gap}) -1] * Ng$ [Huang, 2009] causing the material to behave like a Drude metal. Γ is typically on the order of 1 fs for laser excited semiconductors.[6] For irradiation just above the melt threshold at 1.58 eV, the real part of the excited GaAs dielectric function was calculated to be -6.55. The SPP wavelength was calculated by [Barnes, 2003]:

$$\lambda_{SPP} = \lambda_{Laser} [(\varepsilon_{Re} + \varepsilon_{Air})/(\varepsilon_{Re} \cdot \varepsilon_{Air})]^{1/2}$$

(Equation 4.1.2)

where ε_{Re} is the real part of the dielectric function for the excited GaAs and ε_{Air} is assumed to be one. This resulted in an SPP wavelength of 718 nm just above the melt threshold.

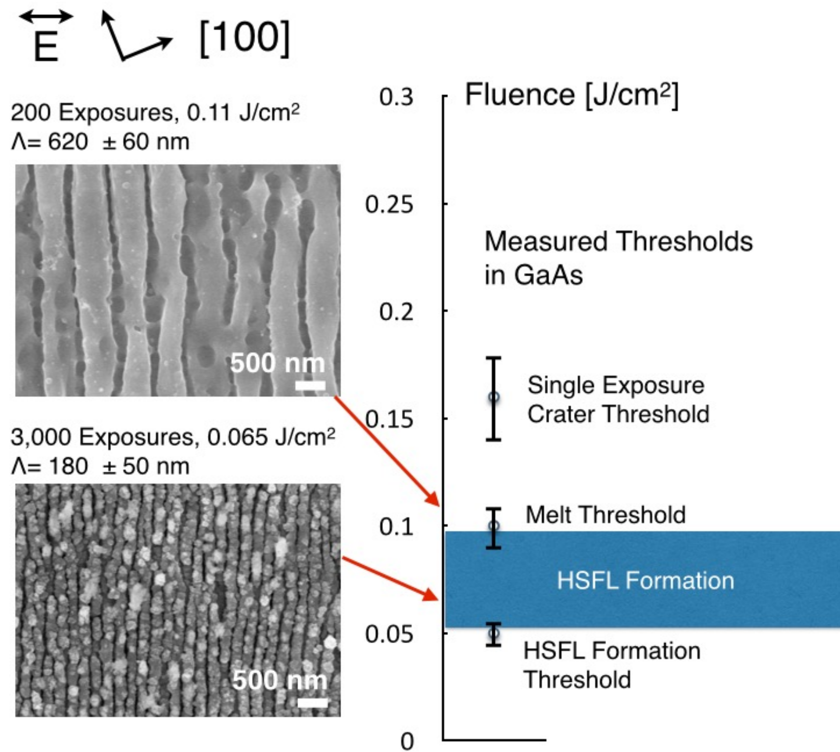

Figure 4.1.3 Representation of the measured thresholds in GaAs. Error bars represent the day to day variation of a specific threshold. (a) LSFL form after 200 exposures above the melt threshold at 0.11 ± 0.01 J/cm2 with period 590 ± 30 nm. Increasing the number of exposures does not produce HSFL (b) HSFL form after 3,000 exposures below the melt threshold and above a fluence of 5.0 ± 0.5 x 10^{-2} J/cm^2. Within this fluence range, the GaAs undergoes a transient order-disorder transition after each exposure. We propose that this is the range over which laser induced point injection is maximized and that accumulation of these defects is necessary for HSFL formation.

The LSFL formed after 200 exposures have a period less than the SPP wavelength. This difference is explained by the interaction between each exposure with grating-like surface formed by pre-existing LSFL [Huang, 2009; Bonse, 2012]. The coupling of SPPs to a grating allows a photonic band-gap to form in the polariton [Barnes, 1996]. For LSFL, increasing the trench depth after each exposure, moves the system along the lower branch of the SPP dispersion

curve [Huang, 2009]. The period after 200 exposures is represented schematically in Figure 4.1.2(d). It can be seen that LSFL period has a minimum at the band-edge of the SP-photonic band-gap, which is consistent with the shortest reported periods for LSFL [Huang, 2009].

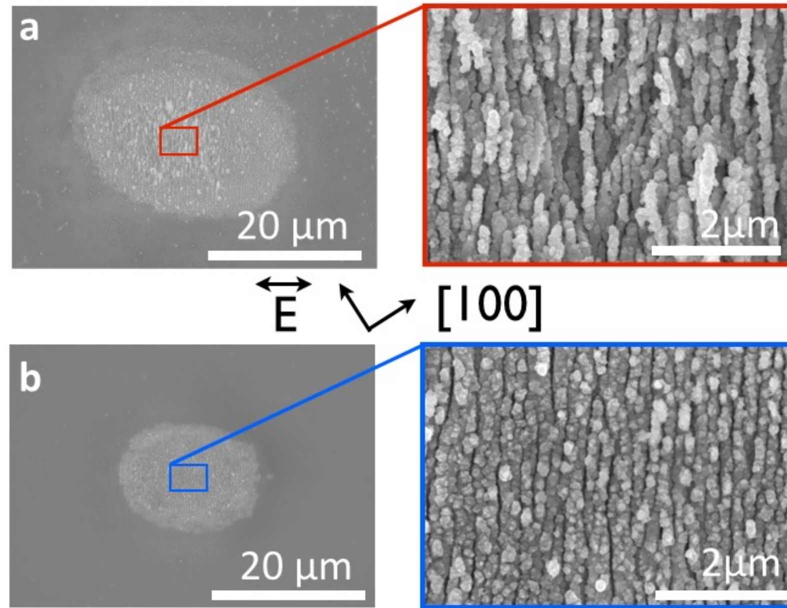

Figure 4.1.4 HSFL formation after 5,000 exposures at a peak fluence of (a) 8.0 ± 0.5 x 10^{-2} J/cm^2 and (b) 5.5 ± 0.5 x 10^{-2} J/cm^2. HSFL form perpendicular to the laser polarization and independent of crystal orientation. HSFL period of 180 ± 30 nm is fluence independent. The trenches between LIPSS are more prominent at higher fluence.

The 620 nm LIPSS are no longer observed below the melt threshold. LIPSS formed below the melt threshold have periods less than λ_{laser} /3 and hillocks on their surfaces in Figures 4.1.2 and 4.1.3. Irradiation with 5,000 exposures at a peak fluence of 0.080 ± 0.005 J/cm^2 produces HSFL on the order of 180 ± 50 nm in Figure 5.1.3a perpendicular to the laser polarization. HSFL formation occurs independent of the crystal orientation relative to the beam polarization. This result is consistent with previous studies on HSFL formation [Borowiec, 2003]. The trenches between LIPSS are not as well defined at 0.055 ± 0.005 J/cm^2 but the structures' period remains unchanged in Figure 4.2.3(b). Further reducing peak fluence to 0.045

± 0.005 J/cm^2 did not cause detectable changes to the GaAs surface morphology in SEM even after increasing the number of exposures to 1,000,000. A threshold for HSFL formation of 0.050 ± 0.006 x 10^{-2} J/cm^2 was calculated by measuring the local fluence at the edge of the SEM contrast of the entire damage spots like those in Figures 4.1.3(a) and (b). This fluence range for HSFL formation corresponds to values between the ultrafast-melt and band-gap collapse thresholds in GaAs that were discussed in Chapter 2.1.2.

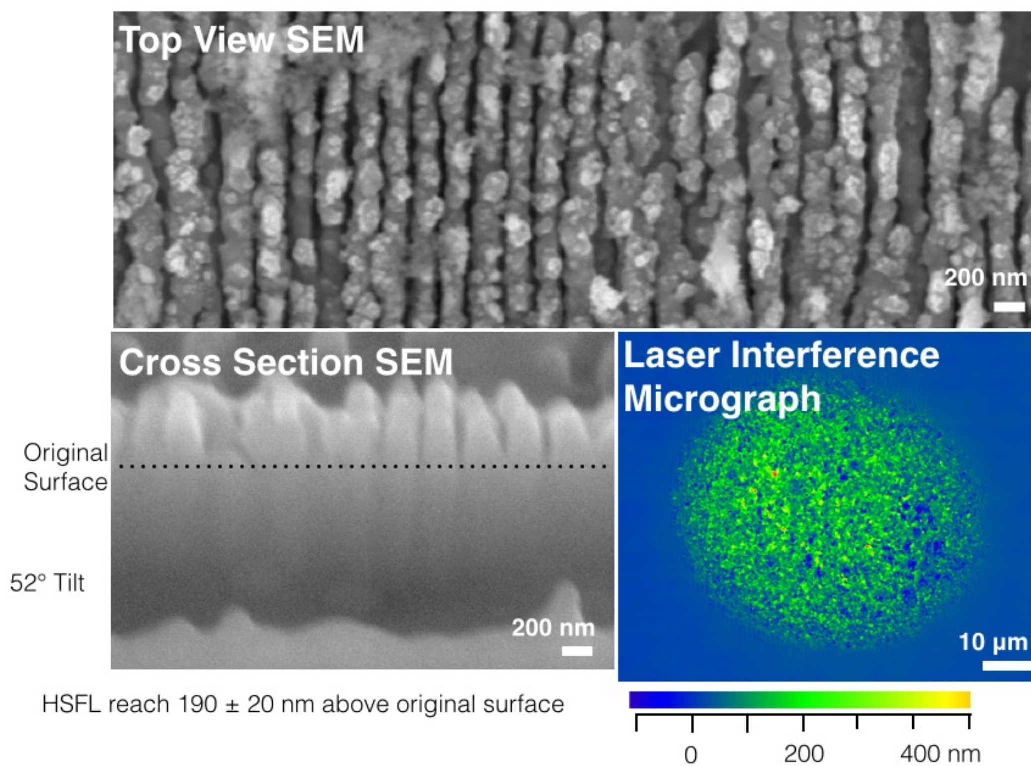

Figure 4.1.5 The HSFL form from a redistribution of mass above the original semiconductor surface. SEM of HSFL formed after 1,500 exposures in (a) top view, (b) at a 52 degree angle in cross section. The HSFL rise 190 ± 20 nm above the original surface. This measurement was confirmed in (c) laser interference microscopy. Both techniques produced consistent HSFL height.

Another defining feature of semiconductor HSFL is that their peaks reside above the original surface. Figure 4.1.5 shows that HSFL rise above the original surface 190 ± 20 nm after 1,500 exposures at 0.065 ± 0.005 J/cm^2. The measurement was determined with two corroborating techniques that yielded consistent results. The marked original surface in Figure

4.1.5(a) was determined by cutting a trench that extended outside the damage spot and then using the beam shift to move across the spot. The laser interference micrograph in Figure 4.1.5(b) does not produce accurate lateral resolution due to the visible light diffraction limit being far larger than the feature size. However, the technique has 20 nm height resolution so the average structure height is still accurate. Unlike semiconductor LSFL [Huang, 2009] and HSFL in dielectrics [Bhardwaj, 2006], semiconductor HSFL do not form from a selective ablation mechanism. Instead, these positive relief structures form due to mass redistribution of laser generated point defects.

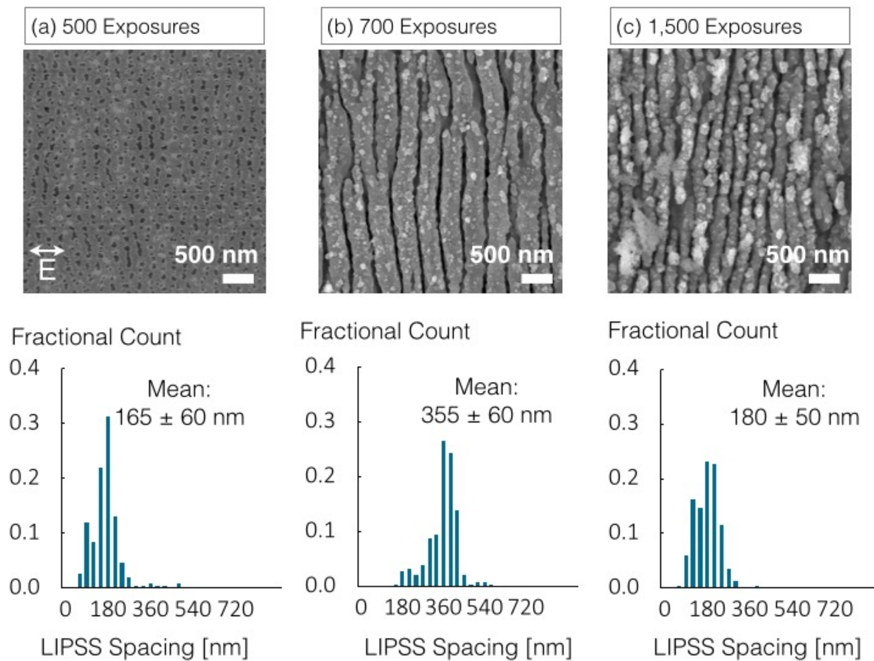

Figure 4.1.6 SEM and corresponding histograms of intermediate LIPSS periods in the laser polarization direction during HSFL formation at 0.065 J/cm^2. LIPSS have a period of 165 ± 60 nm after 500 exposures in (a), 355 ± 60 nm after 700 exposures in (b), and 180 ± 50 nm in (c).

The HSFL evolve through multiple intermediate periods. LIPSS periods were determined from the mean values of the histograms of the feature spacings in the direction of the polarization shown in Figure 4.1.6. The reported error is equivalent to the standard deviation of the measured

distributions. The LIPSS begin with the 165 ± 60 nm period shown in Figure 4.1.6(a). The island precursors to this population will be the focus of Chapter 5 of this thesis. The LIPSS then transition to a longer 355 ± 60 nm period shown in Figure 4.1.6(b). Finally, the LIPSS reach an period of 180 ± 50 nm, between those of the two intermediate populations, as shown in Figure 4.1.6(c). The coupled mechanism involving strain relaxation and the SPP response that cause the transitions between these LIPSS periods will be the focus of Chapter 6 of this thesis.

In summary, we have determined that perpendicular HSFL in semiconductors only form at fluences between the ultrafast-melt and band-gap collapse thresholds. Above this range only LSFL are observed while no morphological changes occur below these fluences. While the LSFL are negative relief features, the HSFL evolve due to mass redistribution above the original surface.

4.2 Point defects and high spatial frequency laser induced periodic surface structures

The true impact of the HSFL is that they are a morphological change to a semiconductor that arise from the dynamical pathway the material takes back from the extreme non-equilibrium state of the ultrafast laser excited material. In this section, we will examine how an excited non-fermi distribution of electrons can lead to a uniquely ultrafast mechanism for point defect generation.

The HSFL evolution process is set in motion by a repeated laser material interaction that only lasts 150 femtoseconds per exposure. In addition, the HSFL only form at fluences that correspond to the range below the ultrafast-melt threshold and above the band-gap-collapse threshold [Glezer, 1995a; Glezer, 1995b; Sundaram, 2002]. At these fluences, semiconductors are remarkably resilient to intense ultrashort laser pulses and appear to completely recover their original dielectric properties after each laser exposure [Glezer, 1995a; Sundaram, 2002] even though each interaction excites almost 10 % of the valence electrons [Graves, 1998]. At this level of excitation, the band-structure collapses and the conductivity increases by more than 7 orders of magnitude [Schultze, 2014]. We propose that exciting a semiconductor at these fluences leads to an ultrafast generation of vacancy/interstitial pairs.

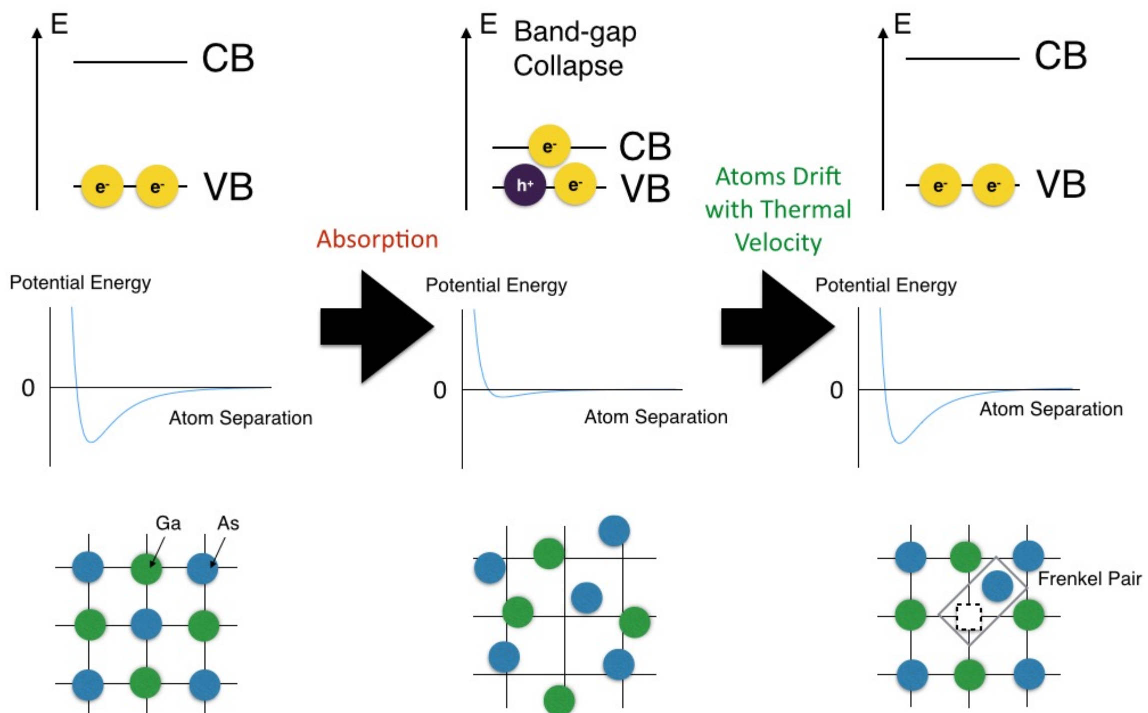

Figure 4.2.1 Schematic of ultrafast point defect formation in semiconductors

The connection between ultrafast laser induced excitation at these intensities and atomic motion was determined through pioneering time-resolved X-ray diffraction experiments [Rousse, 2001; Lindenberg, 2005; Fritz, 2007], confirming earlier theoretical work [Graves, 1998], demonstrating that the root-mean-squared displacement can be as much as an angstrom within a few hundred femtoseconds following laser excitation. This is possible because the impulsive ultrashort laser interaction depopulates the bonding states, weakening the attractive part of the interatomic potential, allowing the ions to drift with their initial thermal momentum until they collide with nearby ions. At the ultrafast-melt threshold these collisions result in a permanent disordering of the crystal lattice within a picosecond. Just below this laser threshold the lattice appears to recover.

Although the average interatomic potential weakening at these fluences is not sufficient to allow all the ions to reach new sites, the Maxwellian distribution of the room temperature thermal momentum ensures that some atoms will have initial conditions such that their motion is favorable for reaching an interstitial site. The interstitial site represents the real space location with the highest density of excited electrons after irradiation [Schultze, 2014], and thus represents a likely site for excited electrons to recombine with an ion core. A configurational change that forms a Vacancy/interstitial pair serves as a non-radiative pathway for the electrons to reoccupy bonding states. A schematic of the Vacancy/interstitial pair formation mechanism is shown in Figure 4.2.1. Repeating this process over multiple exposures causes defects to accumulate and reach a population inversion. The softened binding potential also increases mobility for previously generated defects. This both increases the probability of Vacancy/

interstitial pair dissociation and may enhance diffusivity of the resulting vacancies and self-interstitials.

This model for Vacancy/interstitial pair formation is consistent with collaborative work in which a nonadiabatic quantum molecular dynamics method [Graves, 1998; Allen, 2001] indicated that there is an ultrafast defect formation mechanism active between the ultrafast-melt and band-gap collapse thresholds [Abere, submitted 2015]. The quantum molecular dynamics calculation was based on the work of Graves [Graves, 1998] but it expanded the simulation to 216 atoms so that the crystal can support the formation of a point defect.

The proposed point defect injection mechanism is fundamentally different from the thermally generated point defects observed after nanosecond laser irradiation [Emel'yanov, 1992; Emel'yanov, 2007]. A nanosecond laser acts as a lattice heating source that serves to increase the equilibrium point defect concentration while rapid quench rates maintain their stability when the system returns to room temperature. While the laser electric field reduces the activation energy for defect formation, the process is dominated by thermal lattice heating.

We performed additional experiments in which we irradiated GaAs wafers with 1,000 exposures separated into two sets of 500 at a repetition rate of 1 kHz. The time between sets of 500 exposures has a direct impact on HSFL formation. LIPSS morphology remains unchanged and the 180 ± 50 nm population is observed after a 25 minute delay between sets of exposures in Figure 4.2.2(a). The 350 ± 30 nm LIPSS population forms almost exclusively after a 60 min long delay in Figure 4.2.2(b). Trenches are observed and all features align perpendicular to the laser polarization after a 90 minute delay shown in Figure 4.2.2(c). However, a defined LIPSS period is not observed.

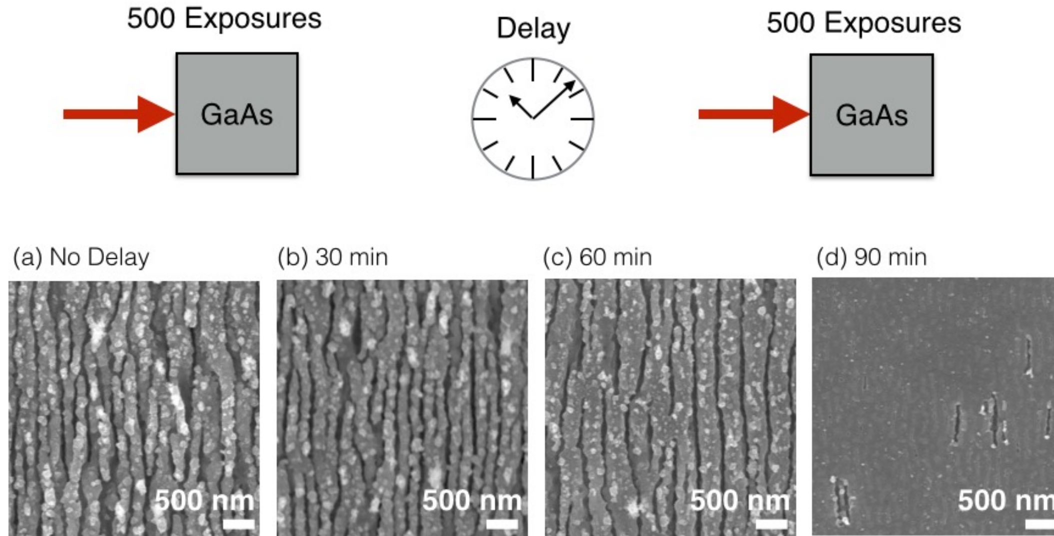

Figure 4.2.2 LIPSS evolution behavior is observed after two sets of 500 exposures separated by a time delay and peak fluence 0.065 ± 0.005 J/cm^2. The experiment tests our point defect model by allowing the accumulated defects to annihilate via diffusion. Increasing the delay between the sets of exposures produces the same morphologies after 1,000 total exposures as reducing the dose delivered all at once. HSFL formation appears unchanged after a (a) 25 minute delay. Only the 355 nm population is observed after a (b) 60 minute delay. Trenches but no LIPSS are observed after a (c) 90 minute delay.

This study confirmed that the magnitude of the Vacancy/interstitial pair supersaturation is fundamentally tied to HSFL formation. When the sample was irradiated by a second set of 500 exposures, the resulting morphology was dependent on the delay between sets. By allowing defects to annihilate for 60 min in between sets of exposures, HSFL formation in Figure 4.2.2(b) after 1,000 total exposures only proceeds to the morphology observed after 700 exposures seen in Figure 4.1.6(b). Increasing the time for annihilation to 90 min in Figure 4.2.2(d) prevents sufficient defect accumulation for the formation of either LIPSS population. The impeded LIPSS formation is consistent with both an generated defect lifetime on the order of hours and that the

process is concentration dependent. A control experiment using a 500 nm GaAs buffer layer grown in molecular beam epitaxy was also performed to ensure that HSFL formation did not depend on carbon impurities [Kang, 2013] in the as received wafers.

In summary, we have identified that the fluence range between band-gap collapse and ultrafast melt represents the necessary electron excitation to reach a population inversion of Vacancy/interstitial pairs to set the HSFL formation process in motion. The softened bonds not only allow defects to form, but also reduce the barriers to mass transport on subsequent exposures. Finally, the defect concentration, and resulting lattice strain, is directly related to the stage to which HSFL evolution will progress.

4.3 Structural characterization of high spatial frequency periodic surface structures in semiconductors

Typical ultrafast laser induced nanostructures contain an amorphous layer as thick as the melt depth during ablation. These include both black Si spires [Serpenguzel, 2008] and LSFL [Coyne, 2004]. The HSFL never melt during formation and thus we would expect their structural properties to reflect this difference.

The 180 nm HSFL formed after 1,500 exposures are shown in the cross-section transmission electron microscopy (TEM) images in Figures 4.3.1 through 4.3.4. A conventional bright field TEM image of the HSFL is provided in Figure 4.3.1(a). A typical STEM energy dispersive x-ray spectrum from within the HSFL is provided in Figure 4.3.1(b). The peak ratio

between Ga and As is equivalent to a standard spectrum taken in the same microscope with a consistent acquisition time and indicates a 1:1 composition. Figure 4.3.1(c) contains a selected area diffraction pattern from the top of a structure with the GaAs (111) reflection labelled. An arrow points to a high angle grain boundary at 43°, which suggests the presence of twin boundaries within the structures.

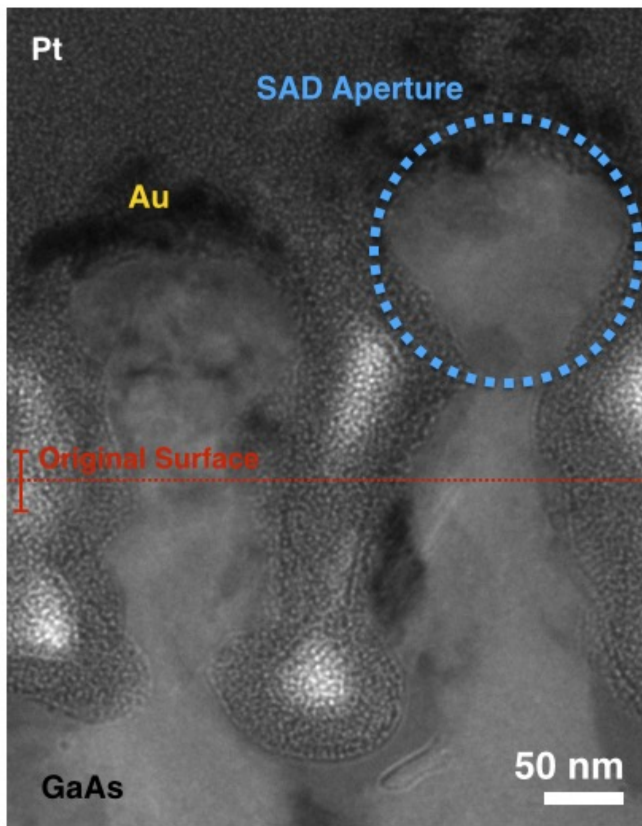

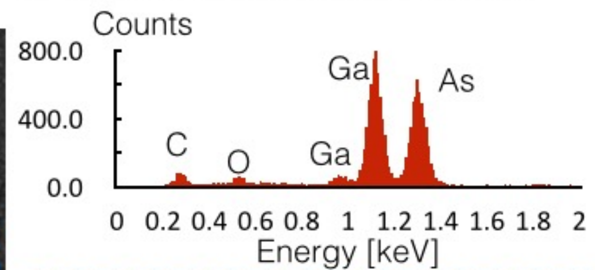

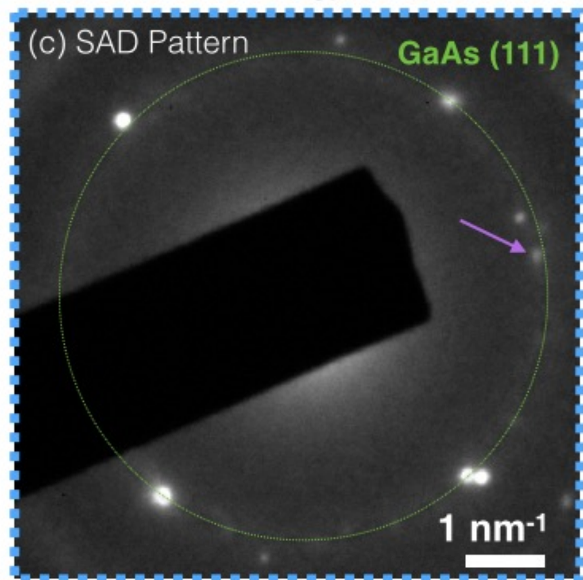

Figure 4.3.1 (a) Bright field TEM of HSFL. (b) Typical STEM-EDS spectrum showing that HSFL are composed of stoichiometric GaAs. (c) Selected area diffraction pattern from the top of a structure focussing on the GaAs (111) reflection. The strained polycrystal is consistent with the STEM images in Figure 5.3.2.

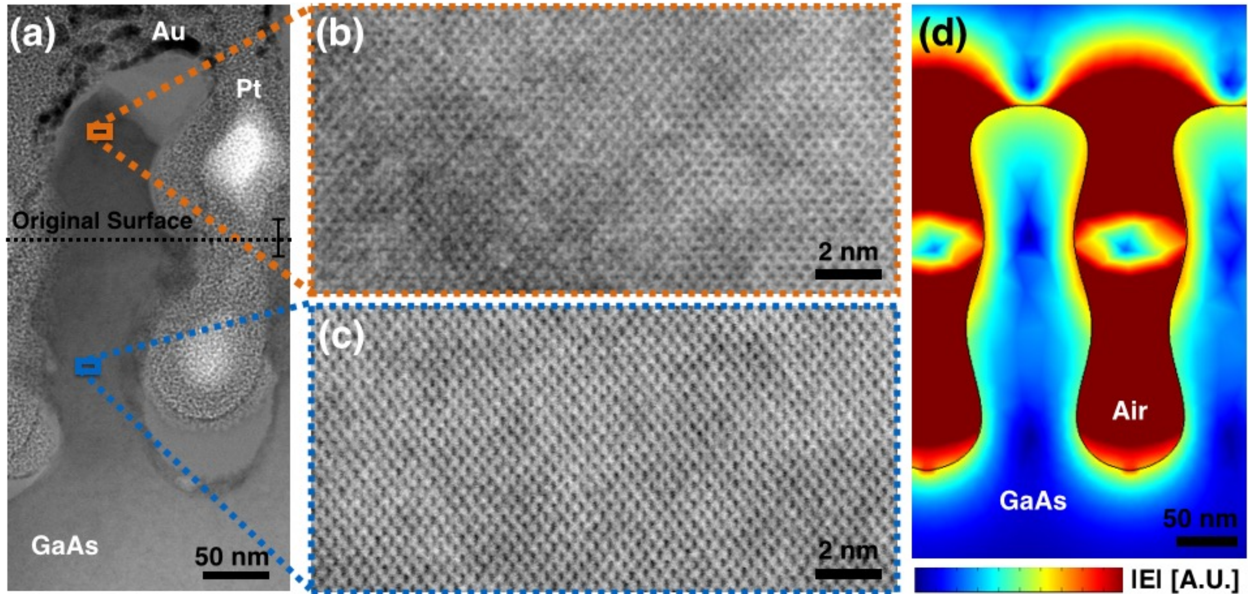

Figure 4.3.2 (a) Bright Field STEM image of HSFL along the [110] zone axis. Structures were covered in Au and Pt to protect them from ion beam damage during sample preparation. The diffraction contrast within the HSFL corresponds to misoriented grains. The GaAs remains epitaxial 80 nm above (b) and below (c) the initial surface. A frequency domain finite element analysis calculation in (d) shows that the structures become polycrystalline where the local absorbed intensity is the highest.

The HSFL formed after 1,500 exposures were further characterized in bright field cross-section scanning transmission electron microscopy (STEM) images in Figure 5.3.2. The HSFL have an amplitude near 350-400 nm, which is an order of magnitude larger than those typical for LSFL in spite of forming at lower fluence [Huang, 2009]. The strained polycrystal from the selected area diffraction pattern in Figure 4.3.1(c) is consistent with the diffraction contrast in Figure 4.3.2(a). Further STEM characterization in Figure 5.3.2 shows that the central region of each structure remains epitaxial to the bulk. Images were taken along the [110] zone axis of the original GaAs. The single crystal region is continuous through both the region above the initial surface in Figure 5.3.2(b) and below in Figure 5.3.2(c). The increased mobility within the vacancy rich material is capable of growing at least 80 nm of epitaxial semiconductor material.

Highly misoriented nanocrystalline regions at the structure tops, sidewalls, and trench bottoms appear as light diffraction contrast in Figure 5.3.2(a). A frequency domain finite element analysis simulation [Comsol] in Figure 5.3.2(d) shows that the nanocrystalline regions correspond to the highest local absorbed intensity where defect generation is concentrated and likely represents regions where the defect generation rate exceeded vacancy mobility.

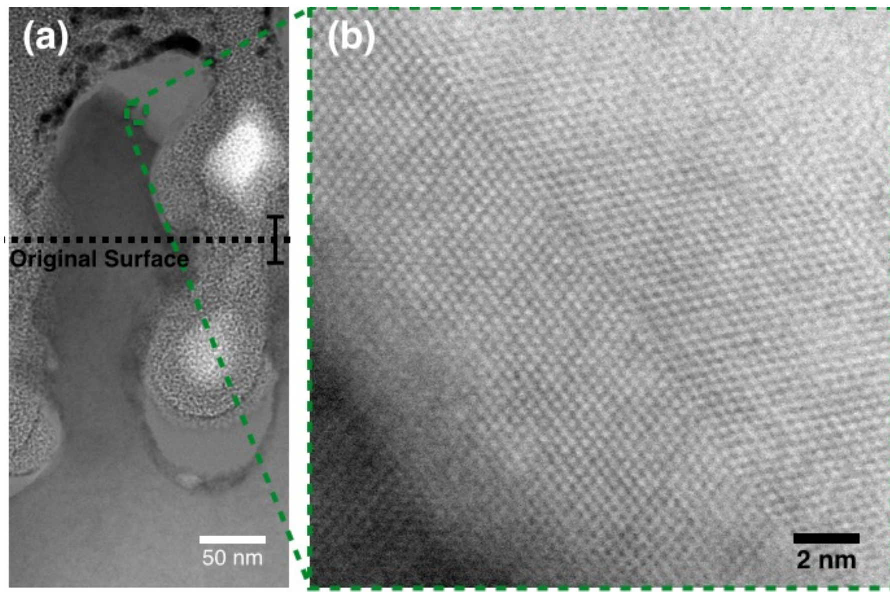

Figure 4.3.3 (a) Bright field cross-section STEM of HSFL (b) High resolution bright field STEM image of nanocrystal and twin boundary at the top of a single structure

Further characterization in STEM shows that the high angle grain boundaries observed in the selected area diffraction patterns in Figure 4.3.1(c) are in fact twin boundaries. The twin boundaries form within the polycrystalline regions at the top of the structures after 1,500 exposures and one such boundary is shown in atomic resolution bright field STEM in Figure 4.3.3. The coherent twins typically occur near the boundary between the epitaxial and nanocrystalline regions at the structure tops.

The HSFL show no evidence of Ga droplets on top of the structures. Ga droplets should form on the sample surface if thermal energy from multiple exposures had raised the temperature above 660°C [Goldstein,1976]. The polycrystalline tops to the HSFL are more characteristic of nanostructures produced during growth between 200°C to 350°C [Lilental-Weber, 1991].

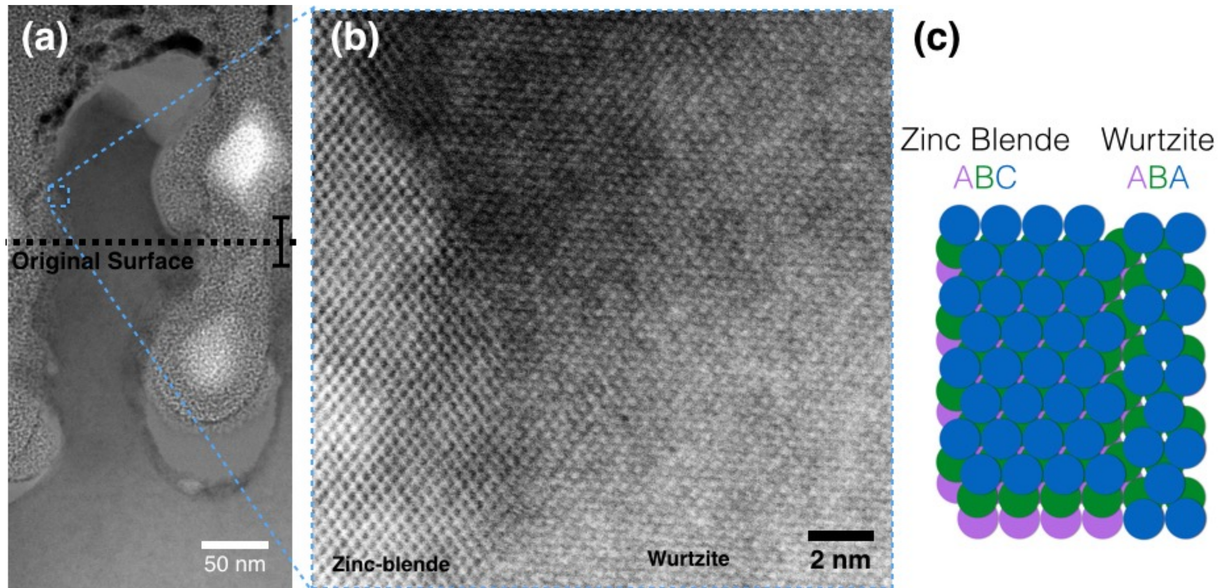

Figure 4.3.4 (a) Bright field cross-section STEM image of HSFL (b) High resolution image of grain boundary between zinc-blende and wurtzite-like grains at the edge of the structure (c) schematic showing the change in stacking order as the zinc-blende (111) planes become wurtzite spaced (100) planes.

HSFL growth is mass neutral so the structures must thin in order to become taller. This produces the changes in concavity along the structure sidewalls. A third region of high absorbed intensity occurs at the concave region of each structure when this curvature is incorporated into the frequency domain finite element analysis simulation in Figure 4.3.2(b). The atomic resolution image in Figure 4.3.4(b) shows that the structures become nanocrystalline at the edge of these concave regions. The grain on the right hand side of the image has an elongated d-spacing along one of the (111) directions. The other (111) bulk direction, however, remains unstrained. This

asymmetry at these d-spacings is consistent with the GaAs switching from ABC to ABA stacking to form a wurtzite-like grain. The strained zinc-blende (111) plane takes on the d-spacing of a wurtzite (100) plane. The wurtzite (002) plains remains lattice matched to the zinc-blende (111) plains at the grain boundary in Figure 4.3.4(b) as they have the same d-spacing [Cheiwchanchamnangij, 2011]. However, where we would expect the (101) d-spacing for wurtzite, the unique hybrid phase retains the original (002) d-spacing from the zinc-blende.

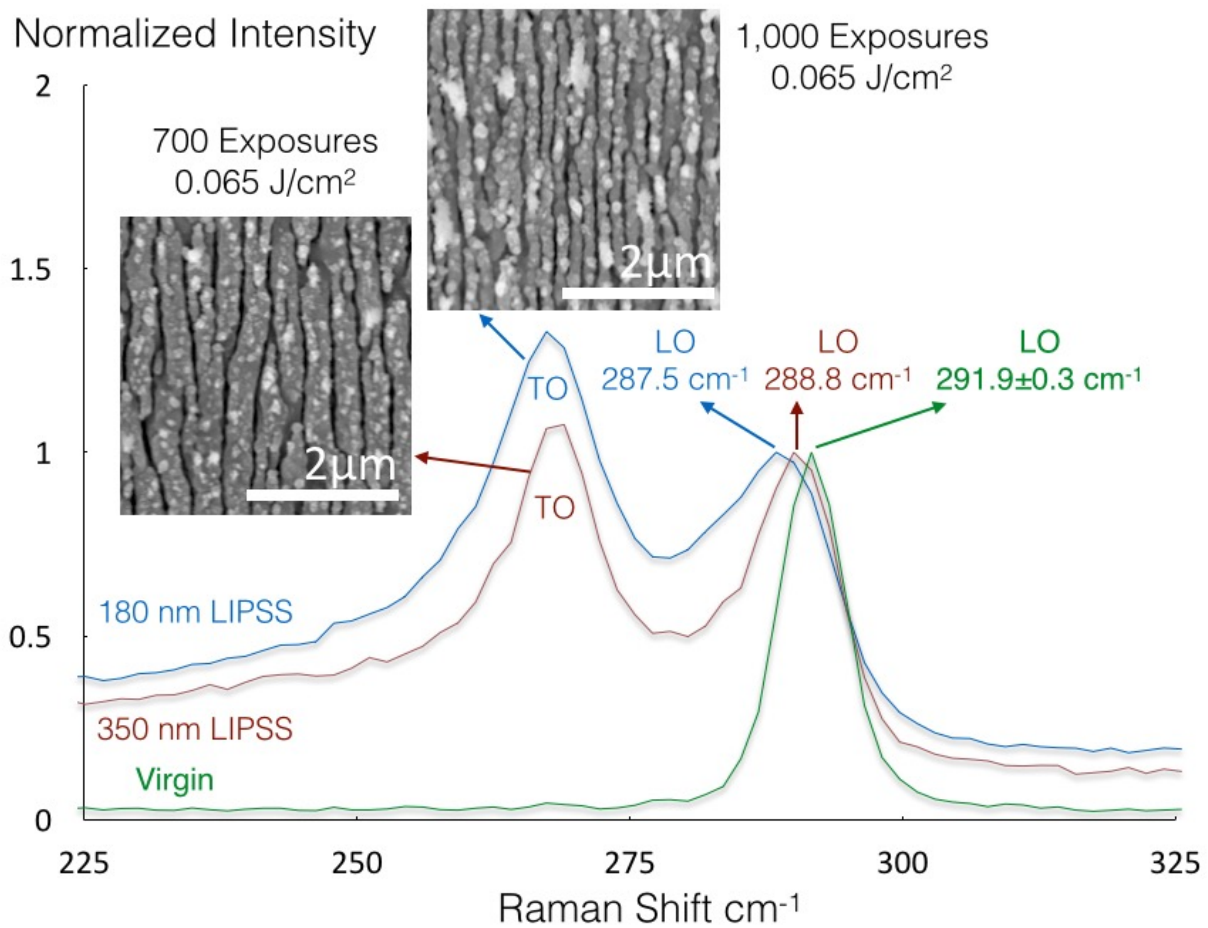

Figure 4.3.5 Raman spectroscopy from LIPSS in HSFL. The corrugation creates (111) surface making the transverse optical mode appear. A redshift and broadening of the longitudinal optical mode with increasing exposures occurs due to the formation of the wurtzite-like phase shown in Figure 4.3.4

The presence of increased d-spacing from wurtzite (100) stacked planes appears as a redshift in the longitudinal optical phonon. The Raman spectra in Figure 4.3.5 show that the wurtzite-like grains shift the longitudinal optical phonon by 1 cm^{-1} for the 355 nm LIPSS and by 2 cm^{-2} for the 180 nm HSFL. The peak from the longitudinal optical phonon is broader due to the presence of both phases. Another defining feature of the HSFL in Raman is the presence of the GaAs transverse optical phonon. While this mode is typically forbidden due to selection rules [Dmitruk, 2007] for the s-polarized beam, the corrugation creates (111) surface for the incident beam to couple to the transverse optical phonon. Consequently, the relative intensity of this mode increases by a factor of two when the HSFL bifurcate. The transverse optical mode does not undergo the same redshift as the longitudinal optical mode, which is consistent with the wurtzite-like grains remaining coherent with the bulk throughout the spot.

In summary, structural characterization shows that the 180 nm HSFL are predominately stoichiometric, epitaxial single crystals. Regions where absorption is highest are nanocrystalline. The nearly 300 nm of single crystal may have potential applications in optoelectronic devices as a means of increasing absorption through surface structuring without losing transport at grain boundaries.

References

J. Bonse, J. Kruger, S. Hohm, and A. Rosenfeld, *J. Laser App.* **24**, 042006 (2012).

P. Saeta, JK. Wang, Y. Siegal, N. Bloembergen, and E. Mazur, *Phys. Rev. Lett.* **67**, 1023 (1991).

EN Glezer, Y. Siegal, L. Huang, and E. Mazur, *Phys. Rev. B.* **51**, 6959 (1995).

EN Glezer, Y. Siegal, L. Huang, and E. Mazur, *Phys. Rev. B.* **51**, 9589 (1995).

K. Sokolowski-Tinten, J. Bialkowski, and D. von der Linde, *Phys. Rev. B.* **51**, 14186 (1995).

SK. Sundaram and E. Mazur, *Nat. Mater.* **1**, 217 (2002).

P.P. Pronko, P.A. VanRompay, C. Horvath, F. Loesel, T. Juhasz, X. Liu, and G. Mourou, *Phys. Rev. B.* **58**, 2387 (1998).

T.H.R. Crawford, J. Yamanaka, G.A. Botton, and H.K. Haugen, *J. Appl. Phys.* **103**, 053104 (2008).

M. Huang, F. Zhao, Y. Cheng, N. Xu, and Z. Xu, *ACS Nano.* **3**, 4062 (2009).

RD Murphy, B. Torralva, DP Adams, and SM Yalisove, *Appl. Phys. Lett.* **103**, 141104 (2013).

K. Sokolowski-Tinten and D. Von der Linde, *Phys. Rev. B.* **61**, 2643 (2000).

E. D. Palik, in Handbook of Optical Constants of Solids, edited by E.D.Palik (Academic, New York, (1985).

P. Stampfli, *Phys. Rev. B.* **42,** 7163 (1990).

WL. Barnes, A. Dereux, and T.W. Ebbesen, *Nature*. **424**. 824 (2003).

WL. Barnes, T.W. Priest, S.C. Kitson, and J.R. Sambles, *Phys. Rev. B.* **54**. 6227 (1996)

A. Borowiec, and H. K. Haugen, Appl. Phys. A. **79,** 521 (2004).

VR. Bhardwaj, E. Simova, PP. Rajeev, C. Hnatovsky, R.S. Taylor, DM. Rayner, and P.B. Corkum, *Phys. Rev. Lett.* **96**, 057404 (2006).

JS. Graves and RE. Allen, *Phys Rev. B.* **58**, 13627 (1998).

M. Schultze, K. Ramasheda, CD. Pemmaraju, S.A. Sato, D. Whitmore, A. Gandman, J.S. Prell, LJ. Borja, D. Prendergast, K. Yabana *et. al. Science.* **346**, 1348 (2014).

A. Rousse, C. Rischel, S. Fourmaux, I. Uschmann, S. Sebban, G. Grillon, Ph. Balcou, E. Forster, JP. Gelndre, P. Audebert, JC. Gauthiers, and D. Hulin. *Nature Lett.* **410.** 65 (2001).

AM. Lindenberg, J. Larsson, K. Sokolowski-Tinten, KJ. Gaffney, C. Blome, O. Synnergren, J. Sheppard, C. Caleman, AG. MacPhee, D. Weinstein *et al*. *Science*. **308.** 392 (2005).

DM. Fritz, DA. Reis, B. Adams, RA. Arke, J. Arthur, C. Blome, PH. Bucksbaum, AL. Cavalieri, S. Engemann, S. Fahy, *et al*. *Science*. **315**, 633 (2007).

R.E. Allen, T. Dumitricaˇ, and B. Torralva, in Ultrafast Physical Processes in Semiconductors, edited by K.T. Tsen (Academic, New York, 2001).

MJ Abere, B. Torralva, and SM Yalisove, *Science,* Submitted

V.I. Emel'yanov and P.K. Kashkarov, Appl. Phys. A. **55.** 161 (1992) **.**

V.I. Emel'yanov, S.V. Vintsents, and G.S. Plotnikov, *Journal of Surface Investigation-X-Ray Synchotron and Neutron Techniques,* **1**, 667 (2007).

M. Kang, A.A. Al-Heji, J.E. Lee, T.W. Saucer, S. Jeon, J.H. Wu, L. Zhao, A.L. Katzenstein, D.L. Sofferman, V. Sih, and R.S. Goldman, *Appl. Phys. Lett.* **103**, 101903 (2013).

A. Serpenguzel, A. Kurt, I. Ianic, J Carey, and E. Mazur, *J Nanophoton.* **2,** 021770 (2008).

E. Coyne, JP Magee, P. Mannion, GM O'Connor, and TJ Glynn, *Appl. Phys. A.* **81**, 371 (2004).

COMSOL Multiphysics 5.1

B. Goldstein and DJ. Szostak, and VS. Ban, *Surf. Sci.* **57**, 733 (1976).

Z. Liliental-Weber, W. Swider, K.M. Yu, J. Kortright, F.S. Smith, and A.R. Cawala. *Appl. Phys. Lett.* **58**, 2153 (1991).

T. Cheiwchanchamnangij and WRL Lambrecht, *Phys. Rev. B.* **84**, 035203 (2011)

N. Dmitruk, S. Kutovyi, I. Dmitruk, I. Simkiene, J. Sabataityte, and N Berezovska, *Sensors and Actuators B: Chemical, Functional Materials for Micro and NanosystemsEMRSContaining Selected papers from the European Materials research Society (E-MRS 2006) Symposium G:* **126**, 294 (2007).

Chapter 5

Island Precursors to High Spatial Frequency Laser Induced Periodic Surface Structures in Semiconductors

The ability to form nanodots on surfaces has long generated interest as a means to improve optoelectronic devices by enhancing absorption through quantum confinement [Kamat, 2008; Nozik, 2002; Nozik, 1985] or coupling to surface plasmons [Pillai, 2007; Deckman, 1983]. Nanodots are commonly deposited by lithography [Masuda, 1996] or physical vapor deposition [Valeev, 2010]. Nanodots are also grown using molecular beam epitaxy (MBE) [Oskam, 2002] or ion beam bombardment [Böttger, 2013]. Nanodot formation and coarsening are observed on ZnSe surfaces as nanoscale Se clusters on epilayers grown in metal organic chemical phase deposition [Zhang, 1999] and SeO_2 clusters formed after exposing MBE grown epilayers to atmosphere [Smathers, 1998]. These techniques are all either time consuming, require multiple steps, or cannot be performed at ambient temperature and pressure. Laser based techniques have the speed and scalability for roll-to-roll processing [Ahn, 2008] and can be performed in air at ambient temperature and pressure.

While nanodots sometimes form independently of HSFL, they always serve as precursors to HSFL in semiconductors. Reducing the number of exposures at HSFL formation fluences leads to the formation of nanodots on semiconductor surfaces. SEM images of these nanodots are shown for ZnSe and GaAs in Figure 5.0.1 (a) and (b) respectively. This chapter will focus on the

formation and characterization of ultrafast laser generated nanodots and then show how they are fundamentally different from more commonly studied laser induced nanoparticles.

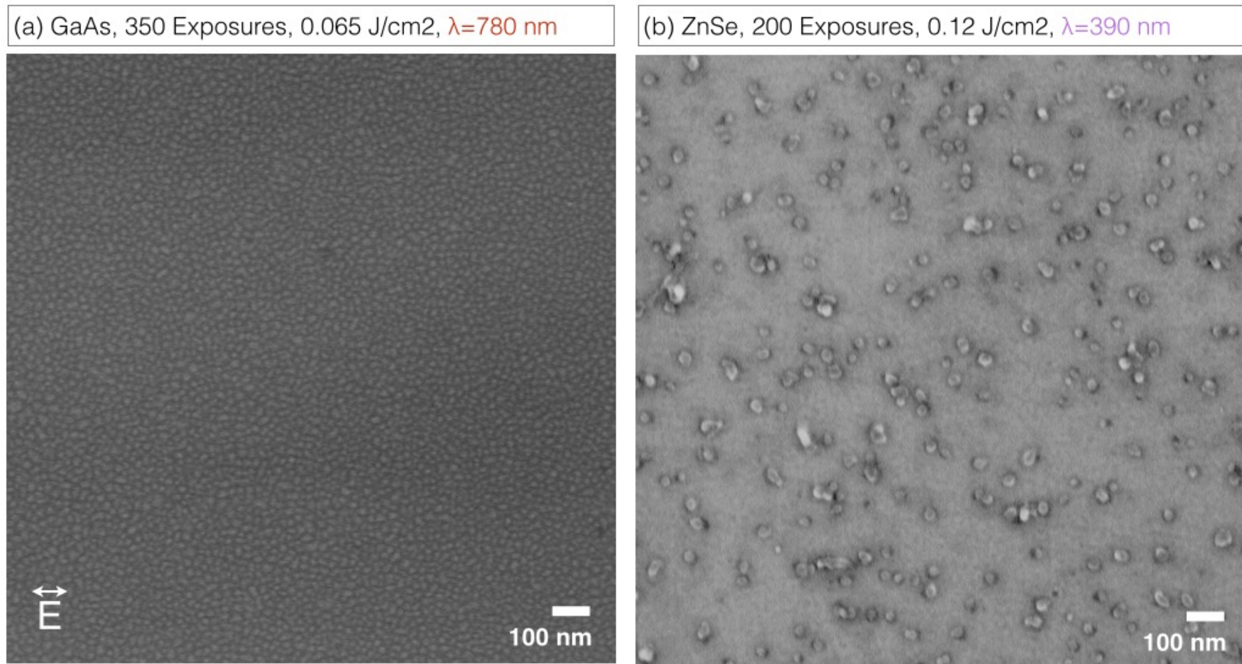

Figure 5.0.0 Initial islands/nanodots that evolve into HSFL with additional exposures in (a) GaAs and (b) ZnSe. Specific irradiation parameters that lead to HSFL in each material are given within the figure.

Section 4.1 Nanodot Formation in ZnSe

This study focuses on forming ZnSe nanostructures due to their optical properties [Geng, 2006; Hao, 2001] as well as the material's applications in heterojunction solar cells [Blieske, 1997; Yater, 1996; Chu, 1995]. Additionally, the femtosecond laser has been shown to nanostructure ZnSe within the damage crater [Jia, 2005]. Nanodot formation has been observed after nanosecond laser irradiation of amorphous films [Cen, 2006]. The mechanism responsible for this formation is laser heating inducing recrystallization in the amorphous film. The technique requires thermal annealing for particles to fully form. We demonstrate formation of ZnSe nanodots on the ZnSe surface after femtosecond laser irradiation. The nanocrystalline structures retain both stoichiometry and zinc-blende structure, characterized with cross-section nanobeam energy-dispersive X-ray spectroscopy (XEDS) and high resolution STEM. Unlike nanodots formed from nanosecond irradiation, femtosecond laser induced nanodots, far below the ultrafast melt threshold, do not form from lattice heating and recrystallization. Instead, the nanodots are consistent with morphological changes caused by ultrafast laser injected point defects and subsequent diffusion.

The irradiated samples were 1-3 μm thick epitaxial ZnSe films grown in MBE on GaAs (100) wafers. A Clark MXR Ti:sapphire 780 nm laser pulsed at 150 fs with a 1 kHz repetition rate and maximum pulse energy of 800 μJ was used. Laser was frequency doubled to 390 nm using a 0.4 mm thick beta-barium borate crystal cut at 29.2°. Experiments were conducted in air. Samples were irradiated with 10,000 exposures at a fixed location with peak fluence of 0.120 ± 0.035 J/cm^2. Reported error in peak fluence was determined by measuring the day to day variation in the minimum fluence required to produce a crater in GaAs after a single exposure

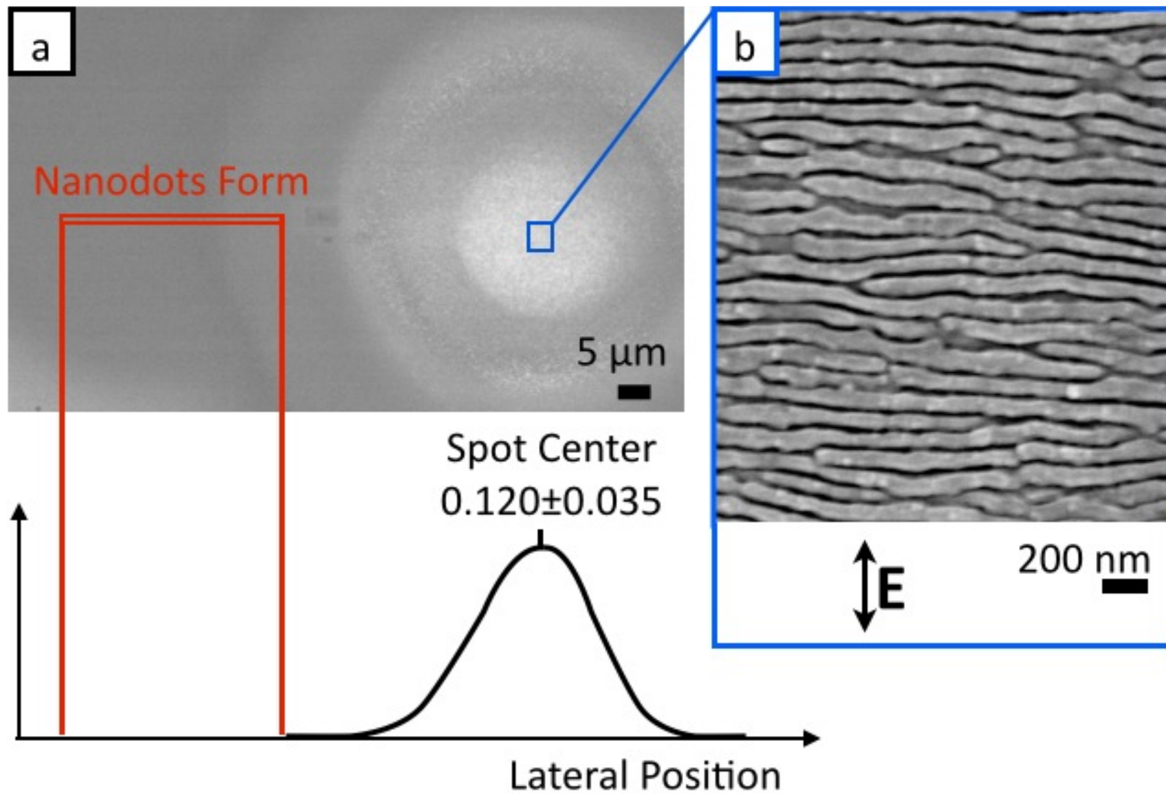

Figure 5.1.1 (a) SEM image of laser damage spot after 10,000 exposures at 0.120 ± 0.035 J/cm^2 and λ = 390 nm. The red box corresponds to a local flucence between 0.3 ± 0.3 x 10^{-3} J/cm^2 and 2.2 ± 0.8 x 10^{-2} J/cm^2 where nanodots are formed. The relationship between the lateral position along the horizontal axis of the damage spot and local fluence for the Gaussian pulse is plotted beneath the image. Local fluence for nanodot formation is calculated with a Gaussian fit to a beam profile imaged on a CCD camera. The region where nanodots form is outlined. (b) High spatial frequency laser induced periodic surface structures formed in ZnSe at the peak fluence. Structures have a period of 90 ± 10 nm. The structures are used as a fiducial mark to locate the spot center when calculating local fluence.

with 390 nm light. The GaAs material removal threshold of 0.155 ± 0.035 J/cm^2 was calculated with an established two-parameter fit [Borowiec, 2004].

The observed nanodots form in the tails of the Gaussian beam. Therefore, to calculate the nanodot formation fluence we use a Gaussian fit to a beam profile imaged with a DataRay WinCamD CCD camera. A schematic of the relationship between lateral position and local fluence is provided in FIG. 5.1.1(a) superimposed on a SEM image of a laser spot.

An SEM image of the morphology at the spot center shows the formation of laser induced periodic surface structures (LIPSS) in FIG. 5.1.1(b). The structures have a period of 90 ± 10 nm and align perpendicular to the applied electric field. These structures are commonly seen in compound semiconductors after multiple exposures [Jia, 2005; Borowiec, 2003]. The structures also serve as a fiducial mark to determine the spot center when calculating local fluence.

The relationship between local fluence and nanodot diameter was determined by measuring the size distribution at an offset from the spot center. The images in Figure 5.1.2 were taken 12 hours after irradiation. Reported local fluence error represents the sum of the propagated error in peak fluence measurement and the range of local fluence across the image width. Nanodot formation was not observed at fluences where LIPSS were present. A control study where the peak fluence was reduced to one error bar (0.035 J/cm^2) above zero showed that nanodots can form without the presence of LIPSS. Nanodots were observed at a maximum local fluence of $2.2 \pm 0.8 \times 10^{-2}$ J/cm^2 in Figure 5.1.2(h).

Nanodots are well dispersed but not in an ordered array. Diameter distributions were taken from SEM images and plotted at each local fluence. The magnified regions in Figure. 5.1.2 represent 9% of the total area counted. At least 200 nanodots were counted at each local fluence for all distributions. The relationship between nanodot diameter and local fluence is nearly linear up to $1.0 \pm 0.4 \times 10^{-2}$ J/cm^2 in Figure. 5.1.2(a-e). The trend-line in Figure. 5.1.2 is a least squares fit with a slope of 4.6 nm/10^{-3} J/cm^2. Nanodot diameter and density decreases above $1.0 \pm 0.4 \times 10^{-2}$ J/cm^2 in Figure 5.1.2(g-h) while pit density increases.The pits appear as dark secondary

electron contrast in Figure 5.1.2. The time dependent studies and further nanodot characterization discussed below are taken from the center of this linear regime. A local fluence of 4.0 ± 2.0 x 10^{-3} J/cm^2 is shown centered in Figure 5.1.2(d). Images in Figure 5.1.2(c) and (e) show nanodot morphology at a slight underestimate (2.0 ± 1.5 x 10^{-3} J/cm^2) and overestimate (6.0 ± 3.0 x 10^{-3} J/cm^2) respectively.

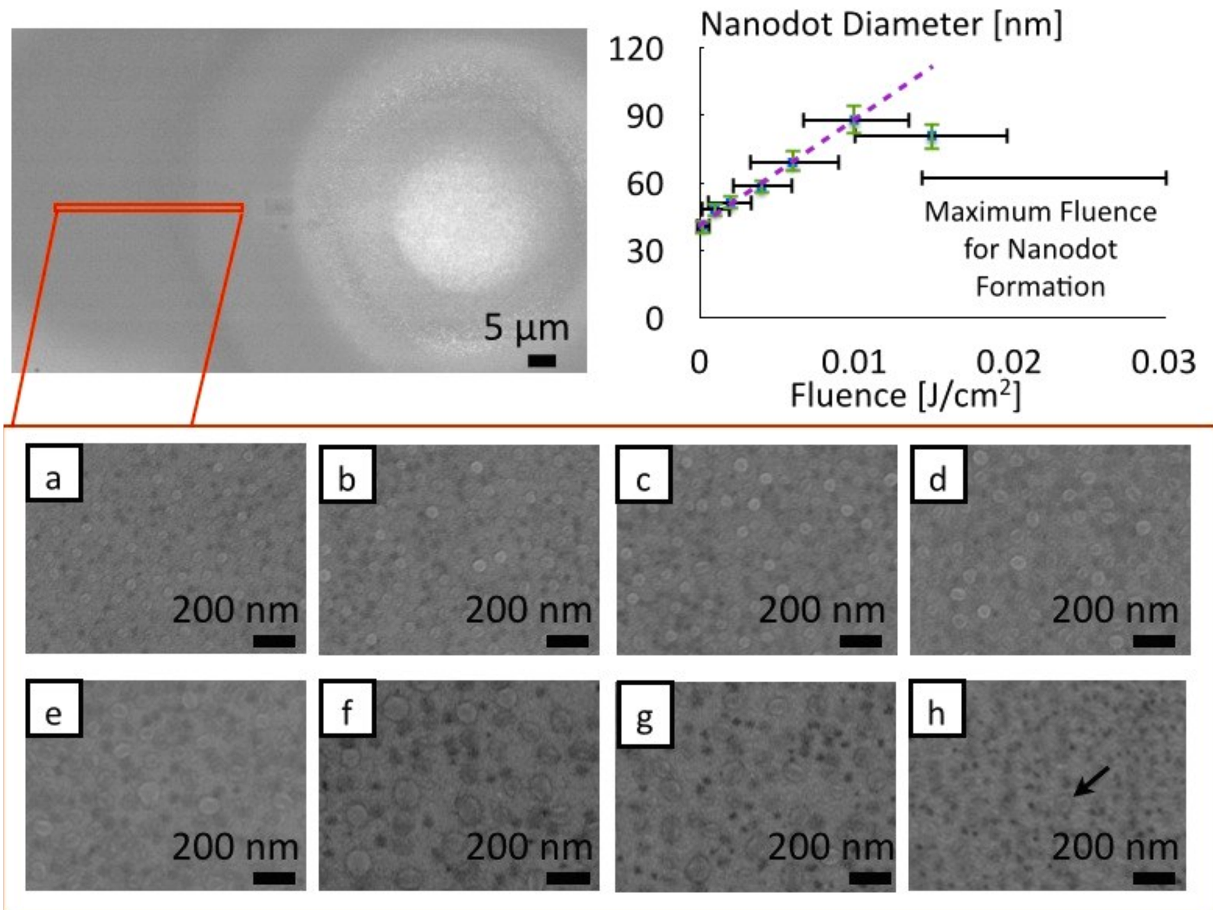

Figure. 5.1.2. Magnified images of nanodots at local fluences taken 12 hours after irradiation at (a) 0.3 ± 0.3 x 10^{-3} J/cm^2, (b) 1.2 ± 0.8 x 10^{-3} J/cm^2, (c) 2.0 ± 1.5 x 10^{-3} J/cm^2, (d) 4.0 ± 2.0 x 10^{-3} J/cm^2, (e) 6.0 ± 3.0 x 10^{-3} J/cm^2, (f) 1.0 ± 0.4 x 10^{-2} J/cm^2, (g) 1.5 ± 0.5 x 10^{-2} J/cm^2, and (h) 2.2 ± 0.8 x 10^{-2} J/cm^2. Nanodot formation has a maximum local fluence of 2.2 ± 0.8 x 10^{-2} J/cm^2. An arrow is provided in (h) to assist the reader in locating the nanodot. Nanodots are still visible at the minimum local fluence measurable by our technique at 0.3 ± 0.3 x 10^{-3} J/cm^2. The magnified images represent 9% of the area used when counting nanodots for the plotted diameter distribution. Error bars on the plot represent one standard deviation from the average nanodot diameter. At least 200 nanodots were counted at each local fluence. A least squares fit shows that nanodot average diameter increases linearly up to 1.0 ± 0.4 x 10^{-2} J/cm^2 at a rate of 4.6 nm/10^{-3} J/cm^2.

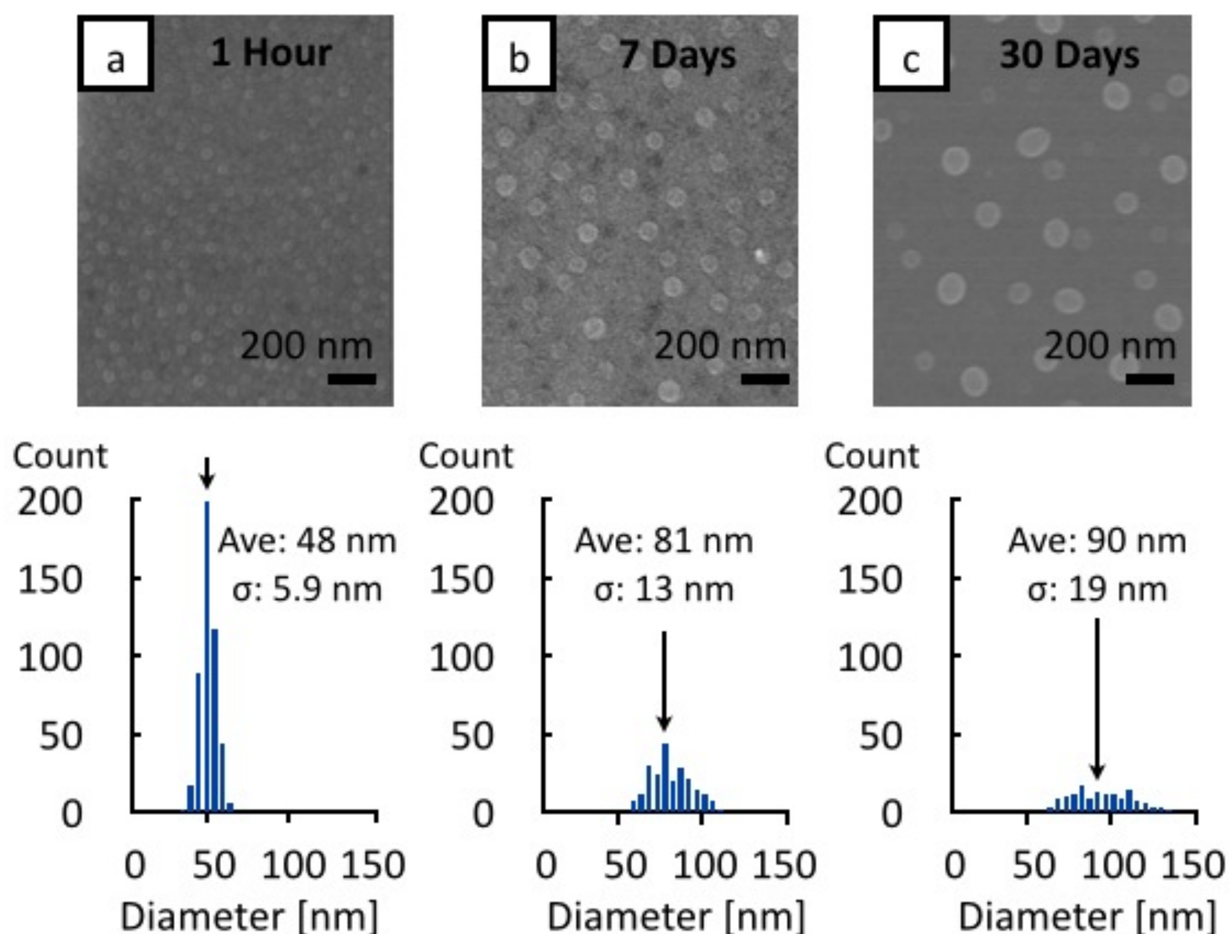

Figure 5.1.3. Representative SEM of counted region and corresponding nanodot diameter distributions at 4.0 ± 2.0 x 10^{-3} J/cm^2. after (a) 1 hour, (b) 7 days, and (c) 30 days. Nanodot distributions are normalized to the counted area. Initial nanodot density of 47 µm^{-2} decreases by a factor of two after 7 days and by a factor of 3 after 30 days. Nanodot average diameter and distribution width both increase over time, which is indicative of a coarsening process.

ZnSe nanodot diameter distribution changes over time in air at room temperature. The change in nanodot diameter over time after irradiation at 4 ± 2 x 10^{-3} J/cm^2 is depicted in Figure 5.1.3. The SEM images in Figure 5.1.3(a-c) were taken one hour, seven days, and 30 days after irradiation respectively. Histograms for each image are taken from a normalized surface area. Images are representative portions of the counted areas. Within the first twelve hours, nanodot average diameter increases from 48 in Figure 5.1.3(a) to 58 nm in Figure 5.1.2(e) and

distribution width increases from $\sigma = 5.9$ to 7.4 nm. Initial nanodot density (47 μm^{-2}) remains constant between one and twelve hours after irradiation but then decreases by a factor of two within seven days and by a factor of three within 30 days.

Nanodot volume change over time was calculated from AFM images. Nanodot volume per unit area was calculated using the Scanning Probe Image Processor™ software. Run-to-run variation between irradiations within the same film and is represented by an error of ± 0.3 $\mu m^3/\mu m^2$ in Figure 5.1.4. Nanodot volume one hour after irradiation is 2.6 ± 0.3 x 10^{-3} $\mu m^3/\mu m^2$ in Figure 5.1.4(a). Nanodot volume increased to 3.4 ± 0.3 x 10^{-3} $\mu m^3/\mu m^2$ in Figure 5.1.4(b) after 24 hours. After 140 hours, nanodot volume further increased to 4.4 ± 0.3 x 10^{-3} $\mu m^3/\mu m^2$ in Figure 5.1.4(c). Nanodot volume reaches a maximum after 6 days and remains within measurement error out to 30 days. Beyond 30 days, surface chemistry obscures our ability to measure additional changes to nanodot volume.

Nanodots on the ZnSe surface were characterized in cross-section STEM prepared with focused ion beam lift-out and imaged with a high angle annular dark field detector. Sample preparation takes more than one week, so nanodots are imaged after reaching equilibrium volume. Pt was deposited to protect the surface during lift-out. The micrograph in Figure 5.1.5(a) shows two nanodots in cross-section on the ZnSe film surface at a local fluence of 4 ± 2.0 x 10^{-3} J/cm^2. Nanodots have an aspect ratio greater than one. Two boxes in Figure 5.1.2a show the locations of magnified regions at the interface in Figure 5.1.5(c) and in the center of a particle in Figure 5.1.5(b). Particle chemical composition was determined with XEDS to contain both Zn and Se in Figure 5.1.5(d). The Cu signal is observed throughout the sample because the film is

attached to a Cu grid, which is sputtered onto the sample during ion beam polishing. Pt is present in the XEDS because the particle is dome shaped and nanodots are smaller than the STEM foil thickness.

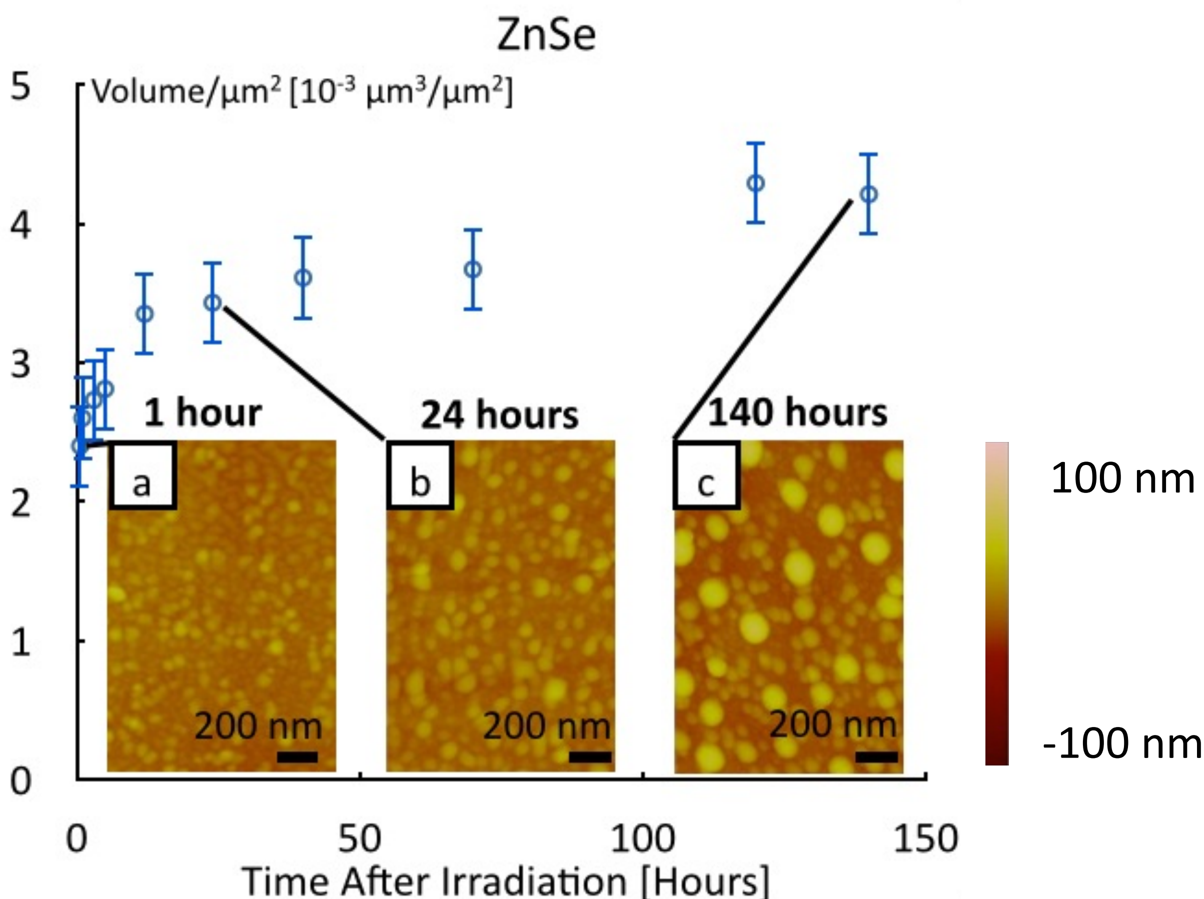

Figure 5.1.4. Relationship between nanodot volume per μm^2 and time after irradiation of 10,000 exposures at 4 ± 2 x 10^{-3} J/cm^2.. Nanodots have elliptical cross section with in-plane diameter greater than height. The volume calculation error (± 0.3 x 10^{-3} μm^3/μm^2) is consistent with the day to day variation. (a) AFM showing nanodot volume of 2.6 ± 0.3 x 10^{-3} μm^3/μm^2 one hour after irradiation. (b) A nanodot volume of 3.4 ± 0.3 x 10^{-3} μm^3/μm^2 24 hours after irradiation. (c) A nanodot volume of 4.4 ± 0.3 x 10^{-3} μm^3/μm^2 6 days after irradiation. Increasing nanodot volume over time is consistent with material diffusing from the bulk during growth. The continued volume expansion long after irradiation suggests that the mobile defects responsible for nanodot growth are the displaced atoms.

Images of the nanodots are taken with the ZnSe film aligned along the [110] zone axis. The film remains crystalline at the nanodot interface. The columns of atoms are visible within the film in Figure 5.1.5(c) and the interatomic spacing matches the labeled crystallographic directions for the ZnSe crystal structure. Within the nanodot, only planes of atoms are visible. Crystal directions in grains with small misorientation from the [110] zone axis of the film are labeled with arrows in Figure 5.1.5(b-c). Planes from grains with large misorientation angle from the film [110] zone axis are not visible because they do not meet the Bragg diffraction condition. The marked planes have spacing that match the ZnSe zinc-blende structure, but the planes do not align with the crystallographic directions of the film. It follows that nanodots are polycrystalline and have grain size on the order of 5 to 10 nm. The other nanodot in Figure 5.1.5(a) was nanocrystalline. No evidence of amorphous nanodots was observed throughout the STEM sample nor was there any amorphous material below or adjacent to the nanodots.

The ZnSe nanodots form due to a three step process. Point defects accumulate during laser irradiation. The interstitial atoms diffuse to the free surface and become adatoms. Adatom diffusion at room temperature is slow enough that growth takes on a Volmer-Weber mode resulting in the observed islands [Volmer, 1926]. The diffusion processes occur on a timescale long after irradiation has ceased so we assume that interactions between the laser and adatoms is negligible. While the band-gap collapse threshold has not been measured directly in ZnSe, we know that we are below the melt threshold. First, nanodots only form at lower fluences than where HSFL are observed. Second, it is well known that semiconductors typically have ultrafast melt thresholds that are approximately half the material removal threshold [Bonse, 2002;

Cavalleri, 1999]. Hence, we estimate the ZnSe melt threshold at approximately 0.3 J/cm^2 [Wang, 2005], about two orders of magnitude above nanodot formation.

The ultrafast laser generated nanodots from ZnSe retain both elements in Figure 5.1.5(d) and their zinc-blende crystal structure in Figure 5.1.5(b-c). The composition can be attributed to the unique ultrafast laser defect formation mechanism. In a perfect ZnSe crystal, both Zn and Se atoms have the same average thermal velocity and are connected by Zn-Se bonds. Our defect generation model depends primarily on an atom's initial thermal velocity and covalent bond strength and thus both species should have a similar probability of displacing from their lattice sites. The laser thus injects interstitials of both materials to serve as adatoms during the growth process.

The laser generated point defects strain the lattice and create a concentration gradient to drive diffusion within the system. Interstitial atoms that diffuse to the free surface cause morphological changes as positive relief features [Vancauwenbeghre, 1991]. The nanodot volume per μm^2 reaches an asymptote in Figure 5.1.4 as the bulk becomes depleted of interstitials to act as adatoms. The qualitative trend of increasing average nanodot diameter, increasing distribution width, and decreasing particle density over time in Figure 5.1.3 is indicative of nanodot coarsening. Nanodot coarsening continues after nanodot volume per μm^2 becomes constant and is driven by surface diffusion [Zhang, 1999; Smathers, 1998]. The coarsening causes the larger nanodots to grow at the expense of smaller nanodots, which leads to the non-uniform distribution observed on the surface in Figures 5.1.2 and 5.1.3.

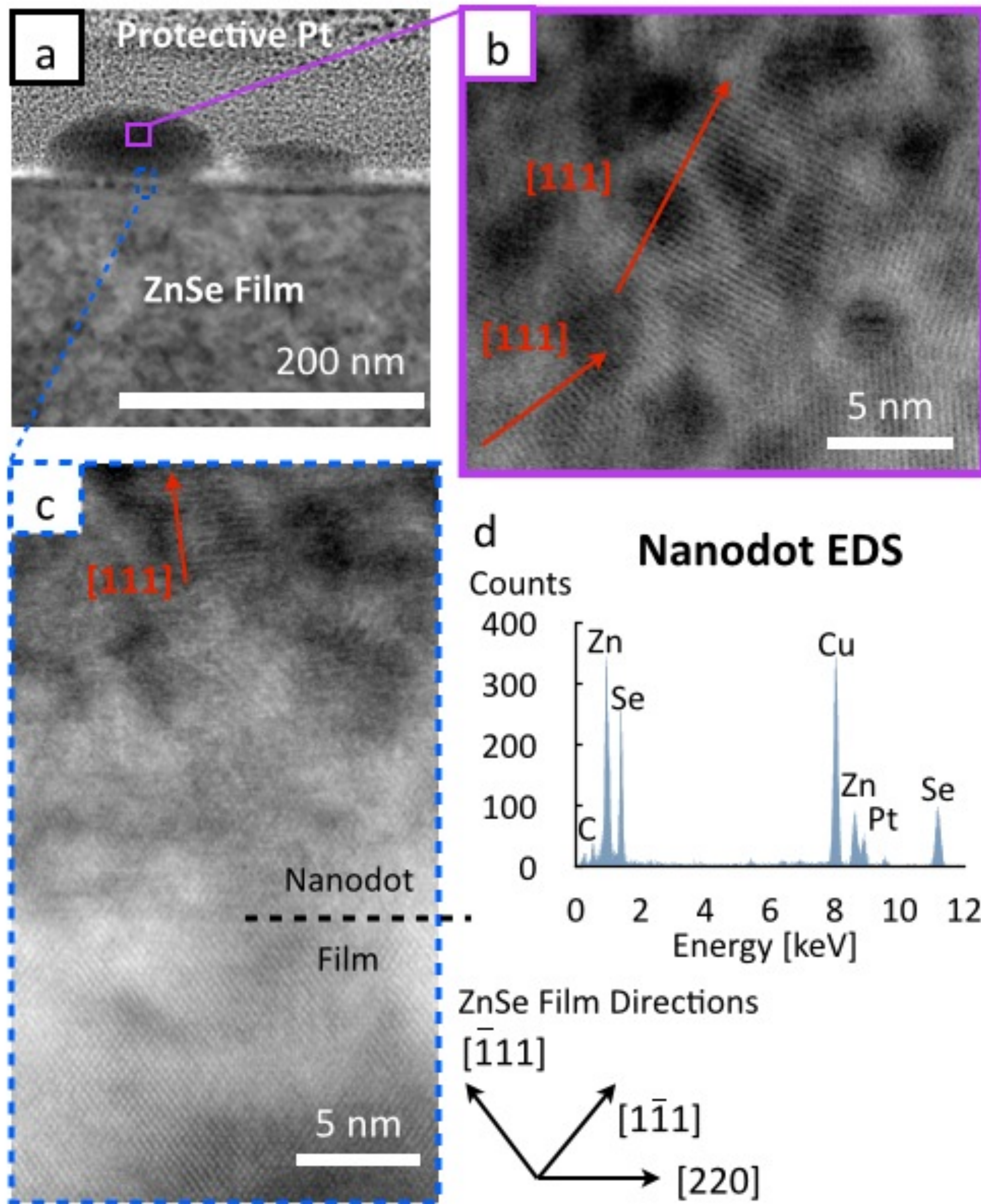

Figure 5.1.5 Cross-section STEM of two nanodots grown from 10,000 exposures at 4.0 ± 2.0 x 10^{-3} J/cm^2. The particles are imbedded in a Pt layer for protection during sample preparation. The rectangles point to the locations within the particle where the insets were taken. (b) Enlarged region of the center of the nanodot showing planes with spacings of ZnSe [111] and [220] directions. (c) Enlarged region at the film/nanodot interface. The film is aligned along the [110] zone axis and retains its structure after irradiation. Planes with ZnSe [111] spacings that are not aligned with the directions in the film are visible within the nanodot. We determine that the nanodots are polycrystalline ZnSe that form while the underlying film remains a single crystal (d) XEDS from within the particle. The Cu comes from sputtering of the grid onto the sample during ion beam polishing. The Pt comes from the protective layer. The nanodots are chemically composed of primarily Zn and Se.

Polycrystalline nanodots are consistent with hillock formation on semiconductors having high point defect concentrations. Polycrystalline structures are also commonly observed on film surfaces during molecular beam homoepitaxy of compound semiconductors at low temperature [Lilental-Weber, 1991]. Films grow with high enough vacancy concentrations that the lattice cannot incorporate the excess anions, which condense on the surface. Kinetic Monte-Carlo simulations predict Ehrlich-Schwoebel step edge diffusion barriers cause adatoms to mound and eventually become the observed polycrystalline structures [Apostolopoulos, 2002]. We predict that laser generated interstitials both form mounds and become polycrystalline due to these same surface kinetics. The key difference between femtosecond laser induced nanodots and those grown in MBE is that the laser induced adatom source is the interstitial defects that have diffused and recombined with the free surface. The larger nanodots formed at constant time after irradiation and higher local fluence (up to 0.01 J/cm^2) can be qualitatively interpreted as more energy producing larger defect populations and faster diffusion in Figure 5.1.2. Above 0.01 J/cm^2 sufficient adatoms are generated to begin to form a continuous film. However, pits on the surface become more prominent in Figure 5.1.s. 2(g-h), which is consistent with islands combining with increased adatom concentration during Volmer-Weber growth [Kaganer, 2009].

We have also considered shot to shot heat accumulation. The rise in temperature after a single exposure was calculated with the energy balance in Equation 1. Within Equation 1, ΔT is the lattice temperature rise of ~50 K after an exposure at local fluence, F, of 4 x 10^{-3} J/cm^2 with reflectivity, R, of 0.17 [Walter, 1970] and heated depth, L, on the order of the laser absorption

depth of 100 nm [Adachi, 1991] is consistent with temperature rises calculated from reflectivity measurements from similar fluences [Wu, 2007] Heat capacity at constant volume, c_v (0.95 J/K^1cm^3) [Benkabou, 2000], is used since energy transfer to the lattice occurs on a timescale faster than thermal expansion. The temperature change is used in the mass transport formula in Equation 2 to calculate an quench rate of 10^{11} K/s. Within the mass transport equation, k (0.2 W/cm^1K^1) [Lugueva, 2004] is a thermal conductivity, c_p (1.8 J/K^1cm^3) [Berger, 1993] is the heat capacity at constant pressure, and ρ (5.27 g/cm^3) is the ZnSe density. The calculated rate is fast enough for the lattice to return to room temperature within 100 ps. At nanodot formation fluences two orders of magnitude below the band-gap collapse threshold, the material would still return to room temperature within 10 μs with a quench rate as slow as 10^6 K/s. Thus, morphological changes during nanodot formation occur from solid-state damage accumulation within the film.

To conclude, we observed the formation of polycrystalline ZnSe nanodots on the film surface after ultrafast laser irradiation. We established a range of fluences over which nanodots form. Our structural characterization of the underlying film allows us to infer that nanodot formation is a solid state process. Nanodot formation is consistent with a defect accumulation and diffusion model, similar to that responsible for HSFL formation. The observed nanodot coarsening and chemical composition are consistent with our model. Beyond fundamental understanding of laser-materials interaction, the ability to form semiconductor nanodots on an epitaxial film in air and at room temperature may provide a useful technique for emerging nanotechnologies.

Section 4.2 Nanodot Formation in GaAs

Nanodot formation was performed on as-received GaAs wafers in order to show that the structures were characteristic of semiconductors. An SEM image of nanodots formed after 10,000 exposures at λ=390 nm and 4.0 ± 2.0 x 10^{-3} J/cm^2 is shown in Figure 5.2.1 taken two hours after irradiation. The nanodots have a diameter of 36 ± 6 nm after two hours. Similar to the ZnSe nanodots, the islands coarsen to a distribution of 39 ± 8 nm after 27 hours. Although nanodots were observed in both materials at λ=390 nm, those on ZnSe had rounded edges while those on GaAs appear faceted in FIG 5.2.1 unlike typical rounded Ga droplets seen in MBE [Plissard, 2011] and ion-beam deposition [Prestigiacomo, 2005]. While Ga is known to segregate when forming droplets on the GaAs surface, the facets on the nanodots leave open the possibility that the nanodots contain crystalline GaAs. These Ga droplets form due to Langmuir evaporation when the growth temperature exceeds a congruent evaporation temperature [Goldstein,1976]. For the [100] face in GaAs, this temperature is 663°C. At nanodot formation fluences, the maximum temperature is ~ 0.25 of the congruent evaporation temperature in GaAs so it would not drive Ga droplet formation. For either composition, this result shows that a nanodot morphology generated by the ultrafast laser is not unique to ZnSe and that nanodot formation does not require the ZnSe/GaAs interface or a film under tension.

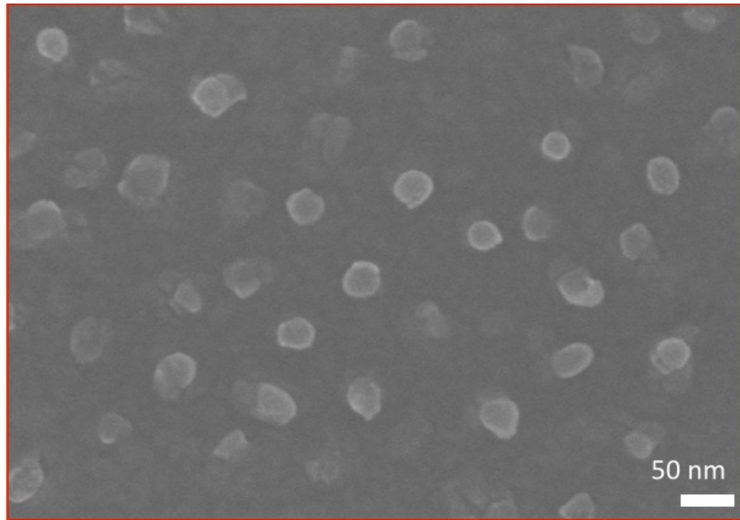

Figure **5.2.1** SEM image of nanodots on GaAs formed after 10,000 exposures at λ=390 nm and 4 x 10^{-3} J/cm^2 taken two hours after irradiation. Nanodots appear faceted. Nanodots have an diameter distribution of 36 ± 6 nm.

The as-received wafers contain carbon impurities that serve to increase the intrinsic nature of the GaAs for electrical applications. A second control experiment on 500 nm thick, stress-free, dislocation-free GaAs epilayer produced the same nanostructures observed on the as-received wafers. This null result shows that the carbon impurity atoms are not responsible for HSFL and nanodot formation [Kang, 2013].

An AFM image of the GaAs nanodots an hour after irradiation with 10,000 exposures at a local fluence of 4.0 ± 2.0 x 10^{-3} J/cm^2 and λ=390 nm is provided in FIG. 5.2.2(a). Nanodot volume per μm^2 under these conditions is equivalent for both materials. Unlike the ZnSe nanodots, the structures in GaAs do not increase in volume after the first hour. Coarsening from surface diffusion is still observed in FIG 5.2.2(b).

The difference in growth long after irradiation suggests that the GaAs atoms require the enhanced mobility during band-gap collapse in order to favor nanostructure formation over defect annihilation. Interstitials being more stable in ZnSe is consistent with its higher difference in electronegativity between cations and anions.

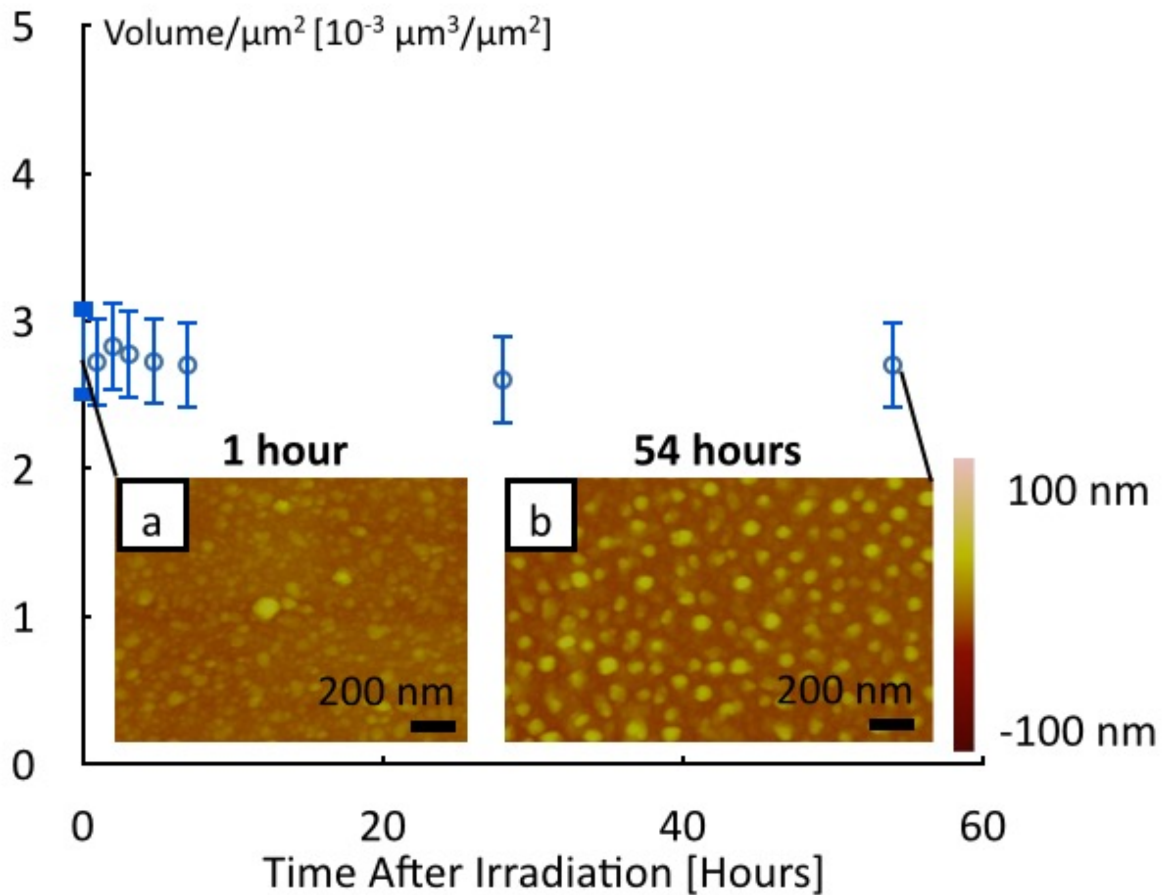

Figure 5.2.2 AFM images of of nanodots on GaAs from 10,000 exposures, λ=390 nm, at 4.0 ± 2.0 J/cm2 (a) 1 hour and (b) 54 hours after irradiation. While the nanodots still coarsen via surface diffusion, no bulk diffusion increases their volume after their initial formation.

A simple thermodynamic argument can explain the preference for nanodots to form over pits at low dose. We consider a 2D lattice occupied by alternating cation and anion species. The system is treated as a regular mixture of vacancies, interstitials, and lattice atoms. The partition function for such a mixture is described by Equation 5.2.1:

$$\Omega=\Omega_V\cdot\Omega_I=(N_A!\cdot N_A!)/((N_A-N_V)!\cdot N_V!\cdot(N_A-N_I)!\cdot N_I!)$$

Equation (5.2.1)

Where Ω is a partition function, N_A is the number of atoms in the system, N_I is the number of interstitial atoms, and N_V is the number of vacancy atoms. Because the ultrafast laser generated point defects are Frenkel Pairs, $N_I = N_V$. From the partition function we derive an expression for the configurational entropy ΔS in Equation 5.2.2:

$$\Delta S = k_b\cdot \ln\Omega=2k_b\{N_A\cdot \ln[N_A/(N_A-N_V)]+N_V\cdot \ln[(N_A-N_V)/N_V]\}$$

(Equation 5.2.2)

The configurational entropy is used in the regular solution approximation for the Gibbs free energy ΔG in Equation 5.2.4:

$$\Delta G = \Delta H - T\cdot\Delta S$$

(Equation 5.2.3)

$$\Delta G = K \cdot X_{defect} \cdot (1-X_{defect}) - T\cdot\Delta S$$

(Equation 5.2.4)

Where K is the defect heat of formation, X_{defect} is the number fraction of point defects, and T is the temperature in Kelvin.

The formation energies for vacancies [Van Vechten, 1975] is lower than that of interstitials [Hurle, 1979] in zinc blende semiconductors. The less stable self-interstitials therefore put more strain on the lattice, leading to higher mobility causing nanodots to form more readily than pits. Equation 3 predicts that self-interstitials of either ion are completely unstable at room temperature in GaAs [Hurle, 1979]. Meanwhile the vacancy solubility within the lattice is ~0.7%. The conditions for nanodot formation can thus be reframed as the point where the population inversion of Frenkel Pairs does not exceed the lattice's solubility for vacancies.

Island-like structures also form after irradiation with λ=780 nm. SEM images of the 20 nm islands formed after 350 exposures at 0.065 ± 0.005 J/cm^2 are shown in Figures 5.0.1(a). Continued irradiation of these nanodots leads to HSFL formation. The role of surface plasmon polaritons responsible for the continued nanostructure evolution will be discussed in Chapter 6. The absence of HSFL formation from a single from the nanodots formed at λ=390 nm will be discussed in Chapter 7.

To summarize, nanodot formation, via diffusing defects, is universal to semiconductors. The tendency for island formation over pit formation at low dose occurs due to the difference in solubilities within the lattice between the two species. Additionally, nanodot formation is greatly assisted by enhanced diffusivity during band-gap collapse and the structures would not otherwise form without this enhancement in GaAs.

Section 4.3 Comparison of point defect based islands and ablation based nanoparticles

Scalable nanomanufacturing is often dependent upon the development of techniques to form and deposit nanoparticles onto a substrate at rates applicable to manufacturing techniques such as roll-to-roll processing [Wei, 2008]. Techniques for patterning a substrate with nanoparticles such as lithography [Huang, 2002; Franklin, 2001], stamping solutions of nanoparticles [Kind, 2000], and ink-jet printing [Ago, 2003] often lead to well dispersed nanoparticles. However, these methods are either time consuming or require a two-step process of forming and then dispersing particles.

Laser based techniques offer a one-pot, scaleable means for nanoparticle deposition. Pulsed laser deposition (PLD) is the most common laser based method of depositing nanoparticles. The resulting nanoparticle morphology is dependent on the properties of the plasma plume resulting from bulk ablation [Anisomov, 1993; Haverkamp, 2003]. Laser printing techniques involve irradiation of thin films through a transparent substrate and can be performed with either the nanosecond [Murray, 2008; Amoruso, 2011] or ultrafast laser [Murphy, 2013a; Rouleau, 2014]. Compared to bulk ablation in PLD, nanoparticles printed from thin films with nanosecond lasers have a more narrow size distribution but the same average particle size [Amoruso, 2011]. Ultrafast laser printed nanoparticles exhibit narrow size distributions and average particle size is dependent on the irradiation conditions [Murphy, 2013a]. Further, Ultrafast laser nanoparticle printing can be performed at fluences below the damage threshold for common semiconductor substrates [Bonse, 2002]. These fluences are a factor of four lower than those required for NiO nanoparticle generation from ultrafast laser based PLD [Liu, 2007].

Scalable processes for deposition, size, and shape control of nanoparticles have far reaching applications in numerous fields. Nanoparticle size and shape determine properties ranging from its plasmon response [Lee, 2006] to its uptake into cells for biological applications [Albanese, 2012]. Here we focus on NiO nanoparticles, which are specifically useful as a catalyst for Carbon nanotube [Kukovitsky, 2002] and GaN nanowire growth [Kim, 2008]. Control over catalyst particle size offers a means for control of the resulting structures' diameters [Nasibulin, 2005; Kukovitsky, 2002; Cui, 2001]. NiO core/shell nanoparticles have also recently shown promise as an anode material in Li-ion batteries [Sasidharan, 2014].

Ultrafast laser nanoparticle printing is a novel one-step process for depositing nanoparticles onto a substrate of choice [Murphy, 2013a; Rouleau, 2014]. The technique is a variant of the LIFT technique [Bohandy 1988] that involves irradiating thin films on transparent substrates through the glass side first. The sample is translated such that each pulse irradiates a virgin area of the sample. The film melts and is ejected from the glass substrate within the irradiated region. The ejected film breaks up into nanoparticles that are collected on the material surface of choice [Murphy, 2013a]. In this chapter, we will detail how size control of these LIFT based nanoparticles are fundamentally different from the defect-diffusion based nanodots in semiconductors. While nanodot size was determined by a coarsening, the NiO nanoparticle size depends on activating different thin film removal mechanisms during ablation. Nanoparticle shape control can also be achieved by tuning resolidification dynamics.

Ultrafast nanoparticle printing has typically been performed above the metal film's plasma threshold [Murphy, 2013a, Rousseau, 2014]. Patterning of 20nm thick Ni films at 5 J/cm^2 with TEM grids placed 8 mm from the film resulted in printing of clusters of nanoparticles onto

TEM grids, shown in Figure 5.3.1(a). Most printed nanoparticles have symmetric, equilibrium shapes. The nanoparticles with diameters >20 nm were typically spherical, indicated by the solid arrow in Figure 5.3.1(a), and STEM contrast suggests spherical NPs are composed of a Ni core surrounded by an 10 nm thick oxide shell. The smaller (<20 nm) nanoparticles were faceted with square and hexagonal shapes, indicated by the dashed arrows in Figure 5.3.1(b).

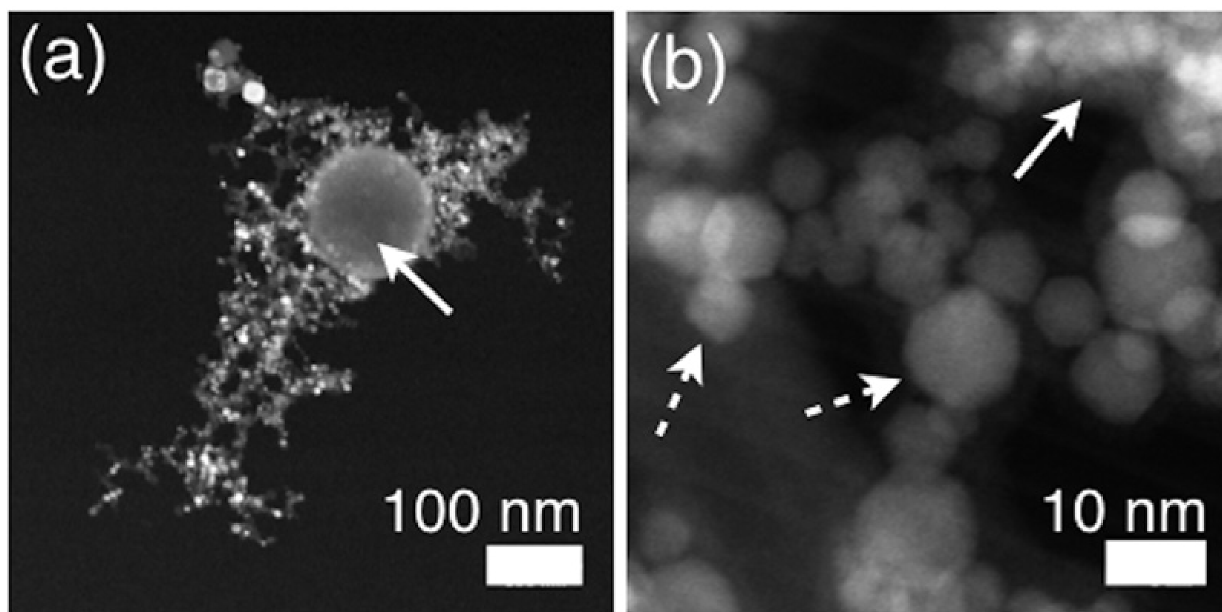

Figure 5.3.1 from from R.D. Murphy, M.J. Abere, K.J. Schrider, B. Torralva, and S.M. Yalisove, Appl. Phys. Lett. 103, 093113 (2013). STEM images of NPs printed onto a holey carbon TEM grid from a 20 nm Ni film using a 5 J/cm^2 laser fluence. (a) NPs were usually found in clusters. NPs with diameters >20 nm were typically spherical and STEM contrast suggests they are composed of a Ni core surrounded by an 10 nm thick oxide shell. A spherical NP with a diameter of 145 nm is indicated by the solid arrow. (b) A cluster of NPs suspended over a TEM grid hole. NPs with diameters 20 nm were typically faceted with square and hexagonal shapes, indicated by the dashed arrows. The solid arrow indicates a dense group of NPs with diameters <6 nm.

The printed nanoparticles were characterized both structurally and chemically in STEM. Particles with a square projection are characterized as the 100 face of cubic NiO with nanobeam diffraction in Figure 5.3.2(a). Particles with a hexagonal projection are characterized as the (110)

face of cubic NiO in Figure 5.3.2(c). Atomic resolution images show that the square Figure 5.3.2(a) and hexagonal Figure 5.3.2B nanoparticles are single crystals. Measuring the interatomic spacing of the images is consistent with the plane spacings determined in nanodiffraction. Individual particles are determined to be 50/50 Ni and O using nanobeam EELS in Figure 5.3.2(b).

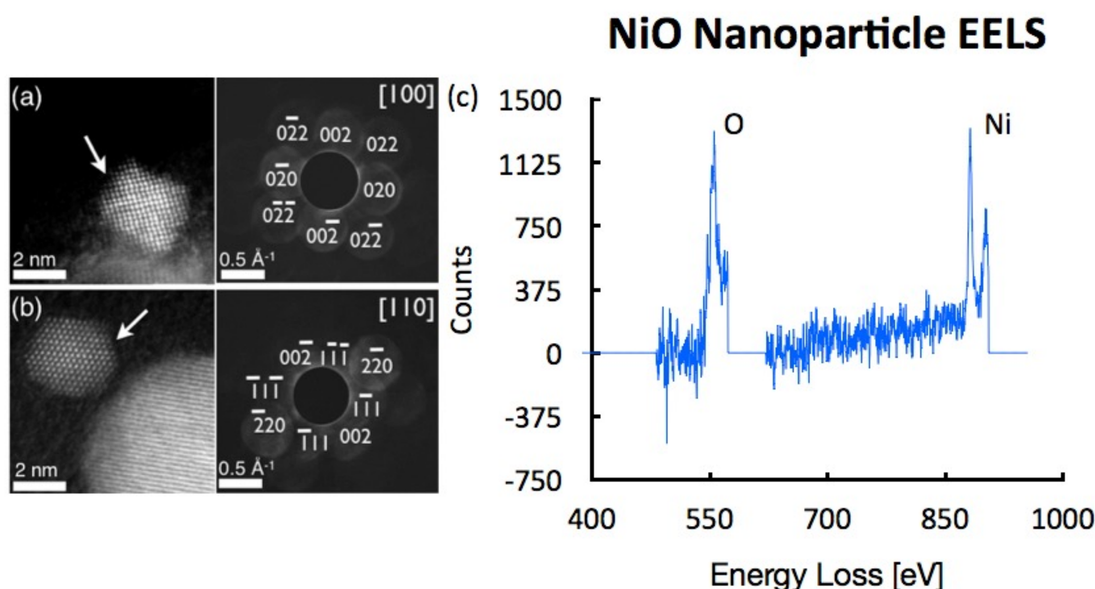

Figure 5.3.2 Adapted from R.D. Murphy, M.J. Abere, K.J. Schrider, B. Torralva, and S.M. Yalisove, Appl. Phys. Lett. **103**, 093113 (2013). a and b) STEM image of Single crystal NiO nanoparticles (see arrows) printed onto holey carbon TEM grids from 20 nm films. a) square and b) hexagonal projections are observed and nanodiffraction shows that they are both FCC NiO aligned down the [100] (square) and [110] (hexagonal) zone axis. c) Corresponding nanobeam EELS from a single nanoparticle confirming a 1:1 ratio of Ni to O in nanoparticles. Misaligned atoms in (a) are due to sample drift in the STEM.

In previous work [Murphy, 2013], many of the nanoparticles with diameters <6 nm were clustered in a way that they could not be accurately counted. By improving the STEM quality such that individual nanoparticles within the clusters could be differentiated by the coherence of

their lattice planes, it became apparent that the nanoparticles under 20 nm in diameter were actually composed of two modes. Furthermore, we observed that the presence of these two modes correlates to both the thickness and post mortem morphology of the film used for printing.

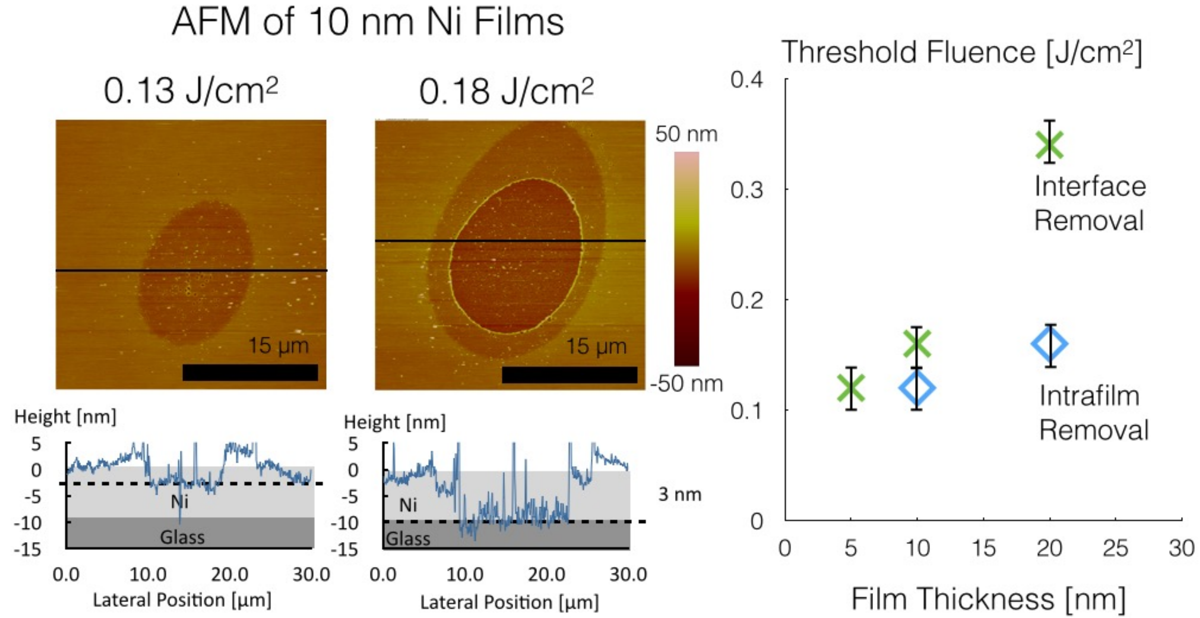

Figure 5.3.3 (a) AFM of the 3 nm intrafilm separation from a 10 nm film after a single exposure at 0.13 J/cm^2 from he Ni side first. (b) AFM of the 7 nm layer removed in addition to the 3 nm at 0.18 J/cm^2 when both intrafilm and interface removal are present. (c) Threshold fluences for Ni side first irradiation of 20, 10, and 5 nm films. The thresholds for the two types of removal become closer in value as film thickness decreases such that for the 5 nm film, only separation at the interface was observed.

It is well known that irradiation of metal thin films with a single exposure produces two distinct damage morphologies [Murphy, 2013b; Rouleau, 2014]. Material removal can either occur within the film as shown in Figure 5.3.3(a) or at the glass/Ni interface as shown in Figure 5.3.3(b). We refer to these two types of removal as being either “intrafilm" or “interface” respectively. The depth of intrafilm removal is dependent on the film thickness. While it has been previously shown that 7 nm of Ni are removed from 20 nm films [Schrider, submitted], we now

show that 3 nm of material are ejected from 10 nm thick films. Only removal at the Ni/glass interface was observed when the film thickness was reduced to 5 nm. Decreasing film thickness also decreases the threshold fluence for each type of removal. For Ni side first irradiation, the interface removal threshold falls from 0.34 J/cm^2 to 0.16 J/cm^2 to 0.12 J/cm^2 for 20 nm, 10 nm, and 5 nm films respectively. Meanwhile, the intrafilm removal threshold changes from 0.16 J/cm^2 to 0.12 J/cm^2 for 20 nm and 10 nm films respectively. Both of these values are less than the 0.25 J/cm^2 threshold for bulk Ni [Murphy, 2013c]. The material removal thresholds as a function of film thickness are provided in Figure 5.3.3(c)

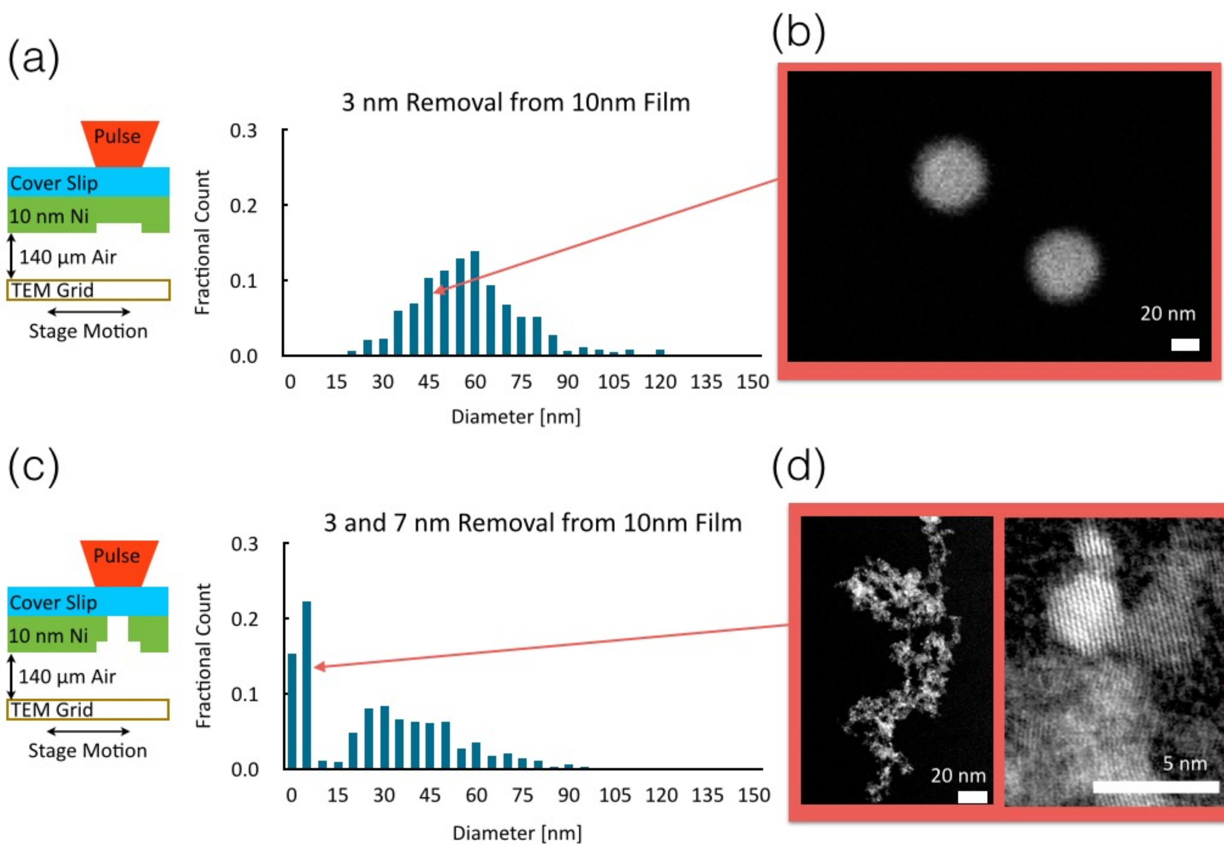

Figure 5.3.4 (a) Schematic and histogram of the nanoparticle distribution formed after printing from the 3 nm intrafilm layer for 10 nm Ni films at 0.09 J/cm^2. Nanoparticles have an average diameter of 58 ± 18 nm. (b) Dark field STEM image of the spherical nanoparticles produced under the 3 nm slab. (c) Schematic and histogram of the nanoparticle distribution formed after printing from both the 3 nm and 7 nm layers for 10 nm Ni films at 0.024 J/cm^2. The addition of a 3 ± 1 nm population originates from the 7 nm layer (b) Dark field STEM image of the agglomerated square and hexagonal nanoparticles produced from the 7 nm slab.

The damage thresholds are reported as the incident fluence. Due to multiple reflections within the glass, a larger fraction of the laser energy is absorbed by irradiating with the glass side as opposed to the Ni side first [Murphy, 2013c]. The damage thresholds are less than those reported for previous Ni side first thresholds [Murphy, 2013b; Schrider, submitted] and scale with the difference in absorptance between the two irradiation geometries [Murphy, 2013c]. The glass first thresholds for interface removal were 0.21 J/cm^2, 0.12 J/cm^2, and 0.08 J/cm^2 for 20 nm, 10 nm, and 5 nm films respectively. The thresholds for intrafilm removal were 0.11 J/cm^2 and 0.06 J/cm^2 for 20 nm and 10 nm films respectively. Irradiation from the glass side first did not change the depth of material expelled during intrafilm removal for any film thickness.

The nanoparticles formed after intrafilm removal at 0.09 J/cm^2 from 10 nm thick films have diameters of 58 ± 18 nm. The nanoparticles were dispersed randomly throughout the TEM grid. A particle diameter distribution taken from 533 nanoparticles is provided in Figure 5.3.4(a) along with dark field STEM images showing their typical spherical shape in Figure 5.3.4(b). The STEM contrast in Figure 5.3.4(b) indicates that these nanoparticles are NiO and not the core/shell structures that formed above the plasma threshold. Increasing the fluence above the interface removal threshold to 0.24 J/cm^2 causes a reduction in the large dispersed nanoparticle diameter to 43 ± 18 nm while preserving the width of the distribution. Additionally, nanoparticle agglomerates with 3 nm diameter form at this fluence. The relative frequency of these two populations in terms of the number of particles is shown in the diameter distribution in Figure 5.3.4(c). The distribution was generated by counting 1,354 individual particles. Typical dark field STEM images of these agglomerates are shown in Figure 5.3.4(d). The single crystal particles

have circular, square, or hexagonal projections and can be differentiated within the agglomerates by the coherence of their lattice planes.

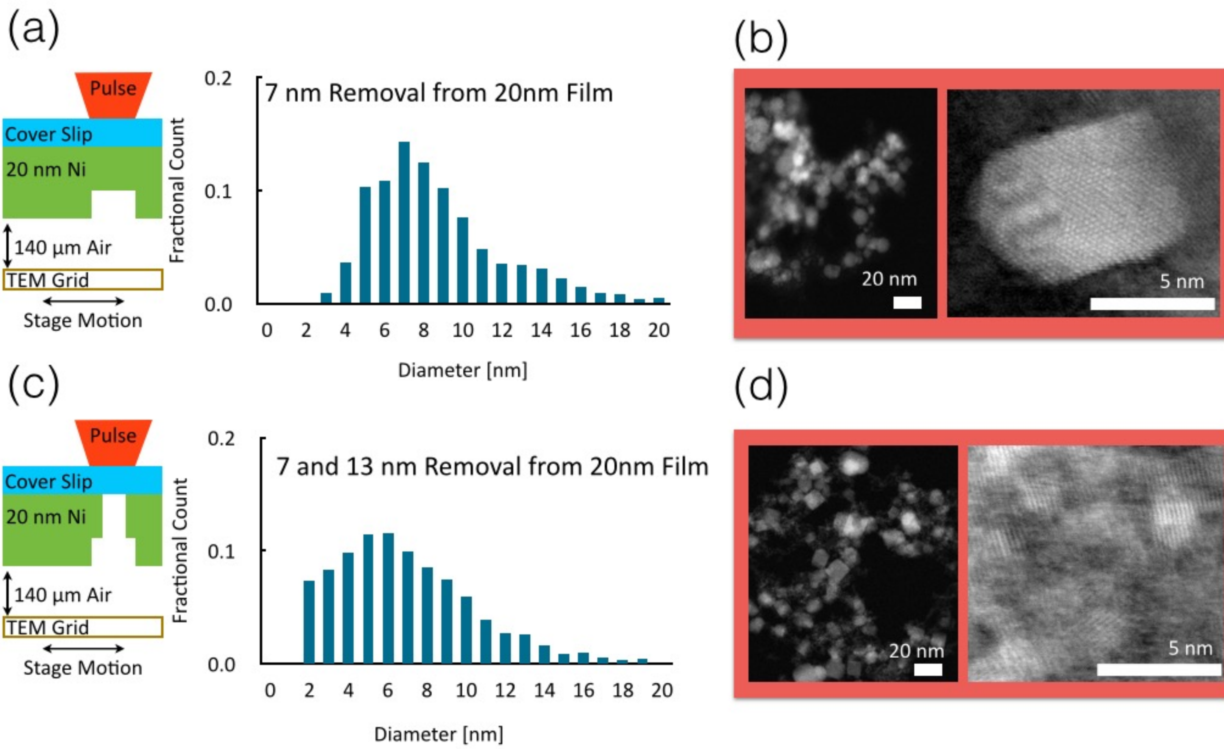

Figure 5.3.5 (a) Schematic and histogram of the nanoparticle distribution formed after printing from the 3 nm intrafilm layer for 10 nm Ni films at 0.15 J/cm^2. Nanoparticles have an average diameter of 7 ± 3 nm. (b) Dark field STEM image of the spherical nanoparticles produced under the 7 nm slab. (c) Schematic and histogram of the nanoparticle distribution formed after printing from both the 3 nm and 7 nm layers for 10 nm Ni films at 0.024 J/cm^2. The broader peak occurs because both the 3 and 7 nm populations from from the 13 nm and 7 nm slabs respectively (b) Dark field STEM image of the agglomerated nanoparticles produced from the 13 nm slab.

Intrafilm and interface removal also produce different sized nanoparticles from 20 nm films. The removal of 7 nm during intrafilm separation at 0.15 J/cm^2 produces nanoparticles with an average diameter equal to the removed film's thickness (diameter = 7 ± 3 nm). A diameter distribution of these nanoparticles was taken from 1,639 particles and is shown in Figure 5.3.5(a). Sample STEM images of the nanoparticles and an atomic resolution dark field image of a single particle are shown in Figure 5.3.5(b). The much larger (>20 nm) nanoparticles can still form but make up far less than 1% of all deposited nanoparticles. The 7 nm population is still present when both intrafilm and interface removal are active from irradiation at 0.24 J/cm^2, but with the addition of the 3 nm agglomerates of nanoparticles, much like those previously observed from the 10 nm films. The distribution, taken from 1,954 particles and shown in Figure 5.3.5(c), appears as a single broad peak because the tails of the 3 and 7 nm populations overlap. However, the STEM images in Figure 5.3.5(d) show that the nanoparticles distribute as larger particles with agglomerates of the smaller population such that areas that appear as uniform dark field contrast in the left hand image are actually composed of numerous agglomerated particles in the right hand image.

The 7 nm nanoparticles from intrafilm removal of 20 nm films is decidedly smaller than the 40-60 nm population from the 3 nm intrafilm removal from 10 nm films. The 5 nm removal from 5 nm thick films produces nanoparticles with an average diameter of 24 ± 11 nm as shown in the distribution in Figure 5.3.6(b). The nanoparticle diameter is consistent with the trend that the larger population's diameter is inversely proportional to the thickness of the removed film. However, the 24 nm nanoparticles form under irradiation conditions where the film is removed at the Ni/glass interface. Nanoparticles with diameters on the order of 20 nm are also observed after

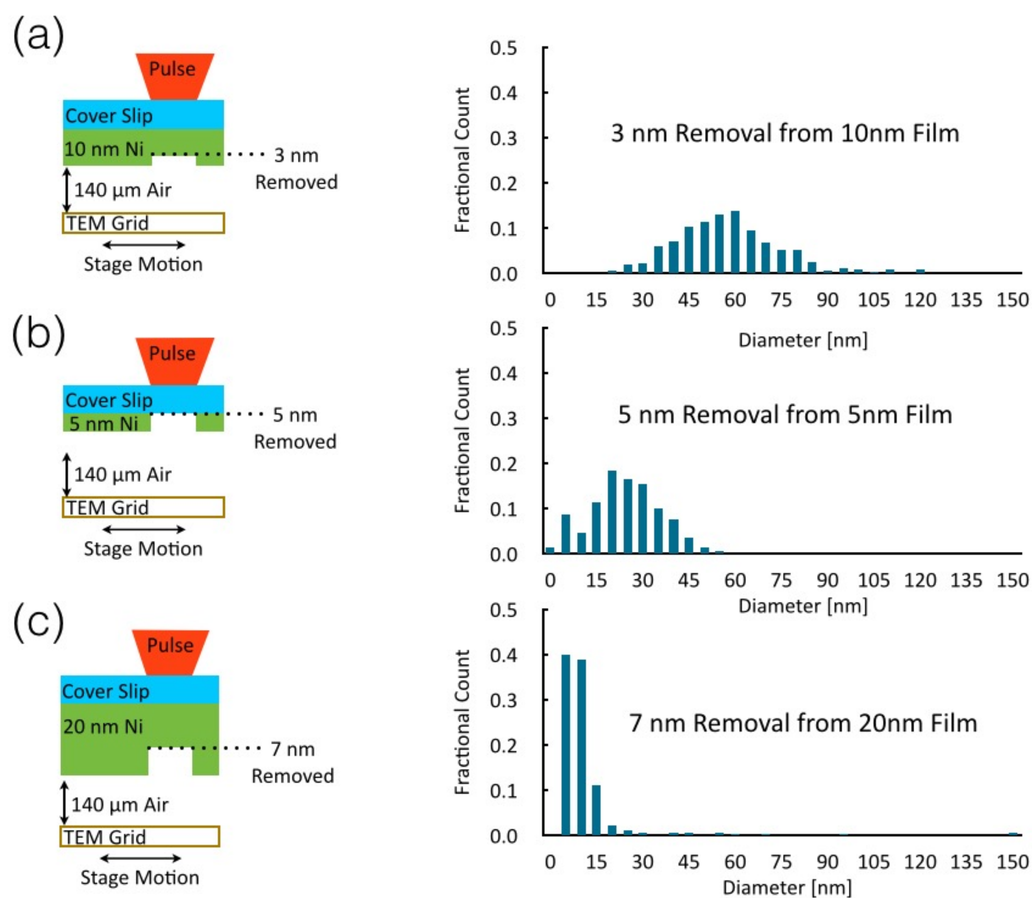

Figure 5.3.6 Removal of (a) 3, (b), 5, and (c) 7 nm slabs from 10 nm, 5 nm, and 20 nm Ni films respectively. Decreasing slab thickness leads to larger nanoparticles. It should be noted that the 5 nm slab separates into nanoparticles in a way consistent with removal via liquid spallation. This is in contrast to those nanoparticles formed during the nucleation and growth of voids within the vapor dome, which form the 3 nm agglomerates regardless of the removed thickness.

printing from 2 nm thick Pt films [Rouleau, 2014]. Therefore, we must consider the dynamics of thin film separation beyond just the type of material removal in order to understand the origin of ultrafast laser printed nanoparticle size control.

It has been previously shown that the intrafilm removal occurs via liquid spallation [Murphy, 2013b] at the trough of the tensile wave within the expanding molten Ni [Leveugle 2004] or the same mechanism as bulk irradiation . We can confirm that the spallation mechanism determines nanoparticle size because the diameter of nanoparticles printed above the plasma

threshold for thin films [Murphy, 2013a] is equivalent to those from bulk irradiation in a reflection geometry [Liu, 2007]. The ejected sheet decomposes into individual particles en route to the target [Rouleau, 2013].

Printing with a 140 μm film-TEM grid separation distance can produce novel nanoparticle shapes. Particles with the hybrid cubic/hemispherical shape seen in Figure 5.3.4(b) only form when material removal occurs due to intrafilm separation. Nanoparticles which are neither cubic nor spherical are known to form when molten material lands on a substrate [Liu, 2007]. These shapes arise because the solid/air interface maintains a constant 90° during solidification, which leads to a non-planar freezing front [Marin, 2014]. The aligned columns of atoms throughout the entire cubic portion of the nanoparticle suggest that solidification nucleates within this "seed crystal like" region. The atomic disorder within the hemispherical portion of these particles may occur to incorporate residual stress from the droplet solidification process [Chin, 1996]. The nanoparticles formed from interface separation have equilibrium shapes at the same separation distance as seen in Figure 5.3.3(d), and we can therefore assume they solidified in transit to the substrate [Murphy, 2013a]. This is consistent with the 500% faster ejection velocity for the intrafilm layer for 20 nm Ni films[Schrider, submitted]. The difference in transit time between the two film removal mechanisms is consistent with nanoparticle solidification on the order of 100 ns.

The slower ejection velocity, in spite of the laser uniformly heating the film, suggests that separation at the interface for the 20 and 10 nm occurs by a fundamentally different mechanism. in which removal occurs due to the nucleation and growth of vapor at the Ni/glass interface [Schrider, submitted]. The removed film leaves a much rougher surface in the ablation crater

[Murphy, 2013b] than liquid spallation during intrafilm separation. Ejection by this nucleation and growth mechanism produces nanoparticles with an average diameter a factor of two lower than removal of the same layer thickness by liquid spallation. We suggest that the nucleation and growth based mechanism causes the region of the film near the fracture to break up into smaller droplets. The total volume of these 3 nm nanoparticles does not account for the entire removed film thickness, which is consistent with some of this layer either remains as the roughness in the ablation crater or breaks up into larger nanoparticles.

The nanoparticle diameters from 5 nm thick films indicate that the removal mechanism more closely resembles liquid spallation. This result suggests that although both removal mechanisms occur within tens of picoseconds [Schrider, submitted], there is a delay before removal via nucleation and growth occurs. The lack of 3 nm nanoparticles is consistent with the 5 nm film being too thin to support the tensile wave within the melt, but spalls at the interface before the vapor has time to nucleate and grow.

In summary, we have demonstrated the ability to control the size of ultrafast laser printed nanoparticles by varying film thickness and fluence to the thin film ablation mechanism. Nanoparticles formed from liquid spallation have an average diameter tied to the thickness of the ejected slab while those formed from the nucleation and growth of vapor at the Ni/glass interface are much smaller than the slab thickness. Asymmetric nanoparticle shapes can be formed by reducing the film-substrate separation distance such that the ejected liquid is still molten when it contacts the substrate. In addition to possible applications as a rapid, one-pot technique for depositing nanoparticles, laser printing is a convenient technique to characterize material ejected after ultrafast laser ablation. This offers an additional avenue to understanding the fundamental

physics of laser-materials interactions, specifically the material's response on timescales long after irradiation.

References

P.V. Kamat, *J. Phys. Chem. C.* **112**, 18737 (2008).

A.J. Nozik *Physica E: Low-dimensional Systems and Nanostructures* **14**, 115 (2002).

A.J. Nozik, F. Williams, M.T. Nenadovic, T. Rajh, and O.I. Micic, *J. Phys. Chem.* **89**, 397 (1985).

S. Pillai, K.R. Catchpole, T. Trupke, and M.A. Green, *J. Appl. Phys.* **101**, 093105 (2007).

H.W. Deckman and J.H. Dunsmuir, *J. Vac. Sci. Technol.* **1**, 1109 (1983).

H. Masuda and M. Satoh, *Japanese J. Appl. Phys*. **35**, L126 (1996).

R. Valeev, E. Romanov, A. Deev, A. Beltukov, K. Napolski, A. Eliseev, P. Krylov, N. Mezentsev, and V. Kriventsov. *Physica Status Solidi (c)* **7**, 1539 (2010).

G. Oskam, Z. Hu, R.L. Penn, N. Pesika, and P.C. Searson. *Phys. Rev. E* **66**, 011403 (2002).

R. Böttger, A. Keller, L. Bischoff, and S. Facsko. *Nanotechnology* **24**, 115702 (2013).

X.B. Zhang and S.K. Hark, *Appl. Phys. Lett.* **74**, 3857 (1999).

J.B. Smathers, E. Kneedler, B.R. Bennett, and B.T. Jonker, *Appl. Phys. Lett.* **72**, 1238 (1998).

S.H. Ahn and J.L. Guo, *Adv. Matr.* **20**, 2044 (2008).

B.Y. Geng, Q. B. Du, X. W. Liu, J. Z. Ma, X. W. Wei, and L. D. Zhang. *Appl. Phys. Lett.* **89**, 033115 (2006).

E. Hao, H. Zhang, B. Yang, H. Ren, and J. Shen. *J. Colloid and Interface Sci.* **238**, 285 (2001).

U. Blieske, T. Kampschulte, A. Bauknecht, M. Saad, J. Sollner, A. Krost, K. Schatke, and M. Ch Lux-Steiner, 26th PVSC, 939 (1997).

J.A. Yater, G.A. Landis, S.G. Bailey, L.C. Olsen, and F.W. Addis, 26th PVSC, 65 (1996).

T.L. Chu, S.S. Chu, Solid State Electron. **38**, 535 (1995).

W. Wang, J. D. Phillips, S. J. Kim and X. Pan, *J. Electron. Mater.* **40**, 1674 (2011).

T. Jia, Q., H. X. Chen, M. Huang, F. L. Zhao, J. R. Qiu, R. X. Li, Z. Z. Xu, X. K. He, J. Zhang, and H. Kuroda. *Phys. Rev. B* **72**, 125429 (2005).

Z. Cen, J. Xu, Y. Liu, W. Li, L. Xu, Z. Ma, X. Huang, and K. Chen. *Appl. Phys. Lett.* **89**, 163107 (2006).

A. Borowiec, and H. K. Haugen, Appl. Phys. A. **79,** 521 (2004).

A. Borowiec and H.K. Haugen, *Appl. Phys. Lett.* **82**, 4462 (2003).

M. Volmer and A. Weber, *Z. Phys. Chem.* (1926).

J. Bonse, S. Baudach, J. Krüger, W. Kautek, and M. Lenzner, *Appl. Phys. A.* **74**, 19 (2002).

A. Cavalleri, K. Sokolowski-Tinten, J. Bialkowski, M. Schreiner, and D. Von der Linde, *J. Appl. Phys.* **85**, 3301 (1999).

X. Wang, T. Jia, X. Li, C. Li, D. Feng, S. Haiyi, S. Xu, and Z. Xu, *Chin. Opt. Lett.* **3**, 615 (2005).

O. Vancauwenbeghre, N. Herbots, and O.C. Hellman, *J. Vac. Sci. Technol*. B. **9.** 2027 (1991).

Z. Liliental-Weber, W. Swider, K.M. Yu, J. Kortright, F.S. Smith, and A.R. Cawala. *Appl. Phys. Lett.* **58**, 2153 (1991).

G. Apostolopoulos, N. Boukos, J. Herfort, A. Travlos, and K. H. Ploog. *Matr. Sci. Engr. B.* **88**, 205 (2002).

V.M. Kaganer, B. Jenichen, R. Shayduk, W. Braun, and H. Riechert, *Phys. Rev. Lett.* **102**, 06103 (2009).

A.Q. Wu and X.Xu, *Appl. Phys. Lett.* **90**, 251111 (2007).

N.V. Lugueva and S.M. Luguev, *High Temp+,* **42**, 54 (2004).

S. Plissard, G. Larriue, X. Wallart, and P. Caroff, *Nanotech.* **22**, 275602 (2011).

M. Prestigiacomo, F. Bedu, F. Jandard, D. Tonneau, H. Dallaporta, L. Roussel, and P. Sudraud, *Appl. Phys. Lett.* **86**, 192112 (2005).

B. Goldstein and D.J. Szostak, and V.S. Ban, *Surf. Sci.* **57**, 733 (1976).

M. Kang, A.A. Al-Heji, J.E. Lee, T.W. Saucer, S. Jeon, J.H. Wu, L. Zhao, A.L. Katzenstein, D.L. Sofferman, V. Sih, and R.S. Goldman, *Appl. Phys. Lett.* **103**, 101903 (2013).

J.A. Van Vechten, *J. Electrochem. Soc.* **122**, 419 (1975).

D.T.J. Hurle, *J. Phys. Chem. Solids.* **40**, 613 (1979).

K.S. Lee, M.A. El-Sayed, *J. Phys. Chem. B.* **39**, 19220 (2006).

A. Albanese, P.S. Tang, and W.C.W. Chan, *Annu. Rev. Biomed. Eng.* **14**, 1 (2012).

E.F. Kukovitsky, S. G. L'vov, N. A. Sainov, V. A. Shustov, and L. A. Chernozatonskii. *Chem. Phys. Lett.*

355, 497 (2002).

T.Y. Kim, S. H. Lee, Y. H. Mo, H. W. Shim, K. S. Nahm, E. -K. Suh, J. W. Yang, K. Y. Lim, and G. S.

Park. *J. Cryst. Growth* **257**, 97 (2003).

A.G. Nasibulin, P.V. Pikhitsa, H. Jiang, and E.I. Kauppinen. *Carbon* **43**, 2251 (2005).

Y. Cui, L.J. Lauhon, M.S. Gudiksen, J. Wang, and C.M. Lieber. *Appl. Phys. Lett.* **78**, 2214 (2001).

M. Sasidharan, N. Gunawardhana, C. Senthil, and M. Yoshio, *J. Mater. Chem. A.* **2**, 7737 (2014).

D. Wei, H. E. Unalan, D. Han, Q. Zhang, L. Niu, G. Amaratunga, and T. Ryhanen, Nanotechnology **19**, 424006 (2008).

S. Huang, L. Dai, and A. W. H. Mau, Adv. Mater. 14, 1140 (2002).

N. R. Franklin, Y. Li, R. J. Chen, A. Javey, and H. Dai, Appl. Phys. Lett. 79, 4571 (2001).

H. Kind, J. M. Bonard, L. Forro, K. Kern, K. Hernadi, L. O. Nilsson, and L. Schlapbach, Langmuir 16, 6877 (2000).

H. Ago, K. Murata, M. Yumura, J. Yotani, and S. Uemura, Appl. Phys. Lett. 82, 811 (2003).

S. I. Anisimov, D. B€auerle, and B. S. Luk'yanchuk, Phys. Rev. B 48, 12076 (1993).

J. Haverkamp, R. M. Mayo, M. A. Bourham, J. Narayan, C. Jin, and G. Duscher, J. Appl. Phys. 93, 3627 (2003).

P. T. Murray and E. Shin, Mater. Lett. 62, 4336 (2008).

S. Amoruso, N. N. Nedyalkov, X. Wang, G. Ausanio, R. Bruzzese, and P. A. Atanasov, J. Appl. Phys. 110, 124303 (2011).

R.D. Murphy, M.J. Abere, K.J. Schrider, B. Torralva, and S.M. Yalisove, Appl. Phys. Lett. 103, 093113 (2013).

J. Bonse, S. Baudach, J. Kruger, W. Kautek, and M. Lenzner, Appl. Phys. A. **74,** 19 (2002).

B. Liu, Z. Hu, Y. Che, Y. Chen, and X. Pan, Appl. Phys. Lett. 90, 044103 (2007).

C.M. Rouleau, C.Y. Shih, C. Wu, L.V. Zhigilei, A.A. Puretzky, and D.B. Geohegan, *Appl. Phys. Lett.* **104**, 193106 (2014).

J. Bohandy, B. F. Kim, F. J. Adrian, and A. N. Jette, J. Appl. Phys. 63, 1158 (1988).

R.D. Murphy, B. Torralva, and S.M. Yalisove, *Appl. Phys. Lett.* **102.** 181602 (2013).

K.J. Schrider, B. Torralva, and S.M. Yalisove, Appl. Phys. Lett. **Submitted** (2015).

R.D. Murphy, Thesis. (2013).

E. Leveugle, D. S. Ivanov, and L. V. Zhigilei, Appl. Phys. A. **79**, 1643 (2004).

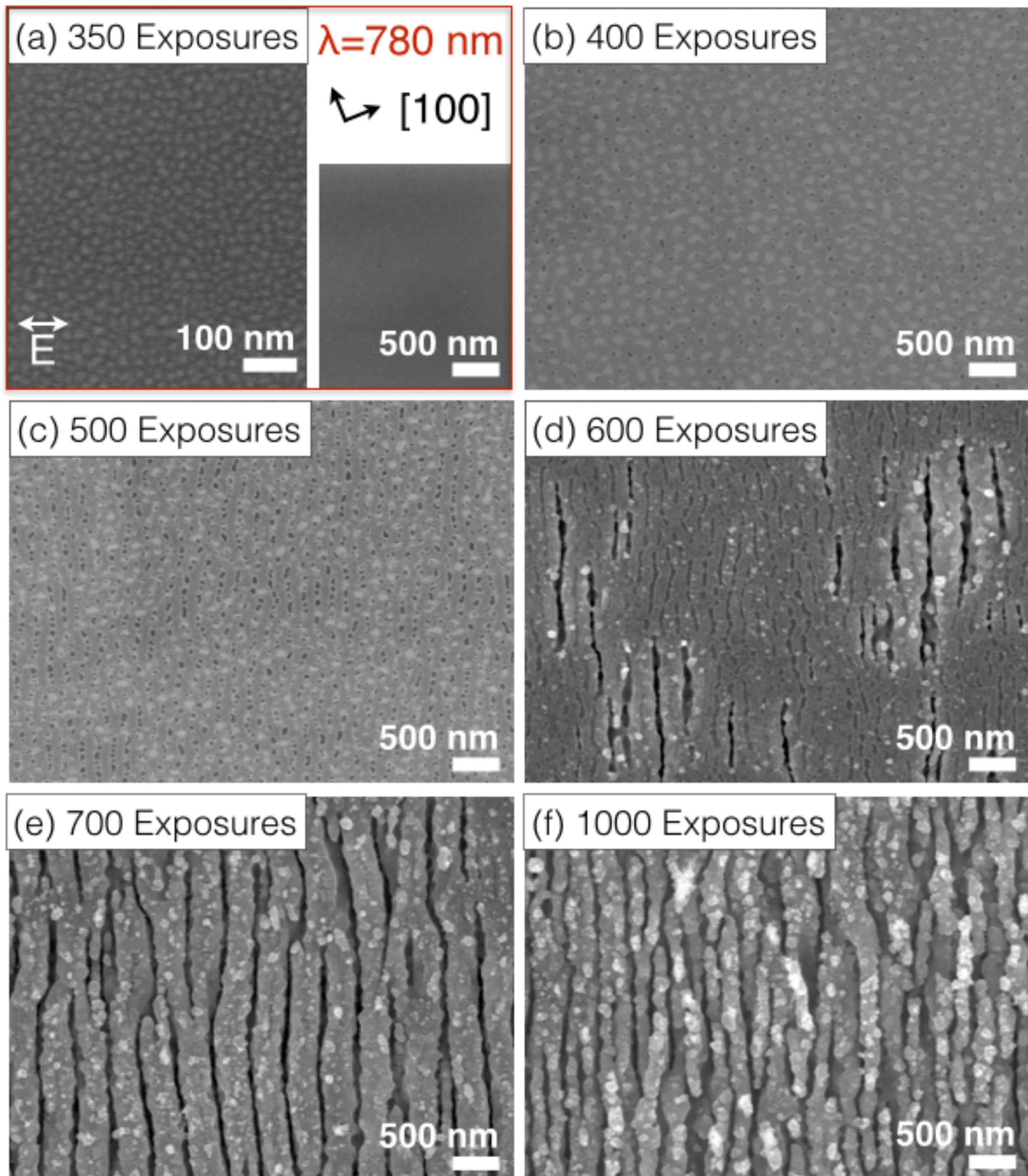

Figure 6.0.1 HSFL formation after irradiation at a fluence of 0.065 ± 0.005 J/cm^2 after (a) 250 (b) 400, (c) 500, (d) 600, (e) 700, and (f) 1,000 exposures. The imaged morphologies are characteristic of laser damage spots with a variance of ± 50 exposures between experiments. The islands and pits in (b) organize into the 165 ± 60 nm population in (c). The LIPSS period first increases to 355 ± 60 nm in (d) and (e) before going through a bifurcation to 180 ± 50 nm in (f).

Chapter 6

Coupled Surface plasmon polariton and Diffusive Mechanisms of High Spatial Frequency Laser Induced Periodic Surface Structure Formation in Semiconductors

The HSFL formation process cannot be explained by an exclusively diffusive or optical model. The HSFL evolve through multiple surface morphologies that each couple differently to SPPs, which changes the local point defect generation rates. Simultaneously, an increasing point defect population places higher strains on the lattice, which changes the defect mobility. An overview of the various surface morphologies arising from mass redistribution that lead to HSFL formation is shown in the SEM images in Figure 6.0.1. LIPSS arise from the distribution of islands that are uncorrelated with the laser polarization, 20 nm in diameter, 40 nm apart, and form within the first 350 exposures in Figure 6.0.1a. Islands coarsen [Abere, 2014] in Figure 6.0.1b to an average diameter of 60 nm after 400 exposures and begin to align into LIPSS perpendicular to the laser polarization. The LIPSS evolve through a series of intermediate 165 nm, 355 nm, and 180 nm periods shown in Figures 6.0.1c, 6.0.1e, and 6.0.1f, respectively. A complete model requires an understanding of both systems and the way in which they interact with each other as the irradiation dose increases. The focus of this chapter will be the way in which the interplay between surface plasmon polaritons and transient surface morphologies

driven by strain relaxation, via diffusing defects, localizes the point defect generation, which results in the evolution and eventual completion of HSFL formation.

6.1 Initial coupling to surface plasmon polaritons

Coupling of surface roughness to SPPs naturally biases HSFL formation perpendicular to the laser polarization by locally enhancing the absorbed intensity. This section will explore how the ultrafast laser excited semiconductor couples SPPs to the island precursors previously discussed in Chapter 5. The island precursors nucleate in GaAs as hemispherical islands with a diameter of 20 nm and a height less than 0.75 nm as shown in the AFM image in Figure 6.1.1. We will begin by considering a single island and determine the way in which its response changes as the island coarsens.

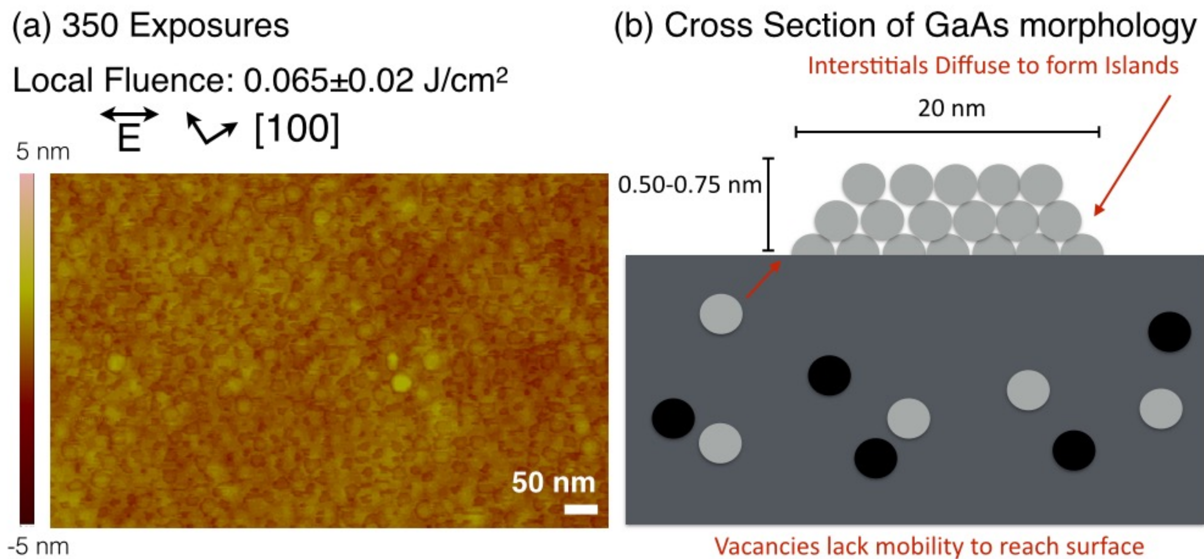

Figure 6.1.1 (a) AFM of 20 nm diameter, 0.50-0.75 nm tall islands formed after 350 exposures at 0.065 J/cm^2. Islands do not orient with respect to the laser polarization or crystal orientation. (b) Schematic representation of the initial morphological change during HSFL formation.

We determined the relative strength of SPP coupling to the islands with a finite element frequency domain calculation [COMSOL]. To model the laser excited GaAs dielectric function for this calculation, we recall Equation 4.1.1 provided for reference below [Sokolowskit-Tinten, 2000]:

$$\varepsilon = 1 + [\varepsilon_g(\hbar\omega + \Delta E_{gap}) - 1] * Ng - \omega_p^2/(\omega(\omega + i\Gamma)$$

(Equation 4.1.1)

where ε_g is the ground state dielectric function [Palik, 1985], ΔE_{gap} is a term for band-gap renormalization, Ng is the fraction of valence electrons in the ground state, ω_p is the plasma frequency, and Γ is the electron collision frequency. Unlike LIPSS formed above the melt threshold [Huang, 2009], it is not sufficient to only consider the Drude term in Equation 4.1.1 for HSFL. Since ultrafast-melt occurs when ~10% of the valence electrons are excited [Stampfli, 1990; Graves, 1998], we can estimate that band-gap collapse occurs when the excited state population density exceeds the order to 10^{22} cm^{-3} in GaAs. For these excited carrier densities, the band renormalization term, which physically represents the sum of exchange-correlation effects and the screened ionic potential, is approximately equal to the GaAs band-gap [Kim, 1994]. Γ is typically on the order of 1 fs for laser excited semiconductors [Sokolowski-Tinten, 2000]. For irradiation at 1.58 eV, the excited GaAs dielectric function was calculated to be -5.74 + 0.22i. The SPP wavelength was calculated using Equation 4.1.2 provided for reference below [Barnes, 2003]:

$$\lambda_{SPP} = \lambda_{Laser} [(\varepsilon_{Re} + \varepsilon_{Air})/(\varepsilon_{Re} \cdot \varepsilon_{Air})]^{1/2}$$
(Equation 4.1.2)

where ε_{Re} is the real part of the dielectric function for the excited GaAs and ε_{Air} is assumed to be one. This resulted in an SPP wavelength of 706 nm.

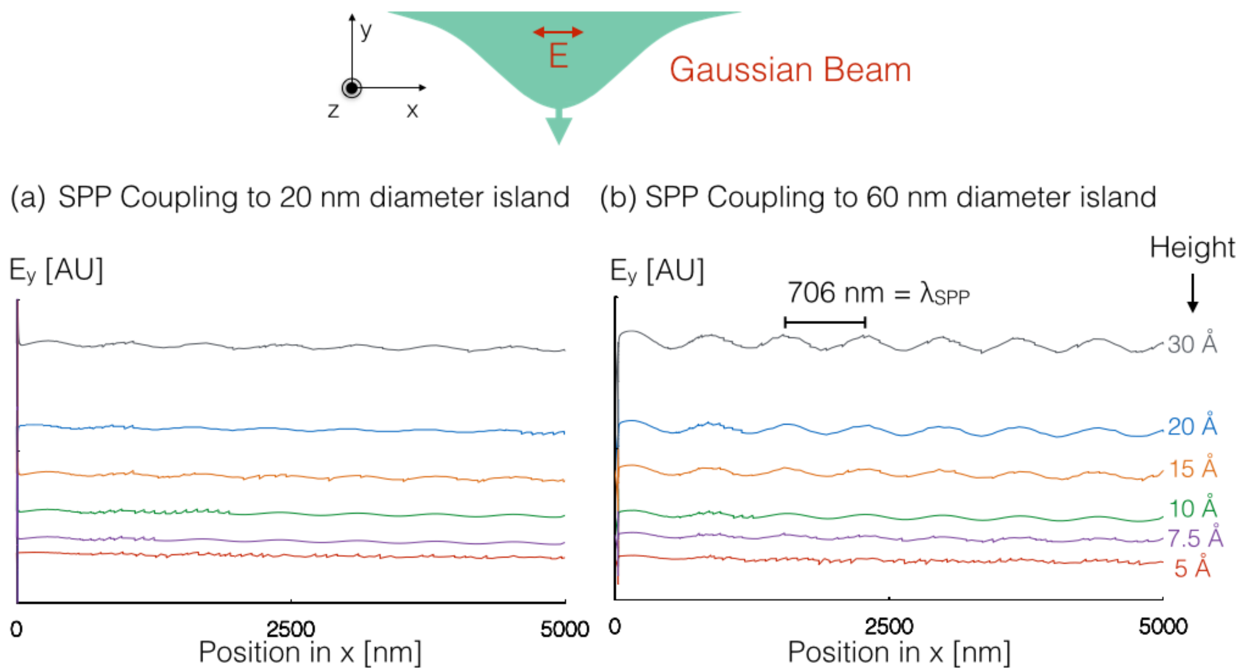

Figure 6.1.2 Frequency domain finite element calculation of the scattered field measured at the air/GaAs interface from an (a) 20 nm and (b) 60 nm diameter hemispherical island. SPP coupling is dependent on height and the relative field strength is dependent on both island height and diameter.

Figure 6.1.2 shows how the strength of SPP coupling is dependent on both structure height and diameter by measuring the propagating scattered field at the air/GaAs interface for 20 and 60 nm diameter islands at various heights. For islands with heights up to 0.50 nm of either diameter, SPP coupling to a single island is not strong enough to cause a propagating wave in the finite element calculation. A propagating polariton is first observed when the dot height of either

diameter exceeds 0.75 nm. The coupling for islands of these heights is not strong enough to induce alignment on the semiconductor surface, which leads to the initially uncorrelated island distribution with respect to laser polarization. The relative intensity of SPP coupling increases both with island height and island diameter, which corresponds to a case where the ongoing coarsening strengthens the SPP coupling to individual islands.

In summary, point defect generation in the bulk semiconductor leads to self-interstitials diffusing to the free surface to form an initial distribution of 20 nm diameter islands. The initial distribution is uncorrelated with the polarization direction because the islands are not tall enough for the SPP to break their symmetry. As the islands coarsen, the taller islands couple more strongly to SPPs, which breaks the symmetry of surface morphology with additional exposures. The way in which the islands align and their period will be the focus of the next section of this chapter.

6.2 Interplay between strain relaxation, via diffusion, and surface plasmon polaritons

The islands not only align into rows perpendicular to the laser polarization, but also take on a 165 nm period in GaAs. This spacing is inherited into the first transient LIPSS observed en route to HSFL formation. In this section, we will determine the way in which strain relaxation, via defect diffusion, and SPPs interact in order to form the 165 nm, 355 nm, and 180 nm LIPSS populations in GaAs.

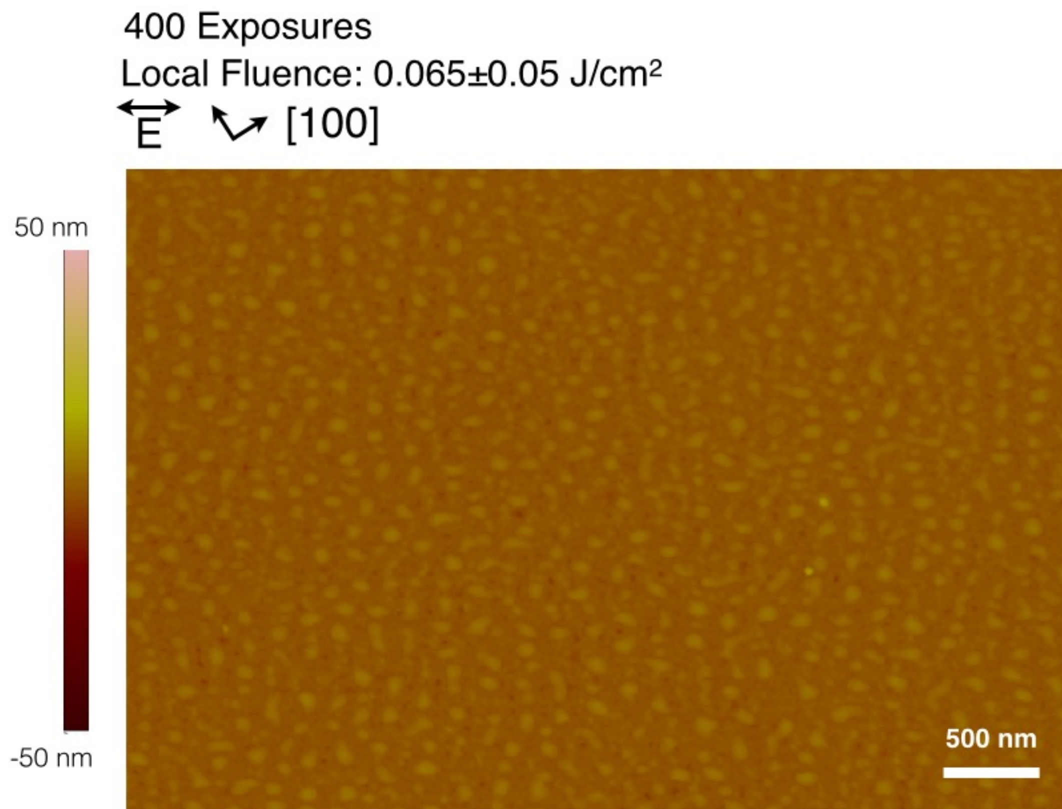

Figure 6.2.1 AFM of islands and pits formed after irradiation with 400 exposures at 0.065 J/cm^2. The islands appear to align into rows with long axis perpendicular to the laser polarization.

Irradiation of the 20 nm diameter islands leads to pit formation between islands as seen in the AFM image in Figure 6.2.1. To find the average spacing between the islands observed after 400 exposures at 0.065 ± 0.005 J/cm^2 in GaAs, we calculated a pair correlation function on the image in Figure 6.2.1. Figure 6.2.2 shows particle detection of AFM images and corresponding pair correlation functions for islands formed after 400 exposures at 0.065 ± 0.005 J/cm^2. Particle detection was performed using Scanning Probe Image Processor™ software. Correlation functions were calculated assuming periodic boundary conditions on the image. The correlation function from a 1 nm island detection threshold in Figure 6.2.2a. While Figure 6.2.1b shows that the AFM image is uncorrelated radially, there are preferential spacings in the direction of the laser polarization in Figure 6.2.2c. The broad peak is centered at 150 nm with a full width half max of 190 nm. Increasing the particle detection threshold to 2 nm in Supplemental Figure 6.2.2c and 6.2.2d raises correlation distance to 165 nm in the direction of the laser polarization. This spacing corresponds to the spacing of coarsened particles when their height reaches 2 nm. The second peak at 330 nm indicates that the surface is starting to become periodic. Alignment of the islands into rows perpendicular to the laser polarization with this 165 nm spacing is only observed in the presence of both islands and pits. It should be noted that the 2 nm islands have an average diameter of 60 nm so the peak at 40 nm spacing is a measurement of the frequency of island agglomeration.

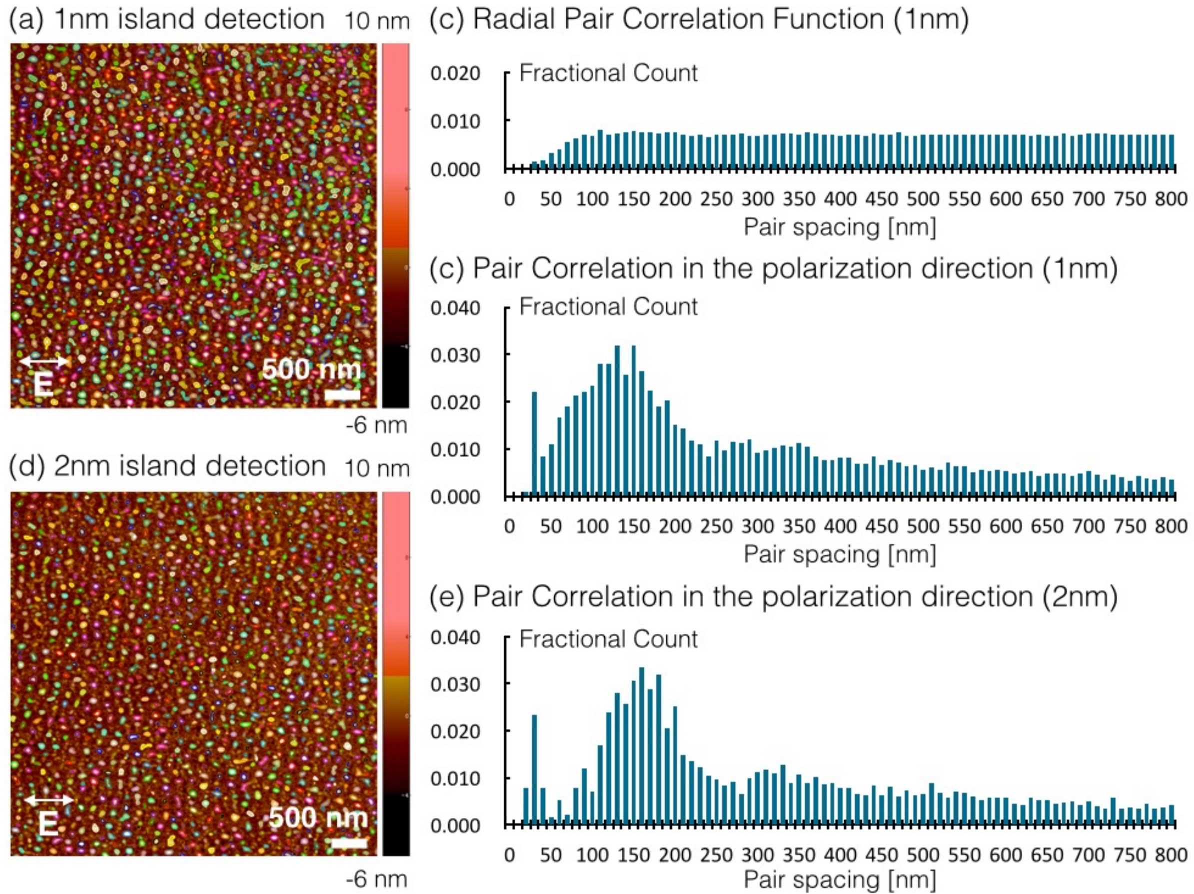

Figure 6.2.2 Island detection of an AFM image with a threshold height of (a) 1 nm, the (b) corresponding radial pair correlation function, and (c) the corresponding pair correlation function in the direction of the laser polarization. The peak is centered at 150 nm with a full width half max of 190 nm. Island detection of an AFM image with a threshold height of (d) 2 nm and the (e) corresponding pair correlation function in the polarization direction. The peak is centered at 165 nm with a full width half max of 100 nm.

To investigate the origin of the 165 nm period observed in the pair correlation function, we characterized the SPP coupling to the aligned islands and pits with finite element frequency domain calculations. For any given spacing, the alternating islands and pits form a grating as shown schematically in Figure 6.2.3a where a* denotes the island diameter and b* denotes the pit width. The coupling of SPPs to a grating allows a photonic band-gap to form in the polariton [Barnes, 1996]. The curvature from this morphology changes the local absorption of subsequent laser pulses, concentrating the absorbed intensity into the sidewalls of the islands and pits as shown in Figure 6.2.3b. SPP coupling in the sidewalls of a grating at a frequency greater than the

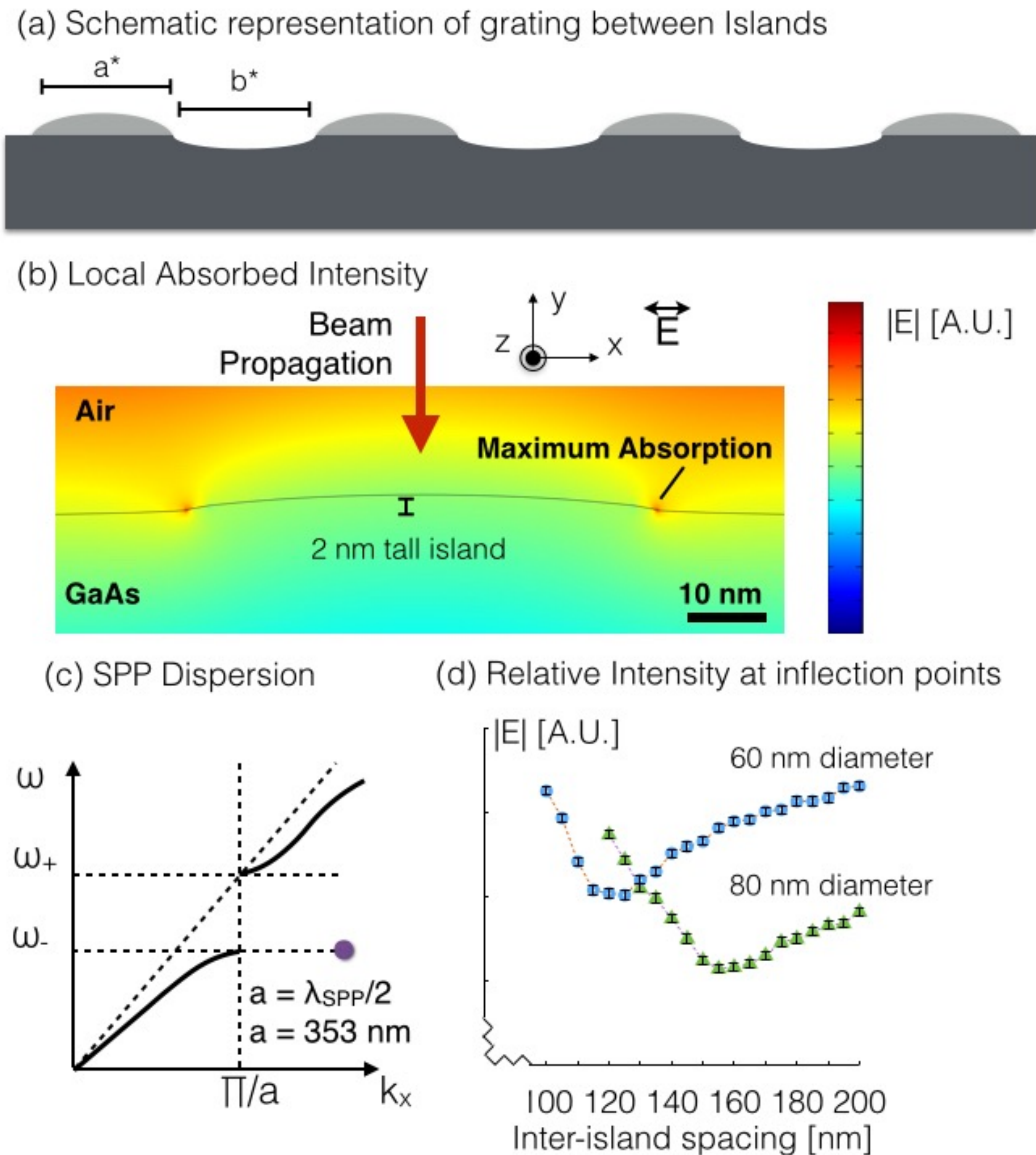

Figure 6.2.3 (a) Schematic of grating formed by aligned islands and pits where a* is the island diameter and b* is the pit width. (b) Finite element frequency domain simulation of locally absorbed laser field from a 2 nm tall island. Absorption is most strongly enhanced in the grating sidewalls. (c) Schematic of grating coupled SP-photonic band-gap dispersion curve. The grating formed by the aligned islands and pits couples to a confined mode off of the dispersion curve signified by the purple dot. (d) Local absorbed intensity in the grating sidewalls for island-to-island spacings with fixed island diameter, height, and trench depth. Absorption is at a minimum for gratings where a* = b*.

band-edge of the SP-photonic band-gap places the strongest absorbing mode is confined off of the SP-photonic band-gap dispersion curve shown in Figure 6.2.3c [Barnes, 2003]. The regions where the SPP enhances absorption experience a higher local defect generation rate, higher mobility, and preferential growth. The competitive nature of coarsening causes only the pits/islands under the most favorable growth conditions to remain.

We calculated the strength of coupling to the confined mode in the grating sidewall with respect to the ratio between a* and b* in Figure 6.2.3d by holding island size and pit height constant while varying the pit width in the grating. Coupling to the sidewalls reaches an absolute minimum when a* = b*. The grating geometry with respect to a* and b* for minimum coupling to the confined sidewall mode is also an absorption maximum when the SPP couples strongly to the mode on the SP-photonic band-gap dispersion curve [Kravets, 2008]. This suggests that coupling for the two modes is a competitive process where the more strongly coupled mode dictates the location of charge separation within each structure. The absorption minimum for the confined mode decreases for larger islands even though the overall SPP coupling is stronger. We would therefore predict that increasing the size of the surface structures would enhance coupling to the mode on the SP-photonic band-gap dispersion curve leading it to become dominant.

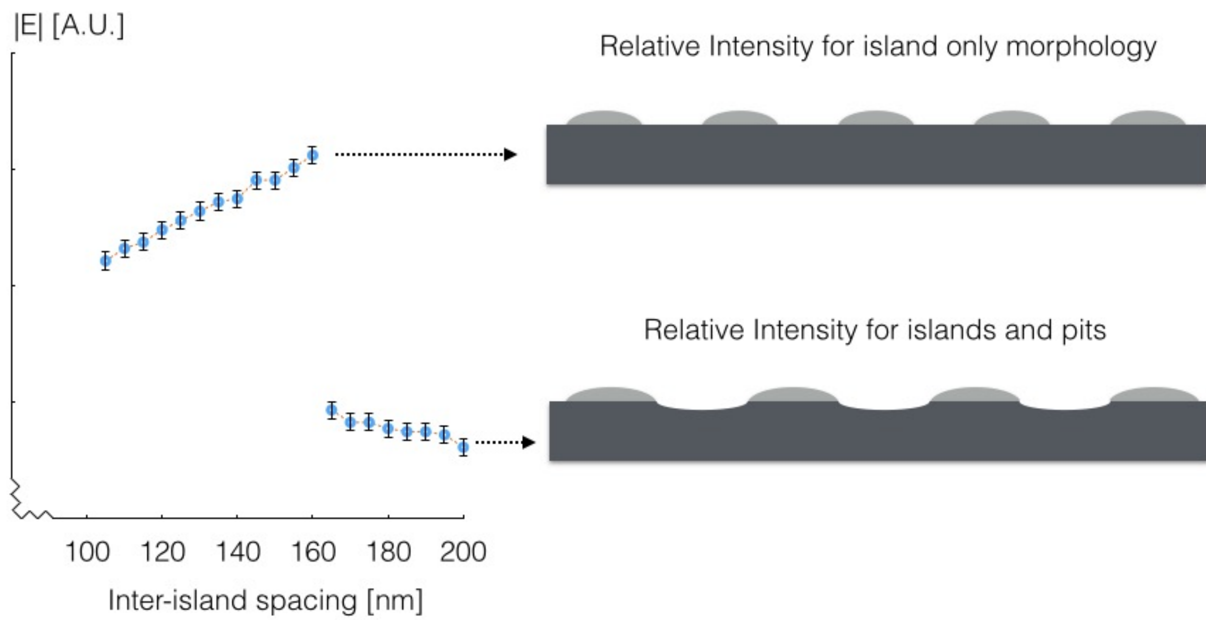

Figure 6.2.4 Relative intensity in the grating sidewall vs inter-island spacing for islands with height and diameter scaled to experimental values. The nucleation of pits causes the local intensity to sharply drop and pins the inter-island spacing.

We propose that the GaAs surface self-organizes to the 165 nm period for our room temperature experiments when continued growth to larger island-to-island spacings would cause a decrease in the defect generation rate. For this calculation, we assumed that island height, diameter, and spacing scale linearly between the initial 20 nm and aligned 60 nm islands and maintained the same growth rate for larger islands. Since the surface begins covered exclusively with islands, we chose to only nucleate pits when the system reached a the 165 nm spacing where they are observed experimentally. A pit height at nucleation of 0.67 nm was used to mirror the islands. The relationship between the growing structures at a given spacing and the local absorbed intensity in the grating sidewall is plotted in Figure 6.2.4. Before pits are allowed to nucleate, the relative absorbed intensity increases as the islands become larger and further apart as height, width, and increasing asymmetry between a* and b* all enhance absorption. However, as soon as pits are allowed to nucleate, the system experiences a sudden drop in local absorption, pinning the system to the existing island-to-island spacing. Allowing the system to continue coarsening under the same conditions after pits nucleate leads to further losses in absorption within the grating sidewalls. The self-organized 165 nm period represents the spacing at which local absorption in the grating sidewall is enhanced enough such that vacancy generation rate and mobility becomes high enough to nucleate a trench. With this in mind, we can now interpret the blueshift in the pair correlation function for islands less than 2 nm tall as coming from structures somewhere along the regime of positive feedback between SPP coupling and coarsening before their spacing is pinned by pit nucleation.

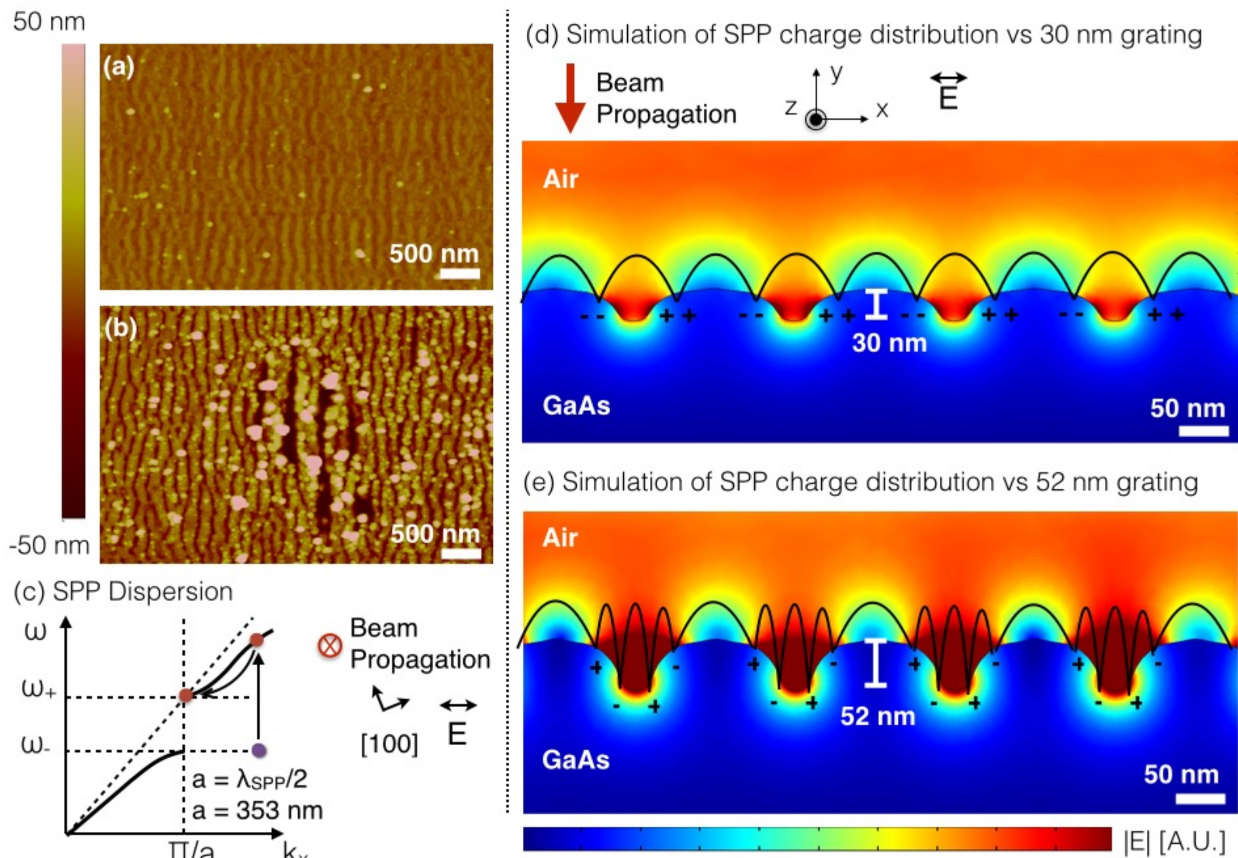

Figure 6.2.5 Atomic force microscopy image of 165 nm grating after (a) 500 exposures, and locally nucleating 355 nm LIPSS after (b) 600 exposures. Fluence in all images is 0.065 ± 0.002 J/cm^2. (c) Schematic representation of the SPP dispersion behavior that leads to the nucleation of the 355 nm LIPSS. Increasing trench depth allows grating coupling of the SPP and the formation of an SP-photonic band-gap. The grating coupled SPP approaches the band-edge from the upper branch (d) Simulation of the 165 nm grating. Charge is confined to the grating sidewalls until the LIPSS amplitude reaches 50 nm in (e). Charge separation to the top and bottom of the trenches indicates that the system is on the upper branch of the SP- photonic band-gap.

The 165 nm LIPSS in Figures. 6.2.5a and 6.2.5b increase in height until a 355 nm population nucleates. The 355 nm period is consistent with a LIPSS period set by the grating coupled SPP wavelength for ultrafast laser excited GaAs [Barnes, 1996; Barnes, 2003]. We suggest that coupling at the band edge ($\lambda = \lambda_{SPP}/2 = 352$ nm), where the SP density of states is the highest, leads to the nucleation of the 355 nm LIPSS. The AFM in Fig. 3B and c shows increasing grating amplitude of the 165 nm LIPSS and eventual transition to a 355 nm period as newly generated interstitials and vacancies diffuse to the structure tops and trench bottoms respectively. The near-field electromagnetic interaction between a laser pulse and the 165 nm LIPSS were modeled with frequency domain finite element simulation. Figure 6.2.5d shows that the surface charge is confined to the side walls of grating trenches less than 50 nm tall. This represents a case where the SPP remains confined off of the SP-photonic band-gap dispersion curve [Barnes, 2003] shown in Figure 6.2.5c. Increasing LIPSS amplitude above 50 nm in Figure 6.2.5e causes the surface charge to separate between the trench top and bottom. This indicates that the SPP can now couple strongly to the upper branch of the SP-photonic band-gap dispersion curve [Barnes, 2003]. The transition from coupling to the upper branch to the band edge, as illustrated schematically in Figure 6.2.5c, demonstrates that the resonant SPP mode dominates over the high energy non-resonant mode with increasing LIPSS amplitude during HSFL formation.

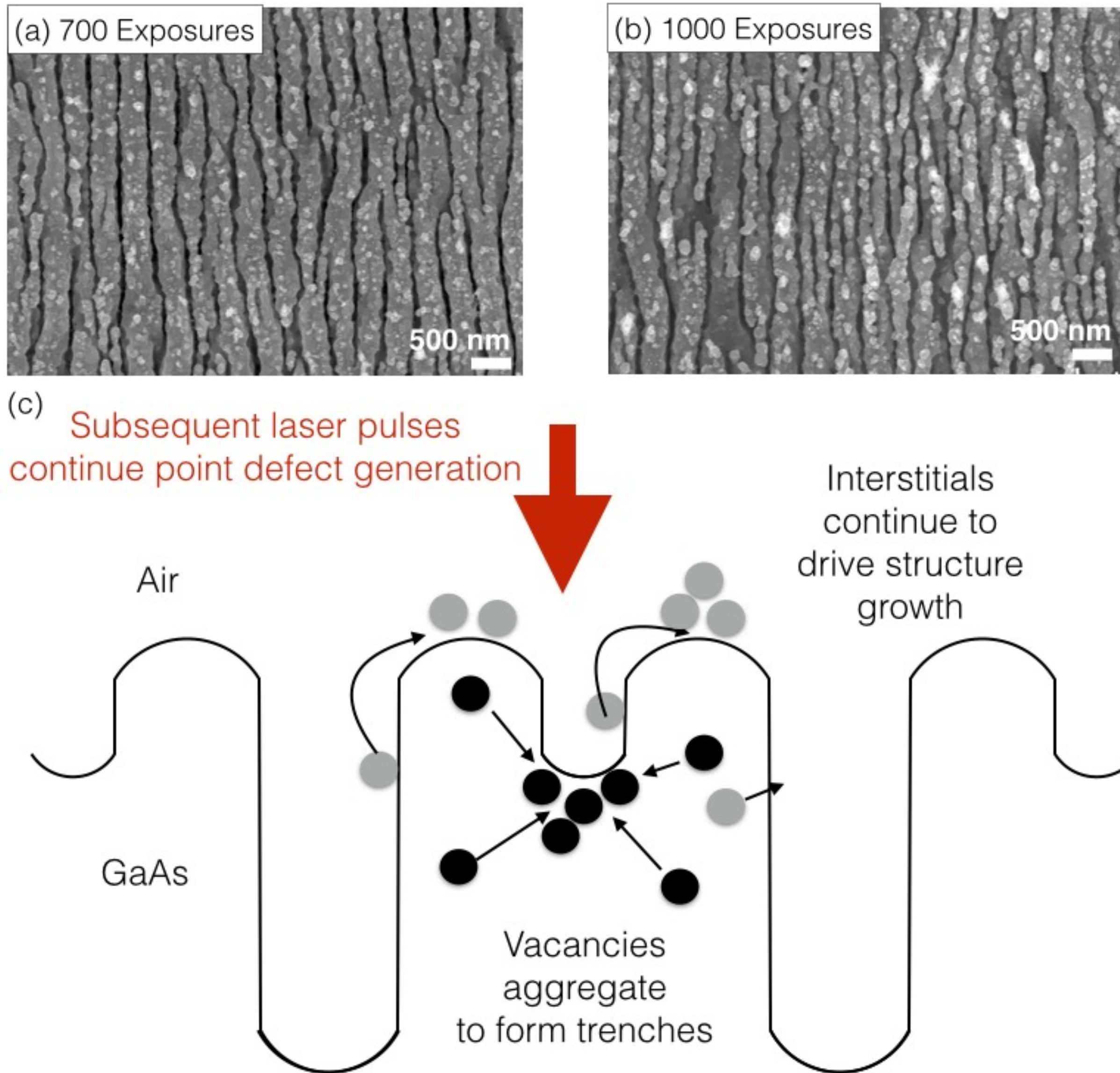

Figure 6.2.6 (a) SEM of 355 nm LIPSS formed after 700 exposures at 0.065 J/cm^2 that bifurcate into (b) 180 nm HSFL after 1,000 exposures. (c) Schematic of strain driven diffusion leading to LIPSS bifurcation.

Continued Vacancy/interstitial pair generation and dissociation within the 355 nm LIPSS leads to strain accumulation in the near surface region [Medhekar, 2009]. Relaxation of this strain provides a potential driving force [Hill, 1975; Young, 1975; Srolovitz, 1989] for the bifurcation from the 355 nm LIPSS in Figure 6.2.6a into the 180 nm HSFL in Figure 6.2.6b. This process is shown schematically in Figure 6.2.6c. The reason that LSFL do not bifurcate, in spite of being capable of forming at the SP-photonic band-edge wavelength[5], is that melting annihilates defects before they can accumulate. The deterministic nature of the ultrafast-melt threshold causes the sharp transition between the two LIPSS populations.

In summary, we have determined that HSFL formation occurs due to ultrafast laser induced point defect accumulation and diffusion. Irradiation within the fluence range between the band-gap collapse and ultrafast-melt thresholds allows for the ultrafast generation of vacancy/interstitial pairs. The HSFL evolve after hundreds of exposures due to the interplay between surface plasmon polaritons and transient surface morphologies driven by strain relaxation, via diffusing defects. The nucleation and growth of HSFL is initially dominated by diffusive processes, then SPPs, and finally back to diffusion during bifurcation.

References

MJ. Abere, C. Chen, DR. Rittman, JD. Phillips, B. Torralva, and SM. Yalisove, *Appl. Phys. Lett.* **105**, 163103 (2014).

K. Sokolowski-Tinten and D. Von der Linde, *Phys. Rev. B*. **61**, 2643 (2000).

E. D. Palik, in Handbook of Optical Constants of Solids, edited by E.D.Palik (Academic, New York, (1985).

P. Stampfli, *Phys. Rev. B*. **42,** 7163 (1990).

J.S. Graves and RE. Allen, *Phys Rev. B*. **58**, 13627 (1998).

D.H. Kim, H. Ehrenreich, and E. Runge, *Solid State Communications*, **89**, 119 (1994).

W.L. Barnes, A. Dereux, and T.W. Ebbesen, *Nature*. **424**. 824 (2003).

W.L. Barnes, T.W. Priest, S.C. Kitson, and J.R. Sambles, *Phys. Rev. B.* **54**. 6227 (1996)

V.G. Kravets, F. Schedin, and AN. Grigorenko, *Phys. Rev. B.* **78**. 205405 (2008).

NV. Medhekar, WL. Chan, V.B. Shenoy, and E. Chason, *J. Phys. Condens. Matter*. **21**, 224021 (2009).

R. Hill and J.W. Hutchinson, *J. Mech. Phys. Solids.* **23**, 239 (1975).

NJB. Young, *J. Mech. Phys. Solids.* **24**, 77 (1975).

DJ. Srolovitz *Acta Metallurgica.* **37**, 621 (1989).

Chapter 7

Effect of Wavelength on Ultrafast Laser Induced Morphology

The wavelength dependence of ultrafast laser interactions is determined by the dominant physical mechanisms active for each specific irradiation condition. In addition to linear photoabsorption, the extreme electric field intensities present during ultrafast laser irradiation can allow for contributions to photo-ionization from tunneling ionization, multi-photon ionization, and avalanche ionization [Schaffer, 2001]. These nonlinear mechanisms are so strong that even materials with band-gaps five times the photon energy can still strongly absorb ultrashort pulses [Gattass, 2008]. In this chapter, we will use our understanding of these various mechanisms to interpret complex laser damage morphologies as well as explain the nonlinear scaling of different material thresholds with respect to wavelength. We will also investigate the wavelength dependence on our point defect generation mechanism and the SPP response during HSFL formation.

7.1 The effect of wavelength above the melt threshold

We examined the wavelength dependence of ultrafast laser damage above the melt threshold. The difference in the material response for semiconductors between wavelengths was determined to be fluence dependent.

The ablation threshold in GaAs was found to be wavelength independent in Figure 7.1.1. However, both melt threshold and crater depth are dependent on laser wavelength. The difference in crater diameter in Figure 7.1.2 is proportional to the difference in focussed spot size for the two experiments. For this reason, the damage spot diameter is normalized to the $1/e^2$ radius in Figure 7.1.1 so that the reader can directly compare crater radius vs fluence at the two different wavelengths.

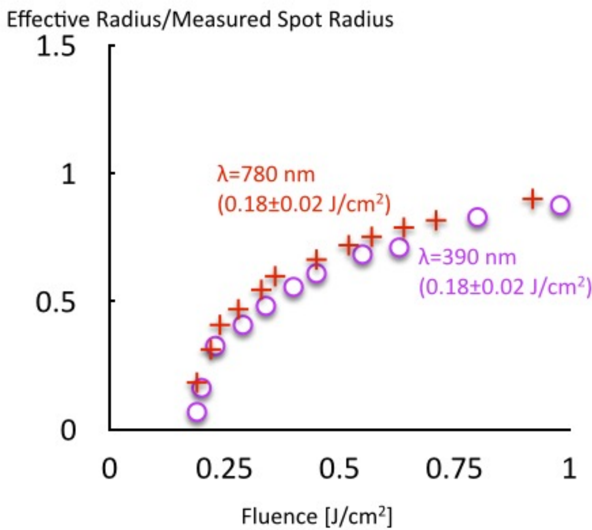

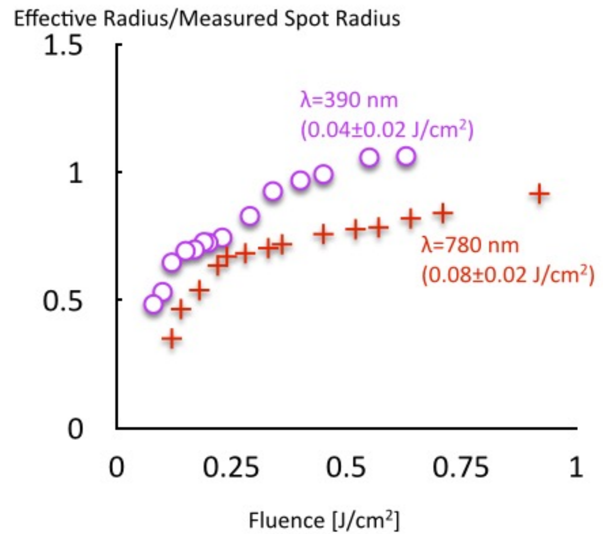

Figure 7.1.1 Calculated damage thresholds for ablation and amorphization of GaAs at $\lambda = 780$ and $\lambda = 390$ nm. (a) Ablation threshold is independent of wavelength (0.18 ± 0.02 J/cm^2). (b) The melt threshold is dependent on absorption at a given wavelength. The melt threshold decreases for $\lambda = 390$ nm from 0.08 ± 0.02 to 0.04 ± 0.02 J/cm^2.

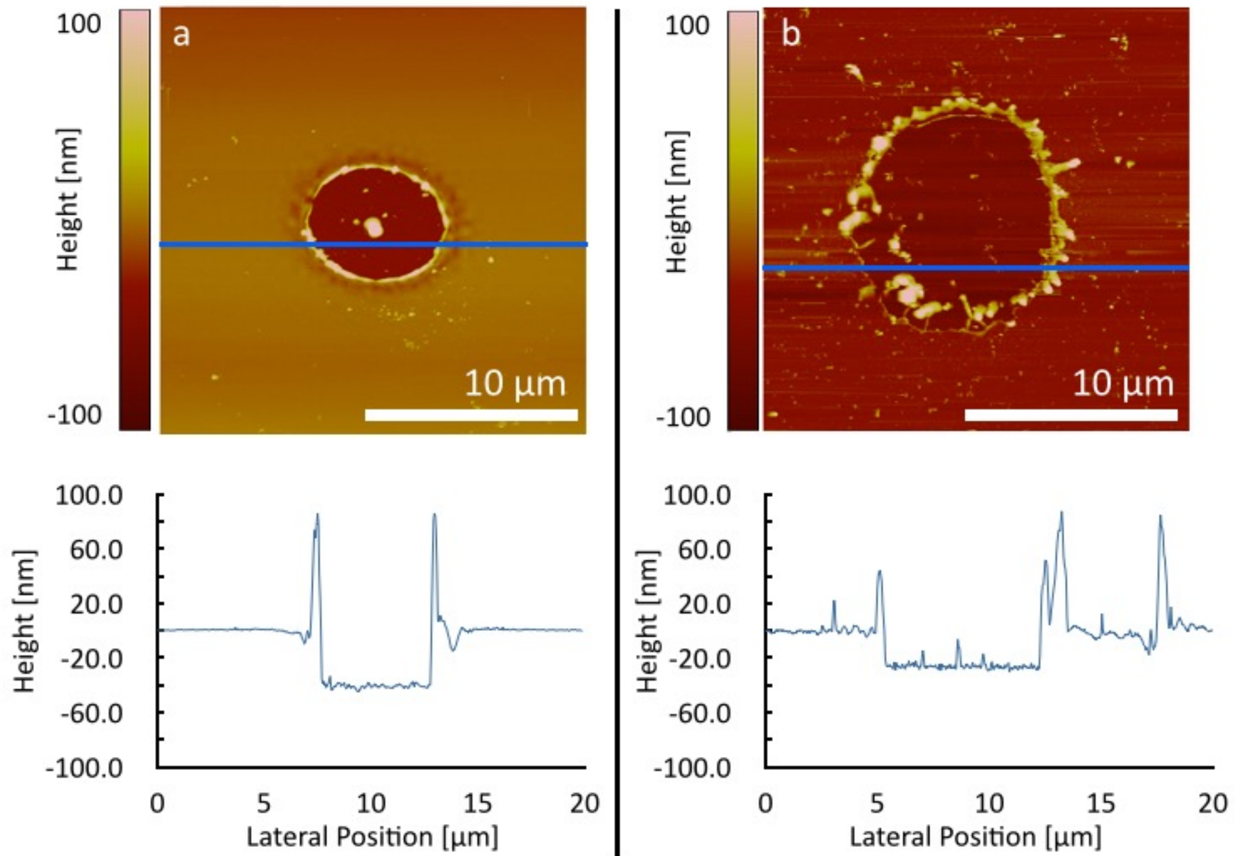

Figure 7.1.2 (a) AFM image of 40 ± 5 nm deep crater in GaAs produced from single exposure irradiation at λ = 780 nm and peak fluence of 0.19 ± 0.01 J/cm^2. Lip height at the crater edge is exaggerated due to a tip artifact. (b) AFM image of 25 ± 5 nm deep crater produced from single exposure irradiation at λ = 390 nm and peak fluence of 0.19 ± 0.01 J/cm^2. Both crater and focussed spot size are 1.5 times larger for this crater. Crater depth between wavelengths is dependent on absorption depth. Additional structure on the crater edge is due to the same fluence absorbed within a smaller volume producing more heating during irradiation at λ = 390 nm.

The melt threshold in semiconductors is entirely dependent on the concentration of non equilibrium carriers excited by the laser. Excitation at both 780 and 390 nm is above the band-gap so linear absorption is the strongest contributor to melting. GaAs has a linear absorption coefficient of 1.48x10^4 cm^{-1} for λ = 780 nm light and 7.42x10^5 cm^{-1} for λ = 390 nm light [Brozel, 1996]. This leads to the decrease in melt threshold to 0.04 ± 0.01 J/cm^2 for λ = 390 nm.

Crater depth after laser irradiation is determined by the depth at which the absorbed fluence is above the ablation threshold [Liu, 1997]. Absorption depth is the reciprocal of absorption coefficient. This leads to the more shallow crater at the same peak fluence in Figure 7.1.3 for λ = 390 nm light. Also, the same fluence is absorbed over a smaller volume and at higher energy levels in the band structure. This causes the GaAs to stay hotter longer and likely contributes to the additional structure on the crater edge.

Understanding that morphology can be tuned by varying both wavelength and fluence, we examined the damage morphologies from irradiation of GaAs (100) wafers with 320 ± 20 nm thick epitaxial films of ZnSe grown in molecular beam epitaxy were irradiated at λ = 780 nm and λ = 390 nm. The system was chosen because of its applications to photovoltaics [Bliske, 2011; Yater, 1996; Chu, 1995; Wang, 2011] and for the relationship of the each layer's bandgap to the laser wavelength. While the GaAs bandgap of 1.42 eV is linearly absorbing for both wavelengths, the ZnSe bandgap of 2.7 eV is large enough so that it is linearly transparent to the fundamental but small enough for two-photon absorption. The ZnSe is then linearly absorbing for the frequency doubled light. To verify whether the ZnSe absorbs the light through two-photon absorption or tunneling ionization, we calculated the Keldysh parameter [Keldysh, 1965; Schaffer, 2001] for the semiconductor using equation 7.1.1:

$$\gamma = \omega/e \cdot (mcn\varepsilon_0 E_g/I)^{1/2}$$

(Equation 7.1.1)

where γ is the Keldysh parameter, ω is the laser frequency, e is the charge of the electron, m is the reduced mass of the electron of $0.17m_e$ [Marple, 1964], n is the refractive index of 2.5 [Adachi, 1991], E_g is the band gap, and I is the laser intensity. For bulk ZnSe ablation at 0.7 J/

cm² [Wang, 2005], this gives a Keldysh parameter of 0.15, which is consistent with tunneling ionization dominating.

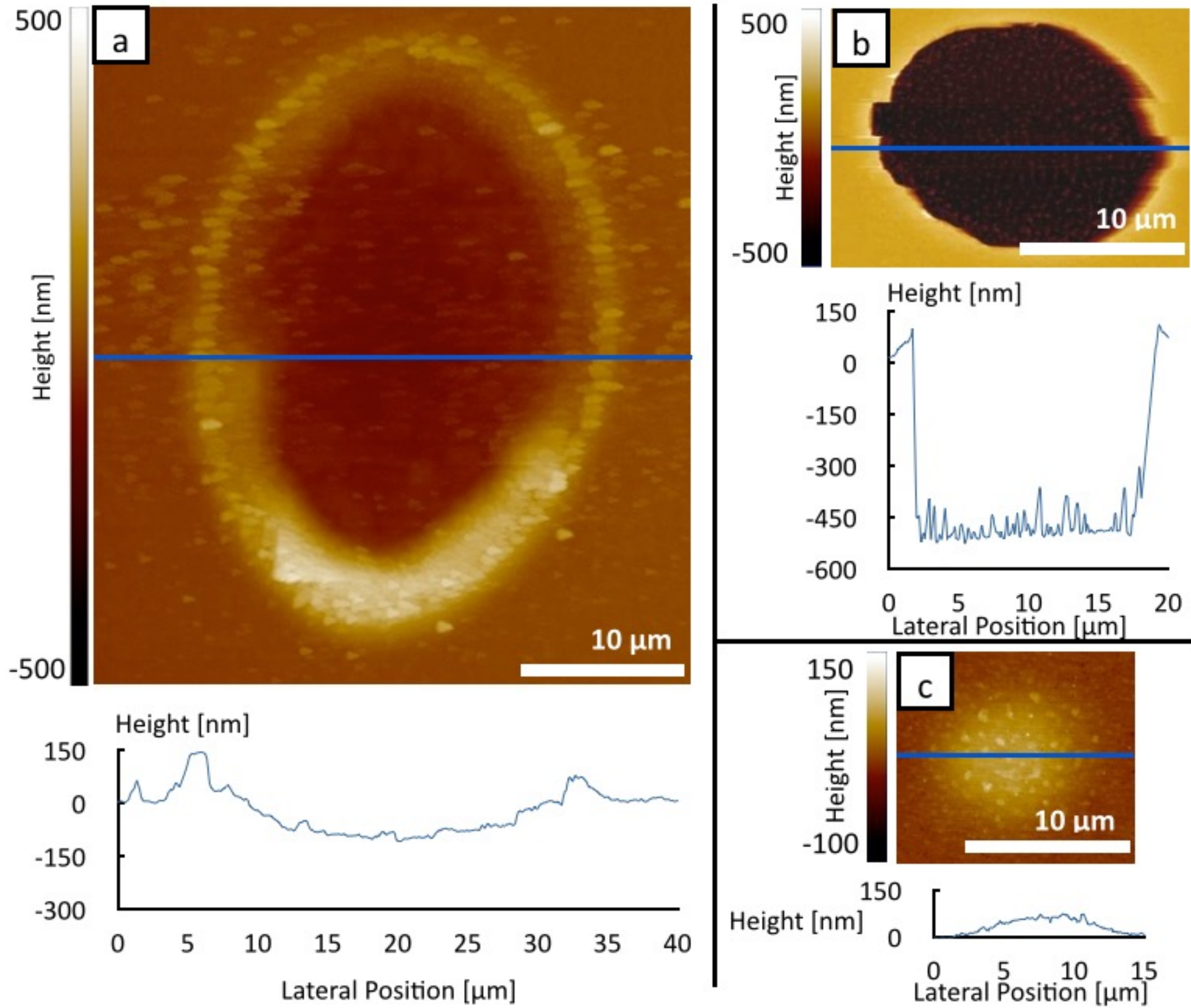

Figure 7.1.3 (a) AFM image of 100 nm deep crater produced from single shot irradiation at λ = 780 nm and peak fluence of 1.0 ± 0.02 J/cm². (b) AFM image of 450 nm deep crater produced from fracture of blister and removal of ZnSe film produced from single shot irradiation at λ = 780 nm and peak fluence of 0.40 ± 0.01 J/cm². The geometric crater edges are caused by fracture along crystal planes and indicate that the film was solid at the time of fracture. The deeper crater at lower fluence occurs because the ZnSe layer becomes strongly absorbing at higher intensity and ablation occurs within the film. c) AFM image of blister produced from single exposure irradiation of a ZnSe film at λ = 780 nm and peak fluence of 0.28 ± 0.02 J/cm². Laser energy is absorbed in and heats the substrate. The film buckling is caused by a release of compressive stress within the film.

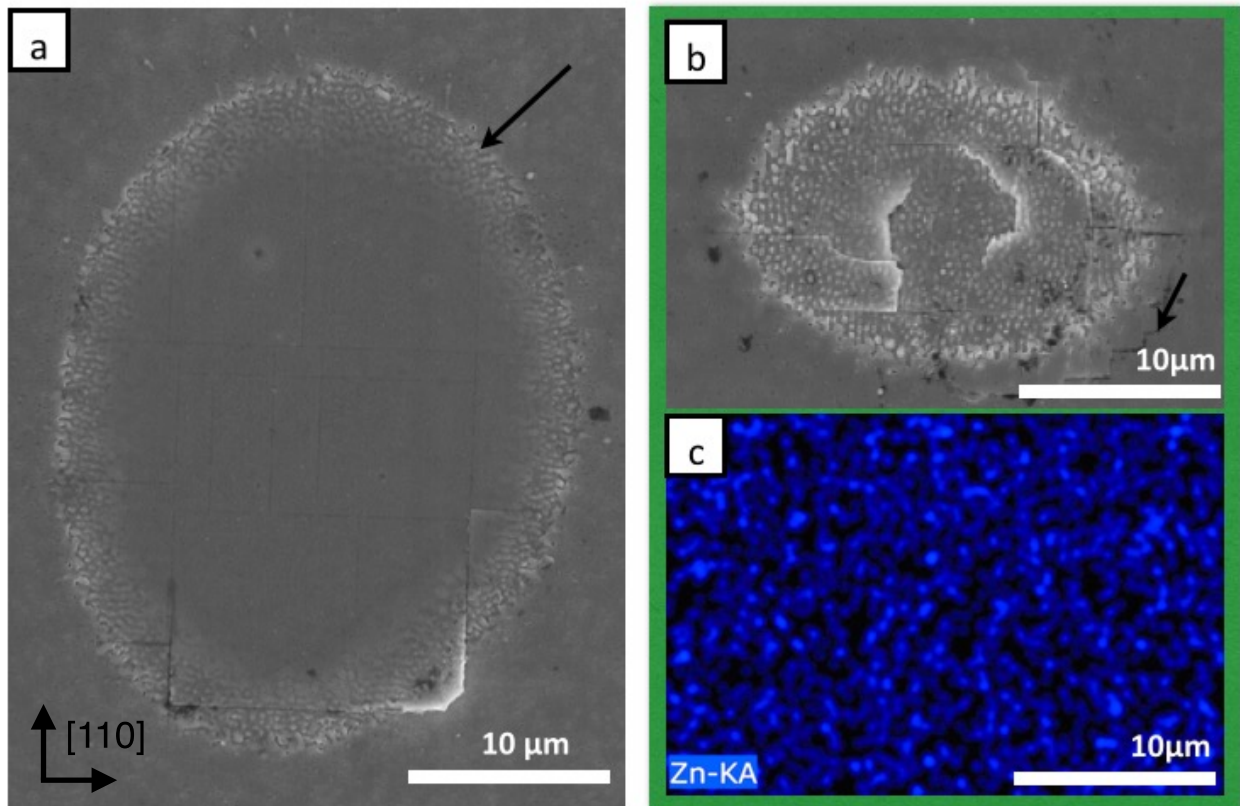

Figure 7.1.4 (a) SEM image of a ZnSe film with a single shot λ = 780 nm laser irradiation with peak fluence of 1.0 ± 0.02 J/cm² produces a uniform contrast surface, which is indicative of ultrafast laser ablation. At local fluence 0.55 J/cm², the same roughness as Fig. 3(b) is observed (see arrow). (b) Single exposure irradiation at 0.50 ± 0.01 J/cm². The roughness and cracking in directions that do not follow cleavage planes is indicative of melting and resolidification. An arrow shows cracking along crystallographic directions at 0.30 J/cm² occurs due to damage in underlying GaAs (c) EDS of the image in (b) showing that the ZnSe is not removed at this fluence

The ZnSe film on GaAs damage morphology after a single exposure at λ = 780 nm is fluence dependent. Craters are formed in the ZnSe at 1.0 ± 0.04 J/cm² and are 100 nm deep in Figure 7.1.3a. An SEM image of a crater from the same fluence as Figure 7.2.3a is shown in Figure 7.1.4a. The central region of the crater surface has uniform SEM contrast in, which is characteristic of femtosecond laser ablation in bulk ZnSe [Wang, 2005]. The ZnSe surface roughness contrast (see arrow in Fig. 3a) occurs at 0.55 ± 0.04 J/cm² and correlates to the morphology depicted in Figure 7.1.4b at peak fluence 0.50 ± 0.04 J/cm². Cracks within the film

are observed at the center of the spot in Figure 7.1.4b do not follow crystallographic directions. The AFM of this rough region in Figure 7.1.3a is consistent with the EDS in Figure 7.1.4c showing that the ZnSe film is not removed. Cracking along the film's crystallographic directions is observed at the arrow in Figure 7.1.4b, which correspond to a range of local fluences between 0.40 and 0.30 ± 0.04.

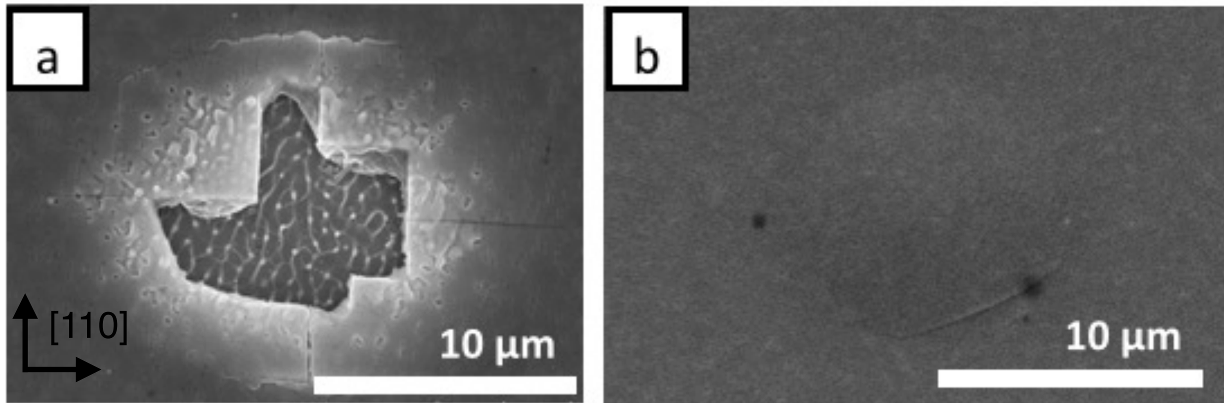

Figure 7.1.5 (a) SEM of crater at a fluence of 0.30 ± 0.01 J/cm^2. The geometric edges along cleavage planes indicate fracture occurred with a solid ZnSe film. (b) SEM of Blister formed in the ZnSe at a peak fluence of 0.26 ± 0.04 J/cm^2.

Craters deeper than the nominal thickness of the film form after irradiation at peak fluences within the range of 0.30 and 0.40 ± 0.04 J/cm^2. An AFM and SEM of craters within this regime are shown in Figures 7.2.3b and 7.2.5a respectively. Craters have geometric edges aligned to crystallographic directions in the film. Approximately 100 nm wide structures with high length to width ratio form in the exposed GaAs in Figure 7.1.6a that were not visible after irradiation with the same fluence on bare GaAs. Reducing peak fluence to 0.26 ± 0.04 J/cm^2 produces blisters on the film surface. Blisters remain intact over a fluence range smaller than the shot to shot variation of our laser. A comparison of the formation mechanism for the two crater species will be discussed below.

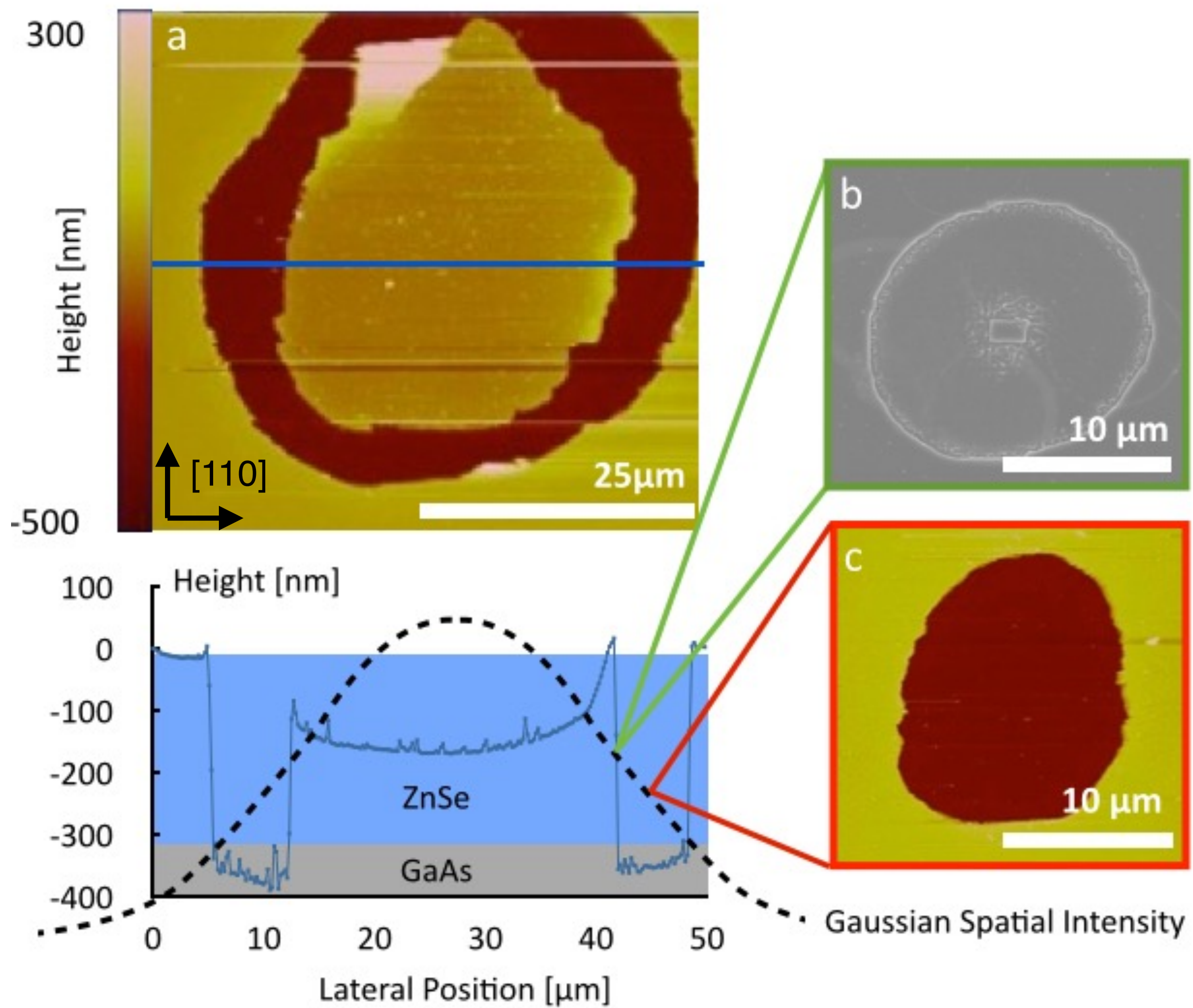

Figure 7.1.6 (a) AFM image of a washer-like morphology on a ZnSe film produced by single exposure irradiation at λ = 390 nm with peak fluence 0.80 ± 0.04 J/cm^2. The central bowl shaped pedestal is caused by absorption and ablation in the ZnSe. The 350 nm deep ring is caused by absorption and ablation in the GaAs. The pulse's Gaussian spatial intensity is overlaid on the height profile to demonstrate that each morphology is dependent on local fluence. (b) SEM image of damage produced by single exposure at 0.57 ± 0.04 J/cm^2 and λ = 390 nm. The central ZnSe pedestal has a rectangular cross section. The material fractured on cleavage planes because it was solid and crystalline at the time of fracture. When the peak fluence approaches threshold, rectangular pedestals are observed because the smaller radius of constant local fluence at threshold causes a reduced variance along a single cleavage plane. (c) AFM image of crater formed when peak fluence (0.45 ± 0.04 J/cm^2) is at the local fluence where ring formation occurs.

Changing the irradiation wavelength produced unique morphologies in the ZnSe/GaAs system. A bowl shaped pedestal surrounded by a 350 nm deep ring shown in 7.1.6a is produced after irradiation with a single λ = 390 nm pulse at 0.80 ± 0.04 J/cm^2. The pulse's Gaussian intensity distribution is superimposed on the AFM trace in Figure 7.1.6a to help visualize the local fluence dependent morphology. The center of the pedestal is 150 nm below the original surface and has geometric edges. The AFM height profile in Figure 7.1.6a is not symmetric at the pedestal edge because the film has delaminated on one side of the trace and is curling upward. In the ring shaped damage region, material removal is greater than the nominal thickness of the film and energy dispersive x-ray spectroscopy shows that the ZnSe film has been removed. The ring occurs between local fluences of 0.56 ± 0.04 and 0.40 ± 0.04 J/cm^2.

Irradiation at a peak fluence just above the pedestal edge local fluence (0.57 ± 0.04 J/cm^2) produces a rectangular pedestal with an elliptical beam shown in Figure 7.1.6b. The pedestal edges are aligned with the crystallographic directions in the film. When the peak fluence approaches threshold, the smaller radius of constant local fluence at threshold causes a reduced variance along a single cleavage plane, which allows for the formation of rectangular pedestals with an elliptical beam. Irradiation at a peak fluence equivalent to the ring's local fluence produces a 350 nm deep crater shown in Figure 7.1.6c. The crater edge occurs at a local fluence of 0.40 ± 0.04 J/cm^2.

The observed ZnSe/GaAs morphologies do not behave like their bulk damage counterparts at the same fluence. However, we can use our understanding of semiconductor melting and ablation to interpret the different damage morphologies as well as which layer

absorbed the laser energy. The blisters formed in the ZnSe from 780 nm irradiation at 0.26 J/cm^2 in Figures 7.1.3c and 7.1.5b require that the top layer remains transparent to the beam so that the underlying material can melt [McDonald, 2006]. Blisters can thus only form after irradiation with light at energies below the ZnSe band-gap and do not form after irradiation at λ=390 nm.

Moreover, the direction of the cracks in the ZnSe depend on the its state during fracture. The cracks observed after irradiation at 0.50 J/cm^2 in Figure 7.1.4b do not follow the ZnSe cleavage planes, which indicates that the ZnSe became molten. Conversely, the cracks follow cleavage planes for the fractured film in Figure 7.1.5a, which indicates that the ZnSe was still solid at the time of fracture. Therefore, a second condition on blister formation is that the transparent layer cannot be excited above its melt threshold or the compressive stress [Serano, 2002; McDonald, 2006] will be released during the phase transition instead of through buckling.

The relationship between GaAs crater depth and wavelength is reversed in ZnSe. The ZnSe ablation craters are 150 nm deep for 0.80 J/cm^2 and λ = 390 nm (Figure 7.1.6) and 100 nm deep at 1.0 J/cm^2 and λ = 780 nm (Figure 7.1.3). The more shallow crater for the longer wavelength is consistent with the two-photon absorption depth being smaller than the single photon absorption depth in ZnSe. This is analogous to absorption in Si, another zinc-blende semiconductor [Reitze, 1990].

We would expect that the single photon absorption in ZnSe would be strong enough such that no energy is absorbed in the GaAs underneath for a film with thickness three times the absorption depth [Adachi, 1991]. The central region of the pedestal in Figure 7.1.6a forms due to ablation within the ZnSe film. However, irradiation at a local fluence of 0.45 J/cm^2, above the

ZnSe melt threshold [Abere, 2014], in Figure 7.1.7 causes not only removal of the entire ZnSe film, but also ablation in the GaAs. Ablation in the GaAs is consistent with the laser pulse with a photon flux of 8.8×10^{17} cm^{-2} at 0.45 J/cm^2 saturating the ZnSe density of states of 3.3×10^{16} states/eV-cm^2 for a 300 nm thick film [Wang, 1981]. It follows that the semiconductor band structure remains intact throughout the duration of the pulse even for fluences above the melt threshold. It is likewise a valid assumption that changing the laser wavelength can allow us to couple to different states at the same excited carrier concentration, which may allow for control over ultrafast point defect generation. The way in which the laser wavelength changes point defect generation and the resulting morphologies will be discussed in the next section of this chapter.

The saturation of the density of states also leads to the equivalence in the semiconductor's ablation threshold between 780 nm and 390 nm light. For the 390 nm irradiation, the number of electrons excited by linear absorption is more than an order of magnitude too small to cause ablation in the material due to Pauli exclusion. The Kelydsh parameter for the 390 nm light of 0.30 is still within the range where it is valid to assume that tunneling ionization is the only active nonlinear absorption mechanism [Lin, 2004]. Tunneling ionization is wavelength independent [Ammosov, 1986; Yan-Zhou, 2012] and therefore the ablation threshold appears wavelength independent for semiconductors as long as the density of states remains low and the Kelydsh parameter remains in the purely tunneling ionization regime below 0.5 [Lin, 2004].

In summary, experiments investigating the material response to ultrafast laser irradiation demonstrate that multiple damage morphologies from a single exposure can be interpreted based on local fluence. Within the ZnSe/GaAs material system, damage morphology is determined by which layer is the primary absorbing layer. ZnSe becoming a strong absorber above the ablation threshold causes more shallow craters to form with higher fluence. We also demonstrate the ability to determine a single crystal's phase at the time of material removal based on crack propagation within the film. Crater depth allows us to qualitatively determine that the two-photon absorption depth of ZnSe is less than its single photon absorption with a simple experimental setup. Finally, the semiconductor retains its band structure during absorption for a range of fluences above the melt threshold, while ablation at both wavelengths is dominated by tunneling ionization even when the semiconductor can linearly absorb the light.

7.2 Control of HSFL formation with laser wavelength

The HSFL wavelength is typically proportional to the laser wavelength but does not scale in a 1:1 fashion [Boroweic, 2003; Bonse, 2012]. In this chapter, we will use our knowledge of the HSFL formation mechanism to explain this nonlinearity in period vs wavelength. We will also show that it is possible to choose a wavelength at which HSFL formation can be turned off by controlling the SPP response.

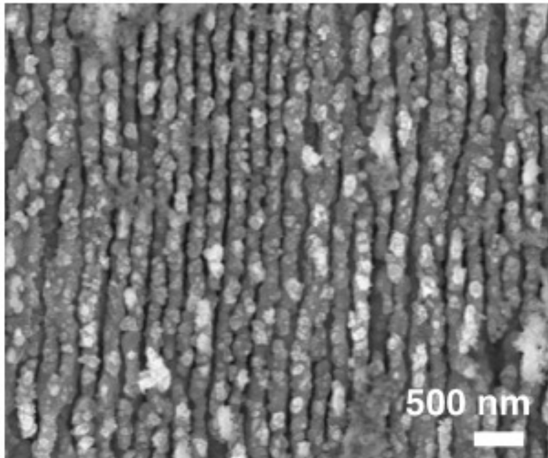

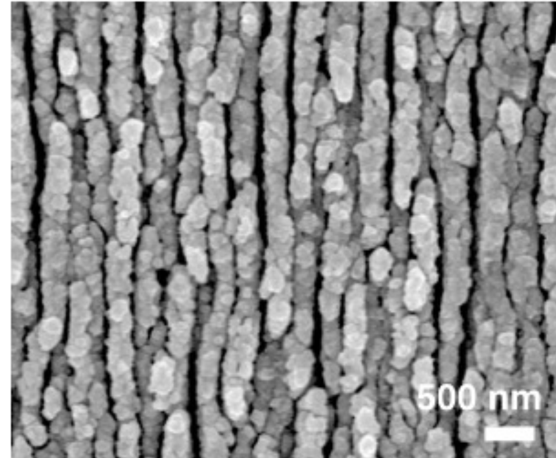

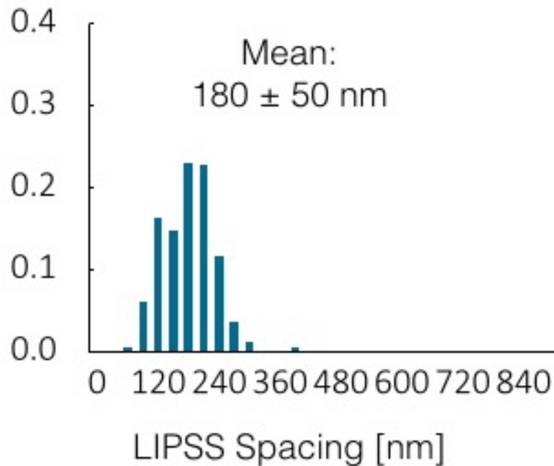

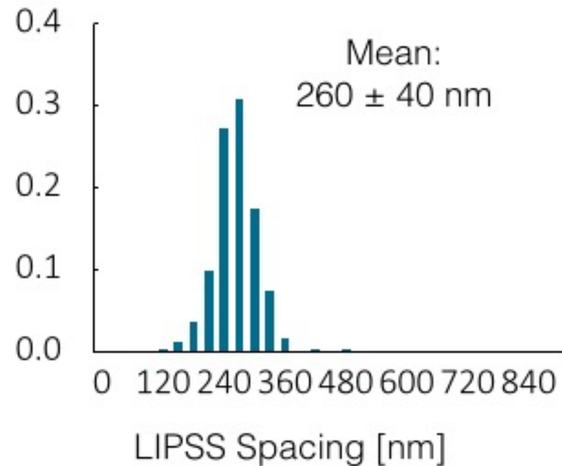

Figure 7.2.1 (a) HSFL with period 180 nm formed at 0.065 J/cm^2 and 1,500 exposures from irradiation with 780 nm light. (b) HSFL with period 260 nm formed at 0.085 J/cm2 and 1,000,000 exposures from irradiation with 1064 nm light. The HSFL wavelength is equal to half the grating coupled SPP wavelength for a each laser wavelength.

To recall from Chapter 4, irradiation with a 780 nm beam produced HSFL with a period of 180 nm. An image of these LIPSS and a distribution of their spacing are provided in Figure 7.2.1a. HSFL were also formed using a femtosecond laser with a central wavelength of 1064 nm with a pulse duration of 600 fs and are shown in Figure 7.2.1c. HSFL formed when either a 100

kHz or 1 mHz repetition rate were used. Based on the processing window for HSFL formation, the melt and band-gap collapse thresholds for this laser both increased to 0.12 ± 0.01 J/cm^2 and 0.080 ± 0.005 J/cm^2 respectively. The resulting HSFL in Figure 7.2.1b formed after 1,000,000 exposures at 0.085 ± 0.005 J/cm^2 have a period of 260 ± 60 nm. The higher thresholds and greater number of exposures required for formation are both consistent with weaker absorption below the GaAs band-gap and lower intensity from the longer pulse.

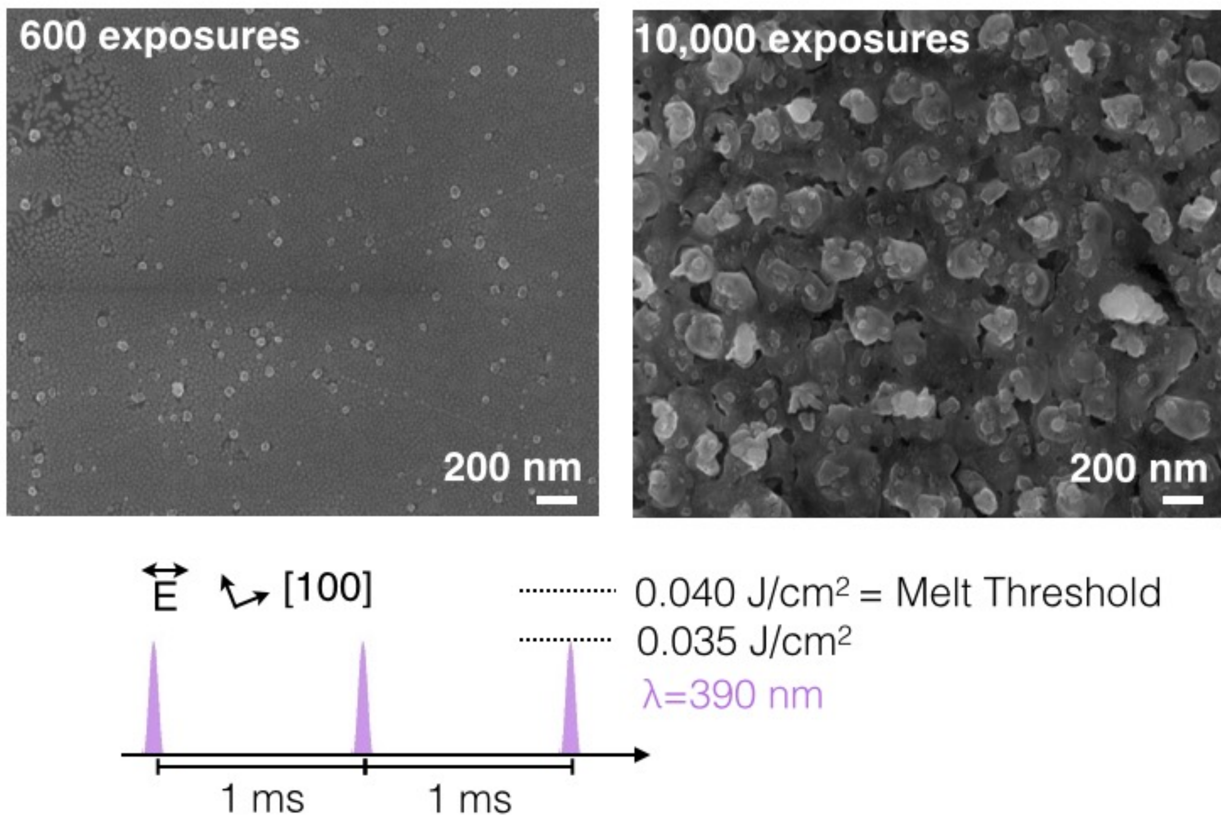

Figure 7.2.2 HSFL do not form when the 780 nm beam is frequency doubled to λ=390 nm for fluences between band-gap collapse and the melt threshold. Instead, only the nanodots covered in Chapter 5 are observed and additional exposures increases their diameter without causing organization perpendicular to the laser field due to the fact that the GaAs does not become metallic at this wavelength so there is no SPP.

No HSFL are observed when the 780 nm (150 fs pulse, 1 kHz) beam was frequency doubled to λ=390 nm. Figure 7.2.2a shows that the precursor nanodots still form below the melt threshold after 600 exposures at 0.035 J/cm^2. However, even after 10,000 exposures neither the initial transient LIPSS, the grating coupled SPP period LIPSS nor the HSFL form. Instead, the nanodots continue to increase in diameter without organizing.

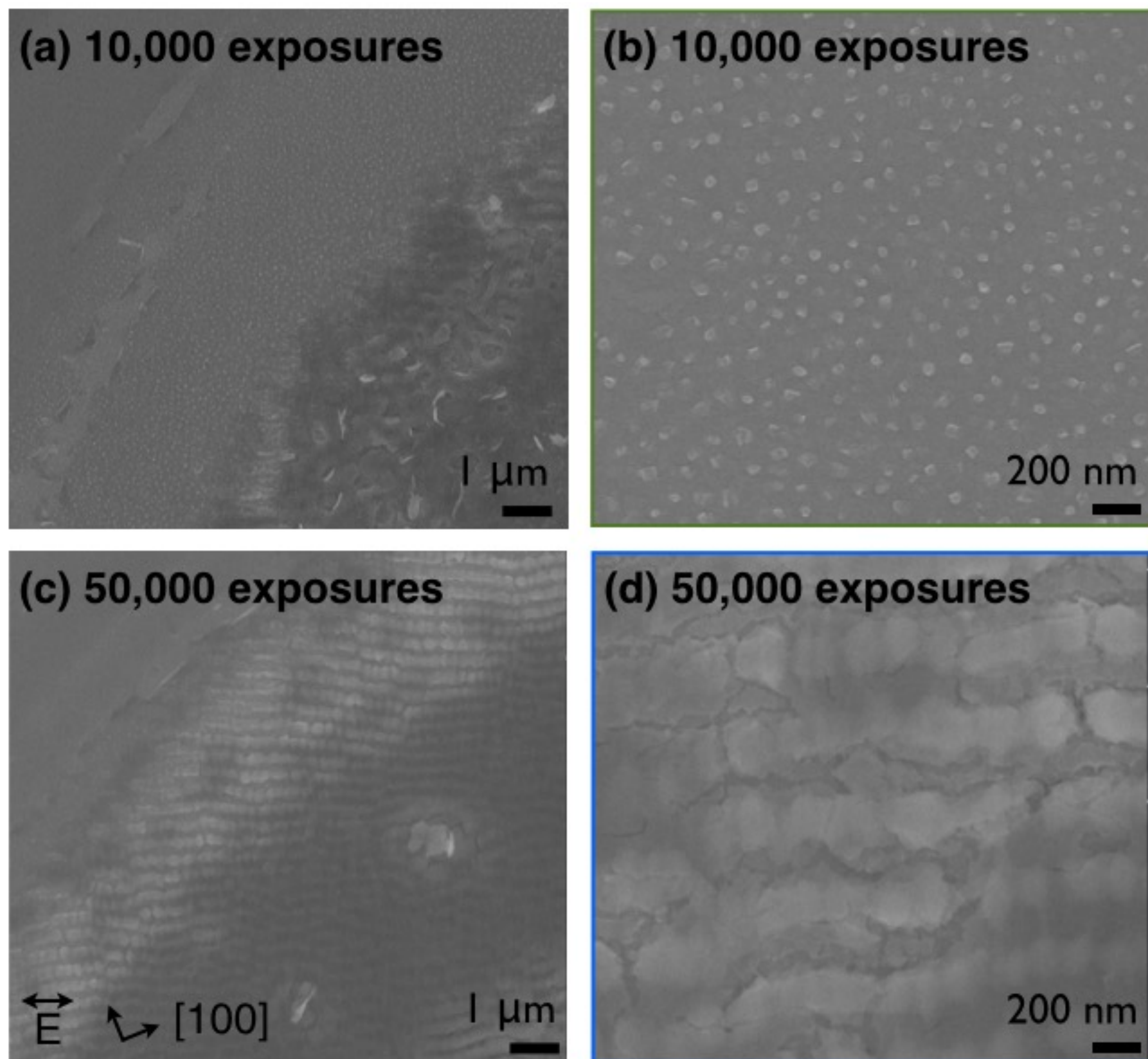

Figure 7.2.3 (a) and (b) Nanodots formed after 10,000 exposures at 0.004 ± 0.002 J/cm^2 in GaAs after irradiation at λ=390 nm. (c) and (d) Continued irradiation to 50,000 exposures at the same fluence causes the nanodots to organize into LIPSS with period equal to the 390 nm laser wavelength that are parallel to the laser polarization. Such LIPSS are only observed in the absence of SPP coupling.

The formation of nanodots from the 390 nm light persists down to 0.003 ± 0.002 J/cm^2. Nanodots formed after 10,000 exposures at 0.004 ± 0.002 J/cm^2 are shown in Figures 7.2.3a and 7.2.3b. While the ratio between the melt and band-gap collapse thresholds in semiconductors is 2:1 for 780 nm light for GaAs - a trend that also holds true for Si [Huang, 1997] - doubling the light's frequency has separated the two by an order of magnitude. The difference is even greater in ZnSe where the thresholds are separated by more than two orders of magnitude [Abere, 2014].

The LIPSS that form after irradiation with the frequency doubled light are not HSFL, but rather have a wavelength equal to that of the laser. In addition, they orient parallel to the laser polarization. An example of these parallel LIPSS formed after 50,000 exposures at 0.004 ± 0.002 J/cm^2 are shown in Figures 7.2.3b and 7.2.3c. The LIPSS have instabilities along their long axis similar to those observed in the initial transient LIPSS formed from the island organization after irradiation with the 780 nm light.

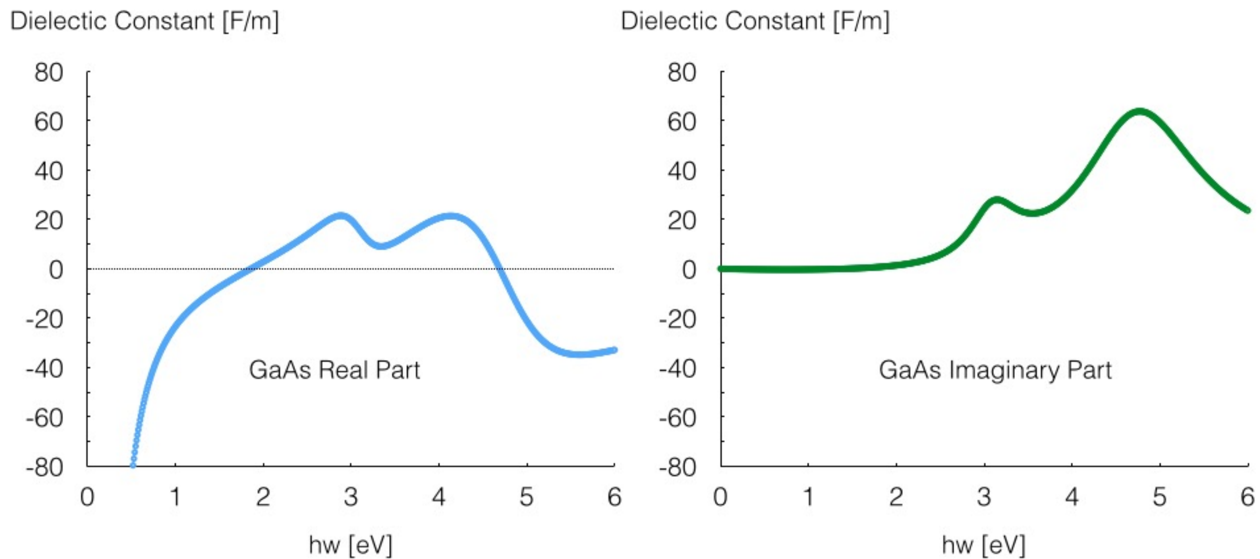

Figure 7.2.4 Calculated complex dielectric function for laser excited GaAs above the band-gap collapse threshold with an excited electron concentration of 10^{22} cm^{-3}.

The nonlinear shift in period and ability to turn off the HSFL formation mechanism can both be attributed to the SPP semiconductor's SPP response at the different wavelengths. As we established in the previous section of this chapter, the semiconductor's band-structure remains intact during the first 150 fs and therefore the SPP response will be influenced by the dielectric function at the irradiation wavelength. To determine this response, we calculated Equation 4.1.1 [Sokolowski-Tinten, 2000] for energies between 0 and 6 eV in Figure 7.2.4 using the C++ code provided in Appendix 1 under the assumption that band-gap collapse occurs when the excited state population density exceeds on the order of 10^{22} cm^{-3}. Equation 4.1.1 is shown again below for reference:

$$\varepsilon = 1 + [\varepsilon_g(\hbar\omega + \Delta E_{gap}) - 1] * Ng - \omega_p^2/(\omega(\omega+i\Gamma)$$

(Equation 4.1.1)

where ε_g is the ground state dielectric function [Palik, 1985], ΔE_{gap} is a term for band-gap renormalization, Ng is the fraction of valence electrons in the ground state, ω_p is the plasma frequency, and Γ is the electron collision frequency. The real part of the excited GaAs dielectric function was calculated at -16.6 F/m for the 1064 nm (1.17 eV) light, which leads to an SPP wavelength of 1030 nm or 96.8% of λ_{laser}. This leads to a grating coupled wavelength of 515 nm and a predicted bifurcation wavelength of 258 nm. Our predicted period is consistent with the measured central wavelength in Figure 7.2.1b.

The real part of the excited GaAs dielectric function remains positive for irradiation with 390 nm (3.18 eV) light even at fluences that initiate band-gap collapse. Under these conditions, SPP coupling cannot occur so the initial islands cannot organize perpendicular to the laser polarization and HSFL never form. Without an SPP, Fresnel diffraction becomes the strongest

contributor to periodic variations in the laser energy coupled into the semiconductor surface [Murphy, 2013]. In the near field, the diffraction is strongest in the direction where the lines of island edges can act similar to an antenna [Born, 1959], which forms the LIPSS with long axis parallel to the laser polarization observed in Figure 7.2.3d.

Frequency doubling the 780 nm (1.59 eV) beam not only reduces the threshold for band-gap collapse due to stronger linear absorption, but also greatly reduces the fraction of the melt threshold and consequently the percentage of excited valance electrons required for point defect generation. To investigate the possibility that absorption of the 390 nm (3.18 eV) photons excites electrons that more strongly contribute to the interatomic binding potential, a quasi-nonadiobatic quantum molecular dynamics calculation, similar to the one described in Abere, 2015, shows that frequency doubling the beam enhances the probability of point defect formation above the band-gap collapse threshold [Torralva, private conversations].

In summary, changing the irradiation wavelength can controllably change the HSFL wavelength depending on the SPP response. Selecting a wavelength for which there is no SPP response will prevent the initial islands from evolving into HSFL and instead lead to parallel LIPSS at the laser wavelength. More strongly absorbing wavelengths also increase the efficiency of bond softening and enhance the ultrafast point defect generation mechanism.

References

C.B. Schaffer, A. Brodeur, and E. Mazur, *Meas. Sci. Technol.* **12**, 1784 (2001).

R.R. Gattass and E. Mazur, *Nat. Photonics.* **2**, 219 (2008).

M.R. Brozel and G.E. Stillman, *Properties of Gallium Arsenide*, INSPEC, London, England, 981 (1996).

1. X. Liu, D. Du, and G. Mourou, IEEE J. Quantum Elect. **33**, 1706 (1997).

U. Blieske, T. Kampschulte, A. Bauknecht, M. Saad, J. Sollner, A. Krost, K. Schatke, and M. Ch Lux-Steiner, 26th PVSC, 939 (1997).

J.A. Yater, G.A. Landis, S.G. Bailey, L.C. Olsen, and F.W. Addis, 26th PVSC, 65 (1996).

T.L. Chu, S.S. Chu, Solid State Electron. **38**, 535 (1995).

W. Wang, J. D. Phillips, S. J. Kim and X. Pan, *J. Electron. Mater.* **40**, 1674 (2011).

X. Wang, T. Jia, X. Li, C. Li, D. Feng, S. Xu, and Z. Xu, Chinese Opt. Lett. **3**, 615 (2005).

L.V. Keldysh, *Zh. Eksp. Teor. Fiz.* **47** 1945 (1964).

D.T.F. Marple, *J. Appl. Phys.* **35**, 1879 (1964).

S. Adachi, T. Taguchi, Phys. Rev. B. **43**, 9569 (1991).

J.P. McDonald, V.R. Mistry, K.E. Ray, and S.M. Yalisove, Appl. Phys. Lett. **88**, 153121 (2006).

J.R. Serrano, D.G. Cahill, J. Appl. Phys. **92**, 7606 (2002).

D.H. Reitze, T.R. Wood, and M.C. Downer, J. Opt. Soc. Am. **7,** 84 (1990).

C.S. Wang and B.M. Klein, *Phys. Rev. B.* **24**, 3393 (1981).

S.H. Lin, A.A. Villaeys, and Y. Fujimura, *Advances in Multi-photon Processes and Spectroscopy.* **16**, 249 (2004).

M.V. Ammosov, N.B. Delone, and V.P. Krainov, *Sov. Phys. JETP.* **64**, 1191 (1986).

F. Yan-Zhou, Z. Song-Feng, and Z. Xiao-Xin, *Chin. Phys. B.* **21**, 113101 (2012).

MJ. Abere, C. Chen, DR. Rittman, JD. Phillips, B. Torralva, and SM. Yalisove, *Appl. Phys. Lett.* **105**, 163103 (2014).

A. Boroweic and H.K. Haugen, *Appl. Phys. Lett.* **82**, 4462 (2003).

J. Bonse, J. Kruger, S. Hohm, and A. Rosenfeld, *J. Laser App.* **24**, 042006 (2012).

L. Huang, *Thesis.* (1997).

K. Sokolowski-Tinten and D. Von der Linde, *Phys. Rev. B.* **61**, 2643 (2000).

E. D. Palik, in Handbook of Optical Constants of Solids, edited by E.D.Palik (Academic, New York, (1985).

R.D. Murphy, B. Torralva, and S.M. Yalisove, *Appl. Phys. Lett.* **102,** 211101 (2013).

M. Born and E. Wolf, *Principles of Optics.* (1959).

Chapter 8

Summary and Future Work

Determine the mechanism responsible for ultrafast point defect generation and the defects' diffusional properties long after irradiation by:

1. determining the origin of laser induced nanodots
2. determining the diffusional component of high spatial frequency laser induced periodic surface structure formation

It was found that the nanostructures formed within a range of fluences that corresponded to the region between band-gap collapse and ultrafast-melting. These fluences represent the range in which softened bonds from electron excitation allows for an ultrafast formation of point defects. Strain relaxation via diffusing self-interstitial atoms redistribute mass above the initial surface and are the origin for both nanodots or HSFL. In addition, we suggest that the softened binding potential during band-gap collapse enhances mobility, which leads to both preferential defect generation rate and mass transport where the intense laser pulse is absorbed.

This thesis sought to establish the role of surface plasmon polaritons on nanostructures formed by the diffusion of laser induced point defects by:

1. developing a complete model for the formation of high spatial frequency laser induced periodic surface structures.
2. gaining size and shape control over nanostructures formed via laser induced point defect diffusion

Our results show that HSFL form when SPPs can couple to surface nanostructures to locally enhance the defect generation rate and mobility. The interplay between SPP coupling and continued strain relaxation of the newly generated point defects causes the surface to evolve through two transient populations with different wavelengths en route to HSFL formation. For GaAs under ambient conditions, the first transient LIPSS have a 165 nm period. This period arises due to the interaction between island coarsening, pit nucleation, and SPP coupling. Increasing the island size and spacing enhances the local absorbed intensity within the structure sidewalls, which locally increases both the defect generation rate and mobility. When the vacancies become mobile enough to nucleate pits, the islands become pinned at their existing separation distance as SPP coupling is only enhanced by increasing island height. The aligned pits and islands form the first 165 nm LIPSS. As the 165 nm LIPSS increase in height, the SPP couples to the upper branch of the SP-photonic band gap dispersion curve. Coupling on the SP-photonic band gap dispersion curve then becomes favored at the band-edge, which leads to the nucleation of a 355 nm LIPSS population. Continued point defect generation within these 355 nm LIPSS increases strain on the lattice, which is relieved through bifurcation. By controlling dose, we can stop the HSFL evolution at any of these intermediate populations, which allows for size control at a single wavelength.

Finally, this thesis sought to investigate the wavelength dependence of ultrafast laser materials interactions by:

1. investigating the effects of exciting specific inter-band transitions during ultrafast point defect generation
2. gaining wavelength control over high spatial frequency laser induced periodic surface structures

Changing the laser wavelength allows for the excitation of unique inter-band transitions. For GaAs, frequency doubling a 780 nm beam excites valance electrons more closely associated with bonding, which allows for band-gap collapse at a lower concentrations of non-equilibrium carriers. Highly absorbing wavelengths also allow for band-gap collapse without generating a dense enough electron-hole plasma to make the semiconductor metallic. Under these conditions the SPPs cannot couple and islands continued to grow uncorrelated to the electric field, forming stoichiometric semiconductor nanodots on the surface. Finally, increasing the laser wavelength causes a similar redshift in the HSFL period that scales proportionally with the SPP wavelength.

8.1 Dynamics of defect formation and digital diffusion

Thus far, this thesis has characterized HSFL formation using post-mortem techniques. Future work should focus on understanding the dynamics of defect diffusion during HSFL formation. Figure 8.1 shows that the transition between the 165 nm and 355 nm LIPSS is easily differentiated with our in-house optical microscope. It is possible to extend the currently available optical pump-probe imaging system [Schrider, 2015] beyond the nanosecond timescale by incorporating a diode triggering system for the probe beam, which would allow for characterization of the kinetics of this transition. However, this technique has its limits as it does not detect the island nucleation for early evolution processes and cannot differentiate between the 355 nm and 180 nm HSFL. The existing in house optical microscope is still useful for determining the stage of HSFL evolution in-situ. This is important for characterizing the

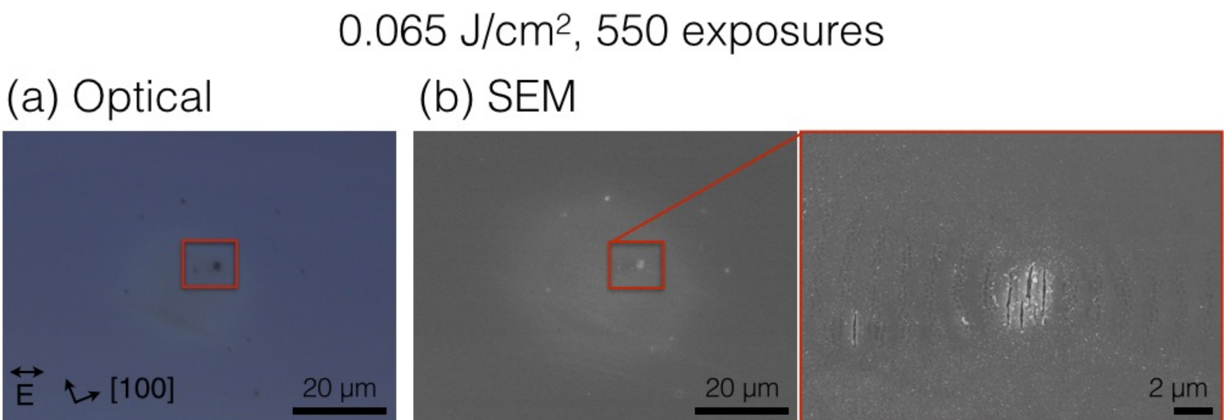

Figure 8.1: (a) Optical and (b) corresponding SEM images of the same laser spot showing that the dark optical contrast corresponds to the nucleation of the 355 nm LIPSS population in GaAs.

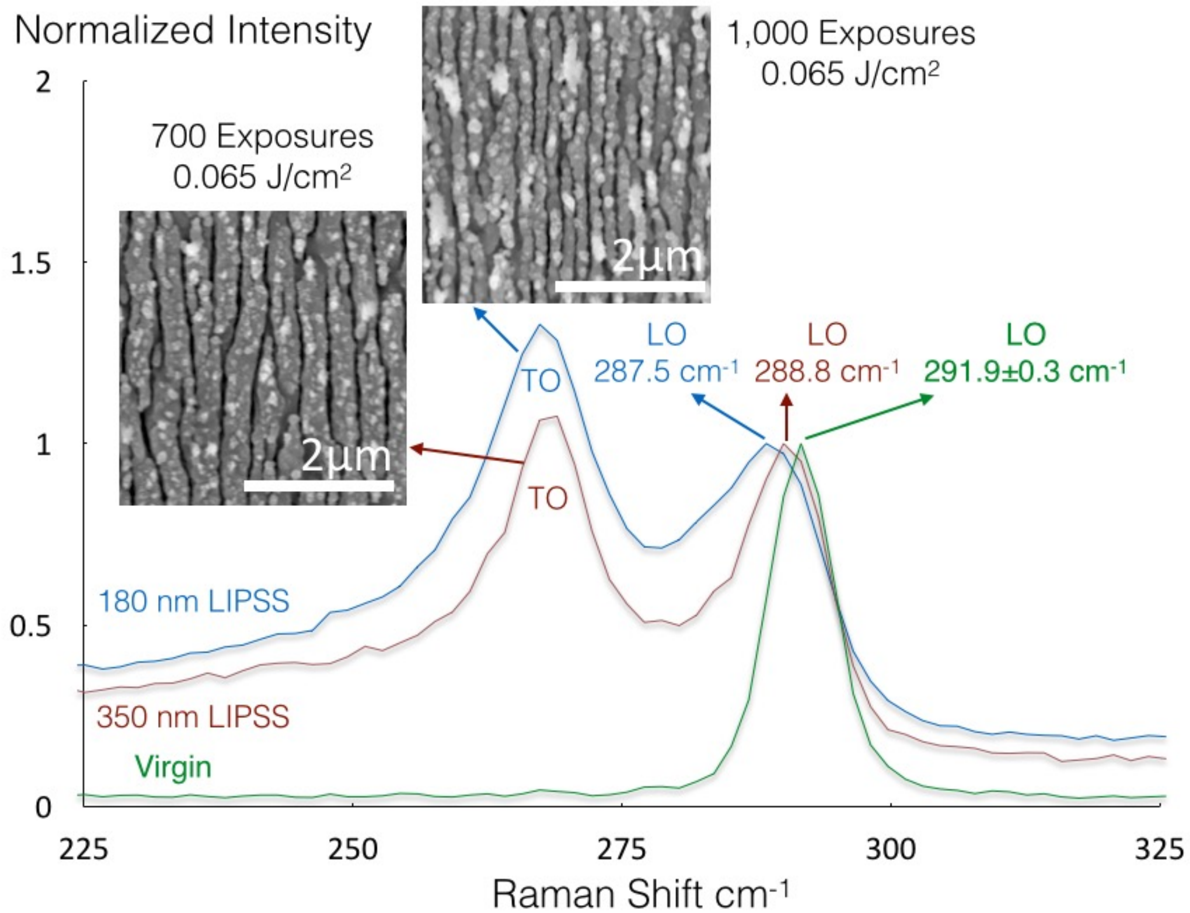

Figure 4.3.5 Raman spectroscopy from LIPSS in HSFL. The corrugation creates (111) surface making the transverse optical mode appear. A redshift and broadening of the longitudinal optical mode with increasing exposures occurs due to the formation of the wurtzite-like phase shown in Figure 4.3.4

dynamics of the 355 nm LIPSS formation because we can then consistently evolve the system right up to the edge of its nucleation before measuring a specific delay time.

To characterize the dynamics of HSFL formation, this thesis suggests building a pump-probe Raman microscope. This thesis showed in Chapter 4 that the nucleation of the 355 nm LIPSS is accompanied by the appearance of the transverse optical phonon mode and that the relative intensity increases by a factor of two during bifurcation. The nucleation of both the 355 and 180 nm HSFL can be observed by using a diode triggered laser as a Raman probe. Figure

4.3.5 is reprinted below for reference to show the dependence of the transverse and longitudinal optical modes in the Raman spectrum on HSFL evolution. Furthermore, monitoring the peak

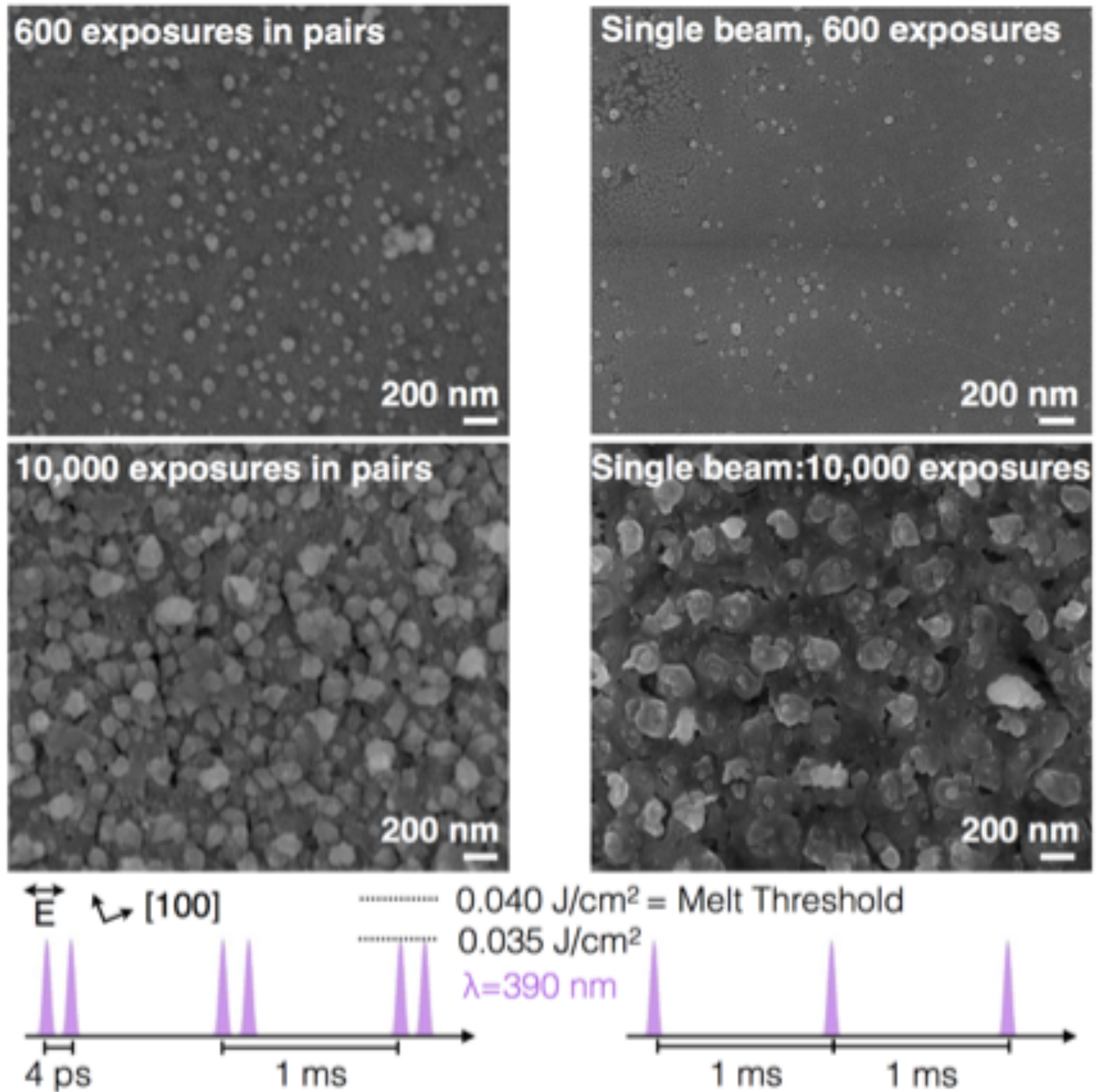

Figure 8.2: SEM images of island distributions formed by repeated irradiation with 390 nm femtosecond pulses below the melt threshold but above the band-gap collapse threshold. There is no evidence of SPP formation in either case.

position of the longitudinal optical phonon mode allows for the study of the dynamics of the phase transformation into the wurtzite-like phase observed in STEM.

8.2 Interaction with a laser excited material during band-gap collapse

This thesis has primarily focussed on GaAs irradiation with a 780 nm laser wavelength because band-gap collapse is well characterized for these irradiation conditions. In order to better understand our results with the frequency doubled beam, this thesis suggests repeating the experiments by Glezer and Mazur [Glezer, 1995] with the frequency doubled beam as well as expanding the characterized time beyond 8 ps to determine the duration of bond softening. With this understanding, it is possible to explore how band-gap collapse, defect generation, and SPP coupling are affected when softened bonds interact with a second excitation. This can be achieved by temporally pulse shaping the beam in order to tailor the dielectric properties of the semiconductor that the laser interacts with when initiating the defect generation process.

Preliminary results show that temporally pulse shaping the beam to interact with a modified dielectric function produces unique surface morphologies. Figure 8.2 shows that temporally shaping the beam to have two peaks 4 ps apart changes the island distribution for irradiation with 390 nm light. These results also suggest that a combination of wavelengths can be used to form new unique nanostructures. For instance, defect generation could be initiated with a 390 nm beam while supplying the SPP with 780 nm light. This could lead to control over

the defect generation rate during HSFL formation as well as the ability to initiate formation from a radically different distribution of islands. Figure 8.3 shows that the same shaped pulse produces a unique parallel LIPSS population in Si with period more than twice the laser wavelength. These structures have never before been observed and show that we can radically change surface morphology by interacting with the softened bonding potential.

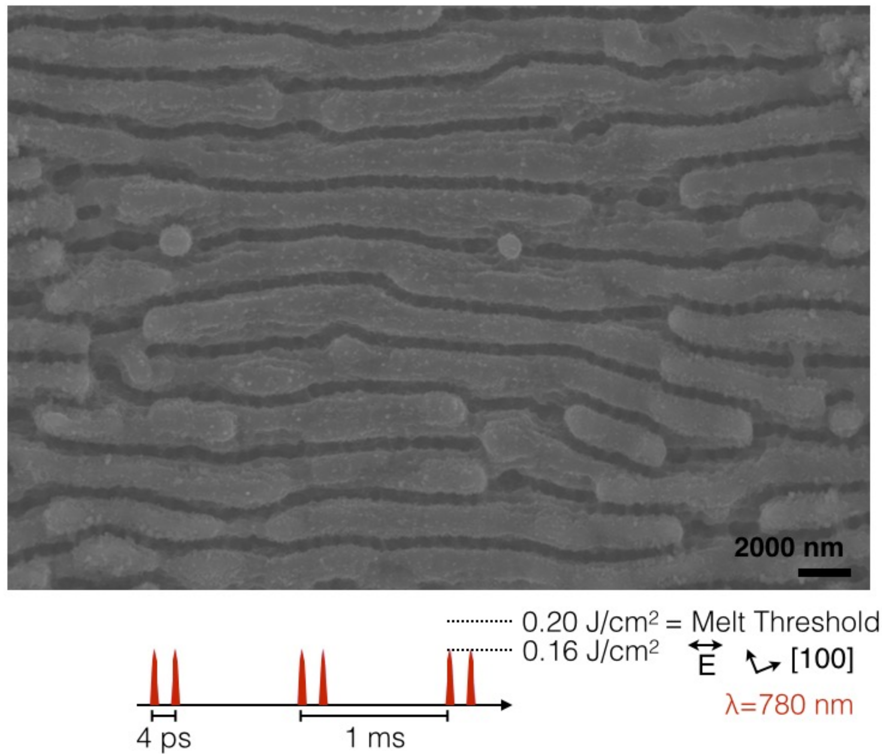

Figure 8.3: Parallel LIPSS formed in Si with period more than two times the laser wavelength after temporal pulse shaping of the beam

8.3 Characterization of Ultrafast Laser Generated Point Defects

This thesis connected the formation of HSFL to ultrafast laser generated point defects and developed a model for their formation. Though quantum molecular dynamics simulations predict that the laser generated point defects are vacancy/interstitial pairs [Abere, submitted] and preliminary studies were performed regarding lifetime within this thesis, much can still be done to characterize the defects.

To further study the ultrafast laser generated defects, this thesis suggests moving to a system in which interstitials are known to remain stable at room temperature long enough for ex-situ characterization in TEM. Interstitials in Si precipitate on {311} planes and form monolayers of hexagonal Si [Eaglesham, 1994]. By imaging the strain from the {311} defects in weak beam dark field TEM, it is also possible to determine the defect density. The ability to directly observe interstitials and their concentration within the semiconductor opens up the possibility for dynamics studies of the defect diffusion at the atomic scale by integrating an ultrafast laser into a dynamic TEM. This would allow for the direct characterization of how strain at a given defect concentration is released to change the semiconductor surface morphology.

The first step toward defect characterization is to reproduce HSFL formation in Si. The HSFL do not form from irradiation at 1 kHz [Bonse, 2009; Costache, 2004; Bonse, 2012], but have been observed after irradiation with an 80 mHz laser [Le Harzic, 2011]. The higher repetition rate allows for the next pulse to soften the bonds faster than the interstitials generated on the previous pulse can annihilate with a vacancy. Preliminary experiments are underway to reproduce the results shown by Le Harzic *et al.* using a 50 mHz laser. Beyond forming HSFL in

Si, this thesis suggests performing repetition rate studies in order to determine the defect lifetime at a concentration capable of causing morphological changes in Si.

8.4 Temperature and atmosphere control during high spatial frequency laser induced periodic surface structure formation

Both the defect generation rate and diffusion rates are a function of the semiconductor temperature. Changing temperature therefore offers another knob for controlling defect/diffusion formed nanostructures in semiconductors. However, heating or cooling the substrate can lead to changes in semiconductor surface chemistry. Heating leads to oxidation of the surface while cooling causes condensation of water or liquid oxygen depending on the temperature. Both of these factors have made preliminary studies difficult to interpret. Thus, this thesis suggests moving the temperature based experiments into an inert atmosphere.

This thesis suggests first using the existing vacuum chamber that can attach directly onto our translation stage that can reach pressures of 10^{-2} mtorr or flow a carrier gas such as nitrogen. This chamber can be modified to include a thermocouple and heating element in order to perform these experiments. However, the existing chamber is limited in size, weight, and vacuum pressure because it is designed to operate suspended from a four axis translation stage. It may therefore be necessary to perform more extensive heating, cooling, and atmosphere controlled experiments after refurbishing the ultra high vacuum (UHV)-Si molecular beam epitaxy chamber.

Working in an inert atmosphere also allows for the exploration of the role of the native oxide on HSFL formation. This oxide has a thickness on the order of the island height at nucleation. It should be determined whether the native oxide is removed after each exposure and interstitials diffuse to the surface before it reforms or if the interstitials diffuse to the GaAs/oxide interface during formation. GaAs has a Ga_2O_3 native oxide, which can be etched away with any of HCl, H_2SO_4, or H_3PO_4. Chemical etching followed by gentle heating within our existing UHV system was previously used to keep the surface atomically clean for at least four hours during studies that showed that the material removal threshold in Si was 30% lower without the native oxide [McDonald, 2005].

The work presented in this thesis focuses on HSFL formation in semiconductors. However, periodic structures with a similar length scale are also observed in metals such as Cu and Ti [Bonse, 2012]. Working with atomically clean surfaces allows for the determination of whether the HSFL formed in metals arise due to defect generation in a semiconducting oxide, at the metal/semiconductor interface, directly within the metal, or by a different mechanism.

8.5 Production of a broad-band detector

Modifying semiconductor surface topography is a common method for enhancing light absorption within various optoelectronic applications such as sensors for power monitoring or video detection. Making detectors that respond in low light environments have many applications ranging from military drones, to self-driving cars, to in-vivo medical imaging. Many surface patterning techniques do not retain the semiconductor's original crystal structure, which

leads to efficiency losses within devices through scattering. Hence, there is need for surface processing methods that can largely retain a single crystal structure within the patterned region.

Patterning a surface with HSFL changes the surface topography while largely retaining the original crystal structure. A provisional patent was recently filed for this technique and future work will focus on building a prototype detector. Although the surfaces appear optically black, the HSFL patterned surface should be characterized across multiple wavelengths with absorption spectroscopy as well as conductivity measurements to determine device efficiency. There are several ways in which to optimize device efficiency. This thesis suggests eliminating the nanocrystalline regions at the structure tops and trench bottoms either through etching or annealing. Furthermore, HSFL may not be the ideal shape for maximizing absorption as they only increase surface area in one direction. The shape of ultrafast laser generated defect/diffusion based nanostructures can be controlled by using alternate laser polarizations [Reif, 2009]. As long as the defect/diffusion based nanostructures formed with elliptical and circular polarization retain their original crystal structure and orientation, we may be able to optimize structure shape for making a detector.

8.6 Doping with exotic elements

With an understanding of the physical mechanisms responsible for HSFL formation in semiconductors, future work should look to exploit them. The enhanced mobility from defect generation and bond softening might be useful for doping semiconductors with exotic materials. This thesis suggests exploring the feasibility of utilizing the ultrafast laser generated point

defects to dope semiconductors by irradiating semiconductors in the presence of carrier gasses. For these applications, it would be ideal to form defects without causing HSFL formation in order to maintain a surface suitable for electrical contacts. Ultrafast laser based doping above the ablation threshold show that the ability to introduce dopants into a semiconductor requires a minimum adsorption rate controlled by the gas partial pressure and doping only occurred when alongside morphological changes [Crouch, 2004]. It is also important to choose a system where the defect lifetime is long relative to the rate of diffusion. For this reason GaAs remains a good candidate for defect-diffusion based ultrafast laser doping. Future work will seek to optimize the fluence, number of exposures, repetition rate, laser wavelength, and gas pressure, which determines adsorption rate in order to explore the potential for defect-diffusion based ultrafast laser doping of semiconductors.

References

K.J. Schrider, B. Torralva, and S.M. Yalisove, *Appl. Phys. Lett.* Submitted (2015).

EN Glezer, Y. Siegal, L. Huang, and E. Mazur, *Phys. Rev. B.* **51**, 6959 (1995).

MJ Abere, B. Torralva, and S.M. Yalisove, *Science,* submitted

D.J. Eaglesham, P.A. Stolk, H.J. Grossman, J.M. Poate, *Appl. Phys. Lett.* **65**, 2305 (1994).

J. Bonse, A. Rosenfeld, and J. Kruger, *J. Appl. Phys.* **106**, 104910 (2009).

F. Costache, S. Kouteva-Arguir, and J. Reif, *Appl. Phys. A.* **79**, 1429 (2004).

J. Bonse, J. Kruger, S. Hohm, and A. Rosenfeld, *J. Laser App.* **24**, 042006 (2012).

J.P. McDonald, AA. McClelland, YN. Picard, SM. Yalisove, *Appl. Phys. Lett.* 86(26), 264103, (2005).

J. Reif, F. Costache, O. Varlamova, G. Jia, and M. Ratzke, *Physica Status Solidi C.* **6,** 681 (2009).

C.H. Crouch, J.E. Carey, M. Shen, E. Mazur, and F.Y. Genin, *Appl. Phys. A.* **79**, 1635 (2004).

Appendix 1

Dielectric Function Code

This C++ code calculates the excited dielectric function for GaAs in order to determine the SPP wavelength. It also will calculate the time dependent ground state dielectric function during band-gap collapse by fitting reflectivity data to a two oscillator model.

```
//
//  main.cpp
//  GaAs Excited Dielectric Function
//
//  Created by Michael Abere on 3/4/15.
//  Copyright (c) 2015 Michael Abere. All rights reserved.
//

#include <iostream>
#include <cmath>
#include <complex>
#include <fstream>

using namespace std;

int main(int argc, const char * argv[])
{
    complex<double>  Epsilon_wX, Epsilon_wY, A_oscillator, B_oscillator, drude, eg;
    complex<double> Ry, Ry1, Exc, gx, hx, dExc, deltaEg, omegaX;
    //double hbar = 6.582e-16;
    double one = 1, wp = 13.7;
    double wp1, ne = 0, e = 1.602e-19, rs, rs1; //Excitation
    double omega1 = 3.1, omega2 = 4.75, gamma1 = 0.68, gamma2 = 1.60; //Time zero
    //double omega1 = 2.85, omega2 = 3.95, gamma1 = 1.2, gamma2 = 6.5; //Time 130 fs
    //double omegaX = 2.2, omegaY =4.4, omega1 = 2.1, omega2 = 3.8, gamma1 = 0, gamma2 =
0; // 130 fs start
    complex<double> i = {0,1};
    double f = 0.16;
```

```
    ofstream myfile;
    myfile.open("solver.txt");

    if (myfile.fail()){
        cout << "Error opening" << endl;
        return 1;
    }




    /*for (int l = 0; l < 20; l++){
        omega2 = 3.8;

        for (int m = 0; m < 20; m++){
            gamma1 = 0;

            for (int n = 0; n < 25; n++){
                gamma2 = 0;

                for (int o = 0; o < 25; o++){
                    A_oscillator = f / (omega1 * omega1 - omegaX * omegaX + i * omegaX *
gamma1);
                    B_oscillator = (1-f) / (omega2 * omega2 - omegaX * omegaX + i * omegaX *
gamma2);
                    Epsilon_wX = one + wp * wp * (A_oscillator + B_oscillator);


                    A_oscillator = f / (omega1 * omega1 - omegaY * omegaY + (i * omegaX *
gamma1));
                    B_oscillator = (1-f) / (omega2 * omega2 - omegaY * omegaY + (i * omegaX *
gamma2));
                    Epsilon_wY = one + wp * wp * (A_oscillator + B_oscillator);

                    myfile << omega1 << " " << omega2  << " " << gamma1 << " " << gamma2 << " "
<< omegaX << " " << Epsilon_wX.real() << " " << -Epsilon_wX.imag() << " " << omegaY << "
" << Epsilon_wY.real() << " " << -Epsilon_wY.imag() << endl;

                    gamma2 = gamma2 + 0.5;
                }

                gamma1 = gamma1 + 0.05;
            }
```

```
            omega2 = omega2 + 0.05;

        }
        omega1 = omega1 + 0.05;
        cout << "progress = " << (omega1 - 2.1) * 100 << "/100" << endl;

    }*/

    ne = 1.77e22;
    for (int j = 0; j < 601; j++){
        A_oscillator = f / (omega1 * omega1 - omegaX * omegaX + i * omegaX * gamma1);
        B_oscillator = (1-f) / (omega2 * omega2 - omegaX * omegaX + i * omegaX * gamma2);
        Epsilon_wX = one + wp * wp * (A_oscillator + B_oscillator);


        wp1 = sqrt(ne * 4.75e4 * 1e6) * 6.582e-16;
        drude = wp1/(omegaX * (omegaX + i * 1e-15));
        //Epsilon_wY = one + (conj(Epsilon_wX) * (omegaX - 1.424) - one) * (1.77e23 - ne)/
1.77e23 - drude;
        Epsilon_wY = one - drude;


        //A_oscillator = f / (omega1 * omega1 - omegaY * omegaY + (i * omegaX * gamma1));
        //B_oscillator = (1-f) / (omega2 * omega2 - omegaY * omegaY + (i * omegaX * gamma2));
        //Epsilon_wY = one + wp * wp * (A_oscillator + B_oscillator);

        //cout << omegaX << " " << A_oscillator << " " << B_oscillator << endl;
        cout << omegaX.real() << " " << Epsilon_wY.real() << " " << Epsilon_wY.imag()<< endl;
        //" " << Epsilon_wY.real() << " " << Epsilon_wY.imag()<< endl;

        omegaX = 0.01 + omegaX;
        }

    /*omegaX = 1.5895;
    eg = 12.8 + 1.4925*i;
    for (int j = 0; j < 5001; j++){

        wp1 = sqrt(ne * 4.75e4 * 1e6) * 6.582e-16;
        drude = wp1/(omegaX * (omegaX + i * 1e-15));
        Epsilon_wX = one + (eg * (omegaX - 1.424) - one) * (1.77e23 - ne)/1.77e23 - drude;
        //cout << ne/1e6 << " " << rs << " " << Ry1 << endl;
        cout << ne << " " << " " << Epsilon_wX.real() << " " << Epsilon_wX.imag()<< endl;
```

```
        ne = ne + 1e20;
    }*/

    myfile.close();

    return 0;
}
```

Appendix 2

Pair Correlation Code

This C++ code calculates the pair correlation function from an AFM image assuming periodic boundary conditions.

```
//
//  main.cpp
//  Pair Correlation Function
//
//  Created by Michael Abere on 6/25/15.
//  Copyright (c) 2015 Michael Abere. All rights reserved.
//

#include <iostream>
#include <cmath>
#include <fstream>
#include <cstdlib>



using namespace std;


//These two functions are for making a sorted list but Excel is faster
void print_array(double array[], int size) {
    //cout<< "buble sort steps: ";
    int j;
    for (j=0; j<size-1;j++)

        cout <<" "<< array[j] << endl;
}//end of print_array

void bubble_sort(double arr[], int size) {
    bool not_sorted = true;
    int j=1,tmp;
```

```
    while (not_sorted)  {
        not_sorted = false;
        j++;
        for (int i = 0; i < size - j; i++) {
            if (arr[i] > arr[i + 1]) {
                tmp = arr[i];
                arr[i] = arr[i + 1];
                arr[i + 1] = tmp;
                not_sorted = true;

            }//end of if
            //print_array(arr,23); //input size of array
        }//end of for loop
    }//end of while loop
    print_array(arr,977032); //input size of array
}//end of bubble_sort


int main(int argc, const char * argv[]) {

    int length = 1311;



    ifstream myfile1;
    ifstream myfile2;
    myfile1.open("xdata.txt");
    myfile2.open("ydata.txt");
    long k = 0, q = 0;
    int n = 0;
    double x, y;
    double x_input[1311] = {}, y_input[1311] = {}, output[1000000] = {}; //need to manually add
lengths
    double x_ninegrid[11799] = {}, y_ninegrid[11799] = {}; //need to manually add length
    double distance;
    //myfile >> x;
    //cout << x << endl;

    if (myfile1.fail()){
        cout << "Error opening x data" << endl;
        return 1;
    }

    if (myfile2.fail()){
```

```
    cout << "Error opening y data" << endl;
    return 1;
}

//This loop inputs shit into an x and y vector
for (int i=0; i<length; i++){
    myfile1 >> x;
    myfile2 >> y;
    x_input[i] = x;
    y_input[i] = y;
    //cout << x_input[i] << " " << y_input[i] << endl; //check to see if input file is functioning
}

for (int asdf1 = 0; asdf1 < length; asdf1++){
    x_ninegrid[q] = x_input[asdf1] - 5000;
    y_ninegrid[q] = y_input[asdf1] - 5000;
    //cout << x_ninegrid[q] << " " << y_ninegrid[q] << endl;
    q = q + 1;
}
for (int asdf2 = 0; asdf2 < length; asdf2++){
    x_ninegrid[q] = x_input[asdf2];
    y_ninegrid[q] = y_input[asdf2] - 5000;
    //cout << x_ninegrid[q] << " " << y_ninegrid[q] << endl;
    q = q + 1;
}
for (int asdf3 = 0; asdf3 < length; asdf3++){
    x_ninegrid[q] = x_input[asdf3] + 5000;
    y_ninegrid[q] = y_input[asdf3] - 5000;
    //cout << x_ninegrid[q] << " " << y_ninegrid[q] << endl;
    q = q + 1;
}
for (int asdf4 = 0; asdf4 < length; asdf4++){
    x_ninegrid[q] = x_input[asdf4] - 5000;
    y_ninegrid[q] = y_input[asdf4];
    //cout << x_ninegrid[q] << " " << y_ninegrid[q] << endl;
    q = q + 1;
}
for (int asdf5 = 0; asdf5 < length; asdf5++){
    x_ninegrid[q] = x_input[asdf5];
    y_ninegrid[q] = y_input[asdf5];
    //cout << x_ninegrid[q] << " " << y_ninegrid[q] << endl;
    q = q + 1;
}
```

```
    for (int asdf6 = 0; asdf6 < length; asdf6++){
        x_ninegrid[q] = x_input[asdf6] + 5000;
        y_ninegrid[q] = y_input[asdf6];
        //cout << x_ninegrid[q] << " " << y_ninegrid[q] << endl;
        q = q + 1;
    }
    for (int asdf7 = 0; asdf7 < length; asdf7++){
        x_ninegrid[q] = x_input[asdf7] - 5000;
        y_ninegrid[q] = y_input[asdf7] + 5000;
        //cout << x_ninegrid[q] << " " << y_ninegrid[q] << endl;
        q = q + 1;
    }
    for (int asdf8 = 0; asdf8 < length; asdf8++){
        x_ninegrid[q] = x_input[asdf8];
        y_ninegrid[q] = y_input[asdf8] + 5000;
        //cout << x_ninegrid[q] << " " << y_ninegrid[q] << endl;
        q = q + 1;
    }
    for (int asdf9 = 0; asdf9 < length; asdf9++){
        x_ninegrid[q] = x_input[asdf9] + 5000;
        y_ninegrid[q] = y_input[asdf9] + 5000;
        //cout << x_ninegrid[q] << " " << y_ninegrid[q] << endl;
        q = q + 1;
    }

    for (int m=0; m<length; m++){


        for (int j=0; j< 9*length; j++){
            distance = sqrt((x_input[m]-x_ninegrid[j])*(x_input[m]-x_ninegrid[j]) + (y_input[m]-
y_ninegrid[j])*(y_input[m]-y_ninegrid[j]));

                //cout << distance << endl; //check to see if distance is calculating

            if (distance == 0){
                distance = 5000;
            }
            if (abs(y_input[m] - y_ninegrid[j]) > 30){
                distance = 5000;
            }
            if (distance < 1455){
                //cout << "if statement distance is: " << distance << endl;
              output[k] = distance;
```

```
            cout << "m= " << m << " k= " << k << " stored " << output[k] << endl; //check to see if
outputing correctly

              //cout << output[k] << endl;
            k = k + 1;
          }


      }
      n = n + 1;
      //cout << "m is now " << m << endl;
   }

   //print_array(output,23);
   //bubble_sort(output, 977032);


   myfile1.close();
   myfile2.close();

   return 0;
}
```

Appendix 3

Calibrating the Ultrafast Laser with the Si Threshold

The ablation threshold of Si is used to calibrate the laser each day before running any experiments. This is because the experiment can be performed quickly and is sensitive to changes in pulse quality that are not detectable by simply maximizing the laser output power, the oscilloscope resolution when measuring the pulse train, or an intensity autocorrelator.

A diagram of the experimental setup used for standard system calibration is provided in Figure A3.1. The laser beam was aligned along the optics table by using two pinholes and two mirrors. Any change to pinhole placement was performed by manually aligning the beam to the screw holes along the table and to a fiducial mark on a fluorescent card for height. Mirror 1 in Figure A3.1 is used to align the beam through pinhole 1 and mirror 2 aligns pinhole 2. One should check to make sure there isn't any dust on the mirrors by looking for dark spots within the beam on a fluorescent card after each mirror. If the mirrors are dirty, they can be cleaned by wiping them with methanol on a lens cleaning cloth.

The average power was measured in an Ophir Optics thermal power sensor, which was converted to an average pulse energy by dividing the measured power by the laser repetition rate. The laser energy was attenuated by rotating the polarization with a half-wave-plate and then rejecting the p-polarized beam with a beam splitting cube. One should not allow the laser dwell

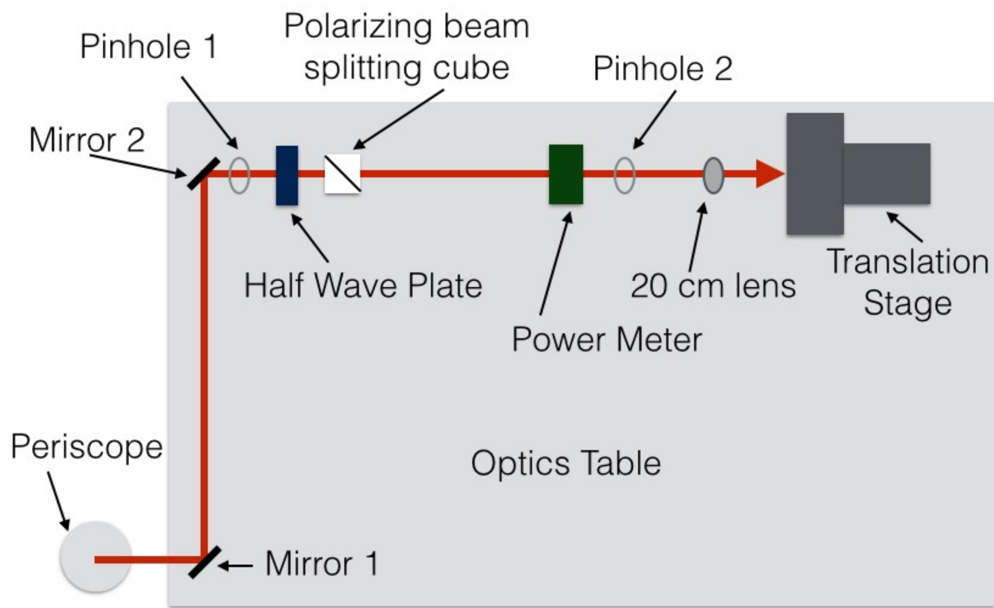

Figure A3.1 Configuration and relevant optics for laser calibration and threshold studies

with the wave-plate rotated to a minimum as this will eventually lead to damage of the cube. Additional attenuation was performed using neutral density filters.

The beam was focussed onto the sample at normal incidence with a plano-convex lens. Calibration experiments and those used to determine damage thresholds in new materials were performed with a 20 cm focal length lens because it produces damage spots with an average separation that is easy to image when the 4-axis translation stage in Figure A3.1 is rastered at its maximum 100 mm/s velocity. Experiments for high spatial frequency laser induced periodic surface structure (HSFL) formation were performed with a 100 cm focal length lens because the larger spot size reduces the contribution of power meter noise when choosing an irradiation fluence.

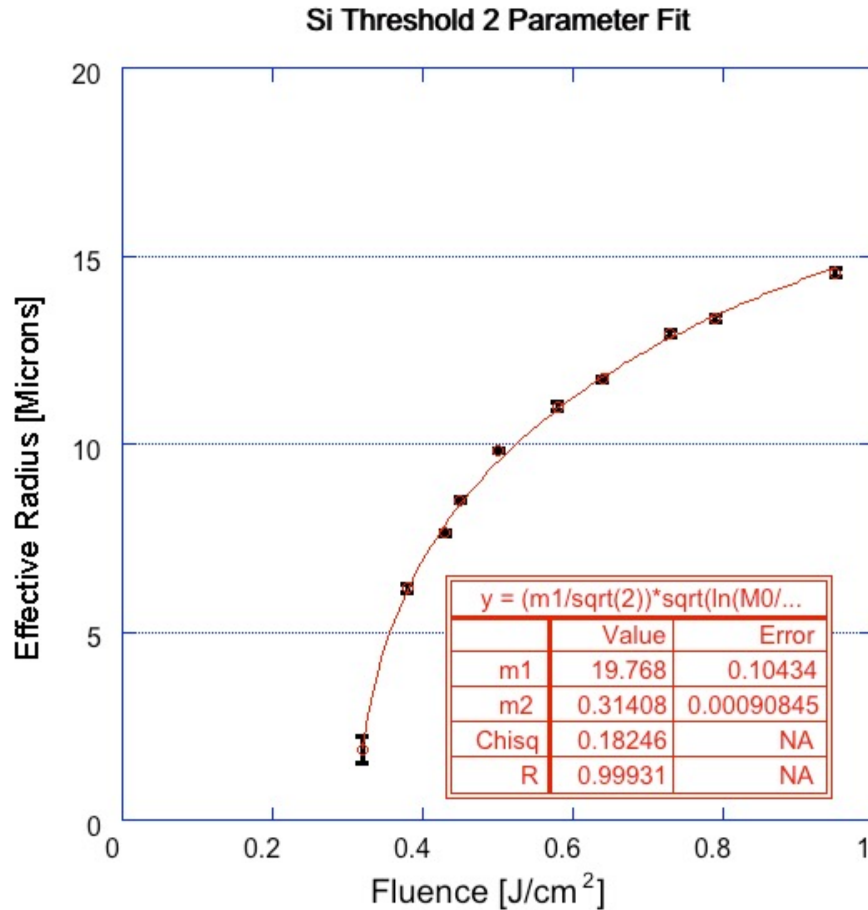

Figure A3.2 Direct output from the Kaleidograph plotting software used for calibration studies. m1 is an estimate of the beam radius and should be within 10% of the measured value from the beam profiler. m2 is the calculated threshold fluence. The plotted line should cross within the error bars for the physical measurements taken from the optical images in order for the fit to be considered

The focussed spot size was measured using a WinCam-D beam profiling CCD camera. The camera magnifies the focussed spot with a 20X objective such that the beam focussed with a 20 cm lens fills ~ 20% of the camera pixels. Coarse alignment into the camera is performed at 300 µW of average power so as not to damage the camera. The beam is attenuated as it is moved toward focus so as not to saturate the pixels. The maximum peak should be on the order of 80% of the maximum in order to get an accurate measurement of the spot size. The spot area was calculated by counting the number of pixels over 13.5% ($1/e^2$) of the spot center. The conversion

between pixel count and a physical length used the width of the imaged area as 235 μm. This value was calibrated by measuring the spot center translation with a known distance on the 4-axis stage and is consistent with the width reported in the WinCam D manual. While the spot size scales by the well known 1.22 fλ/d relationship for lenses longer than 20 cm, new profiles must be taken for focal lengths smaller than 20 cm. The equation $F = 2E_{total}/\pi A$ is used to calculate fluence where F is the peak fluence, E_{total} is the energy per pulse (equal to the average power over the repetition rate), and A is the area calculated from the beam profile.

Sample focus position was determined using a second CCD camera and then marking the position of the focussed spot with a micrometer. This method is consistent with spark testing and decidedly faster. One should note that the camera and micrometer do not fit into the space for lenses less than 10 cm so the spark test must be used. Performing a spark test requires that one finds the range at which a specific fluence produces a spark on a piece of Si. The beam is attenuated until the spark range is on the order of the Rayleigh length of the lens.

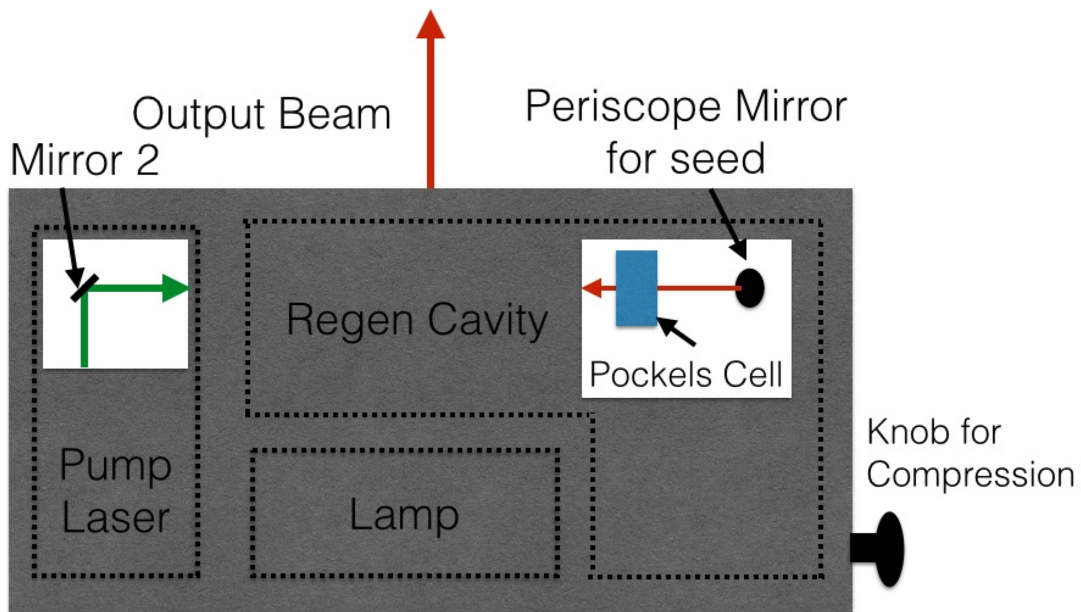

Figure A3.3 Layout of Clark MXR 2001 laser and relevant optics for day to day optimization

The Si threshold is performed by rastering the sample through the focussed beam to make lines of laser damage spots. The threshold is calculated by imaging the sample in optical microscopy and measuring the area of each spot. For statistical purposes, nine damage spots were measured for each fluence on a new material. From each area, an effective radius is calculated by taking the square root of the area over π. The relationship between fluence and effective radius is derived from Equation A3.1:

$$M_0 \cdot \exp(-2 \cdot r^2/m_1^2) = m_2 \quad \text{(Equation A3.1)}$$

$$r = (m_1/2^{1/2}) \cdot \ln(M_0/m_2)^{1/2} \quad \text{(Equation A3.2)}$$

where r is the effective damage spot radius, m_1 is the beam waist, M_0 is the peak fluence, and m_2 is the threshold fluence. The physical significance of Equation A3.1 is that the radius at which the local fluence is equal to the threshold fluence occurs at the edge of the crater. Equation A3.1 is transformed into Equation A3.2 to solve for the effective radius and then plotted with a two-parameter fit to determine the damage threshold. An example of this relationship is shown in Figure A3.2.

The acceptable threshold for Si is 0.32 ± 0.02 J/cm^2. This range is consistent with literature values [Bonse, 2002]. Only when these conditions for the Si threshold are met, the high spatial frequency laser induced periodic surface structures (HSFL) form in a repeatable manner. In cases where the threshold is already known, the process can be sped up to allow for parallel adjustments to the laser during maintenance. The calculated threshold is typically about 0.02 J/cm^2 below the last visible line. By setting the strongest neutral density filter on a wheel to the

corresponding power and then making one line per filter, one can simply check if all the lines appear on the sample with the microscope located next to the optics table.

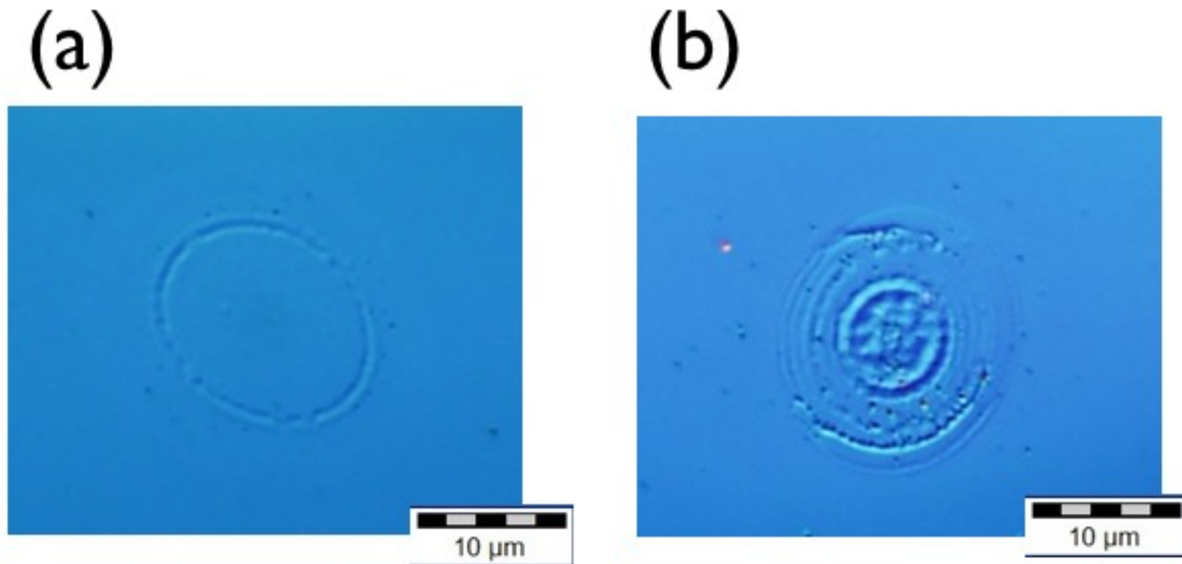

Figure A3.4 (a) Appropriate Si morphology near the damage threshold for all fluences < 0.6 J/cm^2. (b) Si damage morphology signifying that there is an issue with the laser. This particular morphology at 0.5 J/cm^2 came from a damaged Ti:sapphire crystal.

In the event that the Si threshold is not within the acceptable range, sample focus should first be checked. The resulting damage craters should spatially match the beam profile taken with the WinCamD CCD camera. The second easiest problem to solve is having a lens with the wrong anti-reflective coating in the line. The wrong coating will cause the reading in the power meter to

overstate the fluence incident on the sample surface. Furthermore, sending a frequency doubled beam through a borosilicate lens instead of one of the fused silica lenses will damage the optic.

If the optics are all properly functioning, then there is likely an issue with the laser itself. This will happen less frequently if a steady flow of nitrogen is kept passing through the laser. The Clark MXR is highly susceptible to changes in humidity, which frequently occur during the changing seasons in Michigan. The pulse compression should be roughly aligned by optimizing white light generation through a water beaker. This ensures that the pulses are at least 180 fs or shorter. Fine adjustments to compression can be made by minimizing the peak width in the intensity autocorrelator located on the optics table next to the laser. Next, the seed alignment should be optimized by adjusting the periscope mirror for the seed in Figure A3.3. Mirror 2 can then be used to optimize the green Nd:YAG pump laser through the Ti:Sapphire crystal. One should be especially careful when moving this mirror as it is possible to damage the Ti:Sapphire crystal if the green laser is clipping. As long as the pulse train does not disappear from the oscilloscope, the green laser is still going through the Ti:Sapphire.

The next step is to check for pre-pulses by placing the fast photo-diode into the scattered beam. The pre-pulse is the peak that changes if the Pockels Cell (labelled in Figure A3.3) is nudged. Small adjustments by pressing on the Pockels Cell should be made until the contrast between pre and main pulse are at least 1:1,000. If these changes are not sufficient to bring the Si threshold into specification, then the timing may need to be adjusted. Small adjustments to the timing can be made by adjusting the laser current. A good rule of thumb is that the pulse on the photo-diode should not be correlated to the rising pulses in the train. Next, the dump time should be adjusted to maximize power on the dumped pulse. If the threshold is still not within the

specified range, then a different seed pulse may be selected by shifting the injection timing. The new injection timing should be placed where the peak in the pulse train envelope has the least noise in the oscilloscope. If none of this works, then the lamp may have reached the end of its lifecycle and needs to be changed. If all else fails, service will need to be called.

In addition to the value of the threshold, the Si morphology can be used to diagnose issues with the laser. When the laser is working, the crater should have a flat bottom as shown in Figure A3.4a. If the crater has additional structure in it such as the morphology shown in Figure A3.4b, then the laser has either lost mode locking, is allowing two pulses through, or the prism is damaged. Service should be called to remedy these issues.

Appendix 4

Microscopy Long after Irradiation

The atom-scale, nano and microstructures of interest are all significantly smaller than a human's 40 μm optical detection limit. Therefore experiments must be characterized using various microscopy techniques. Characterization techniques using light, electron beams, and scanning probes will be detailed in this section.

A4.1 Optical Microscopy

Optical images were taken to obtain low magnification images of each damage spot. Images were taken on a combination of microscopes. The in-house microscope takes the highest quality dark field images and does not require walking across campus to operate. Scale bars for the different objectives on this scope are stored on the desktop of the lab computer.

Higher resolution optical images were taken in the wet chemistry room of the Lurie Nanofabrication Laboratory on an Olympus BX-51 microscope located in the Electrical Engineering and Computer Science building on North Campus. The microscope has brightfield, darkfield, differential interference contrast, and fluorescence microscopy capabilities. The higher resolution also allows for imaging an entire threshold study in a single image using its area scan function.

Differential interference microscopy was used to optically determine the height of features of an Olympus LEXT Interference microscope located in the wet chemistry room of the Lurie Nanofabrication Laboratory. While the instrument is limited optically to the diffraction

limit of visible light, it has 20 nm height resolution. It is ideal for structures over 100 nm tall that are too rough to take high quality AFM images.

A4.2 Atomic Force Microscopy

Atomic force microscopy is a scanning probe technique that is used to determine the height of various nanostructures. It was performed on the various stages of HSFL evolution and was also used to measure crater depths during ablation experiments. Images were taken on a Bruker ICON AFM at the Electron Microscopy and Microanalysis lab located in the North Campus Research Facility.

Measurements were taken using standard tapping mode because the manual control allowed for real time adjustments of the imaging conditions. Noise can be reduced during each trace by reducing the set point amplitude. This causes the tip to push harder against the sample. The set point can be reduced until the tip begins picking up debris from the surface. Debris on the tip is signified by the laser moving off the center of the photodiode during a scan.

The other most common issue with imaging are tip artifacts that appear as repeated triangles on the image. This occurs because the feature being imaged is smaller than the tip, which causes the tip to image itself. These artifacts are particularly common when imaging Si. The solution to this problem is to switch out to a newer tip that has not become blunt from previous use.

A4.3 Scanning Electron Microscopy

Scanning electron microscopy (SEM) images were taken on a Hitachi S3200-N SEM located in the Lurie Nanofabrication Laboratory clean room. The microscope provides the high SEM resolution, ~10 nm spatially during regular operating conditions, due to its field emission gun electron source. For the highest resolution images, the user should correct not only correct astigmatism, but also follow the beam alignment, aperture alignment, and stigmator lens alignment with the module located directly in the SEM software. Energy dispersive x-ray spectroscopy can also be taken but the results should be interpreted with the understanding that the excitation volume extends well beyond the sample surface.

A4.4 Transmission Electron Mircoscopy

Transmission electron microscopy (TEM) samples were made using focussed ion beam lift-out in an FEI NOVA FIB located in the Electron Analysis and Microscopy Laboratory. 50 nm of Au were first sputtered to protect the surface during lift-out. This was done as a precautionary measure to show that the Pt deposition was not eroding the surface. Additionally, 2 μm of Pt were deposited as additional protection from ion beam milling using the electron beam. While each new material will require a different recipe, the appropriate beam currents for GaAs are provided here. A nice visualization of the lift-out procedure can be found from a microscope manufacturer [Youtube, 2011]. For GaAs, the Pt strip should only be 2 microns tall or it may fracture during sample plucking. The initial trenches should be dug at 1 nA while welding and fine cutting should be performed at 0.10 nA. Polishing should be performed at 50 pA.

Conventional TEM was performed on a JEOL 3011 and scanning TEM (STEM) was performed on an aberration corrected JEOL 2100. Samples are typically aligned to the [110] zone axis for high resolution imaging because it is the cleavage plane for zinc-blende semiconductors. The conventional TEM can be used to take selected area diffraction patterns, bright field, and dark field images. The aberration corrected STEM is more ideal for taking high resolution images because it takes direct images of the atomic positions. The microscope provides both bright field detection and z-contrast from its high angle annular dark field detector. It is also capable of local spectroscopy (energy dispersive x-ray spectroscopy and electron energy loss spectroscopy) and nano-beam diffraction. The advantage of TEM spectroscopy techniques is that the chemical composition of the surface can be separated from that of the bulk. Quantitative spectroscopy was performed by using fixed microscope conditions on calibration samples to determine specific peak to peak ratios.